Photoelectric and magnetic properties of multiferroic domain walls in BiFeO3

Camille Blouzon

Université Pierre et Marie Curie

Ecole doctorale : « Physique en Île-de-France »

Laboratoire de Nano-magnétisme et Oxydes

Photoelectric and magnetic properties of multiferroic domain walls in $BiFeO_3$.

Par Camille BLOUZON

Thèse de doctorat de Physique

Dirigée par Michel VIRET

Présentée et soutenue publiquement le 06 janvier 2016

Devant un jury composé de :

M. Pascal RUELLO, Rapporteur

M. Jens KREISEL, Rapporteur

M. Massimiliano MARANGOLO, Examinateur

M. Nicolas JAOUEN, Examinateur

M^{me} Alexandra MOUGIN, Examinateur

M. Frédéric OTT, Invité

M. Michel VIRET, Directeur de thèse

Acknowledgements

Ces travaux ont été réalisés au Service de Physique de l'Etat Condensé (SPEC) du CEA Saclay, au sein du Laboratoire de Nano-magnétisme et Oxydes (LNO). Je remercie donc tout d'abord François Daviaud, Eric Vincent, Patrice Roche et Claude Fermon pour m'avoir permis d'y réaliser ma thèse.

Ce projet ne serait rien sans les personnes qui en sont à l'origine, Michel Viret, Nicolas Jaouen, Alexandra Mougin et Frédéric Ott que je remercie chaleureusement de m'avoir accompagné durant ces trois années.

Le travail expérimental nécessite des échantillons à étudier, et s'ils sont de grande qualité, leur caractérisation n'en est que plus facile. C'est pourquoi je remercie tout particulièrement Dorothée Colson et Anne Forget de m'avoir permis de travailler sur ces fabuleux cristaux de $BiFeO_3$.

Je tiens à remercier l'ensemble des partenaires de l'ANR MULTIDOLLS, pour les discussions et leur participation à ces travaux. Je n'oublie pas également Brahim Dkhil et Charles Paillard qui ont été de très bon conseil, mais aussi Ludovic Tortech et Jean-Baptiste Moussy pour m'avoir remis sur la voie de la recherche fondamentale.

Un remerciement tout particulier à Jean-Yves Chauleau qui a su me conseiller, m'épauler et finalement a apporté de cette manière une contribution non négligeable à ces résultats. Enfin je remercie Vincent Trauchessec et mon collègue de bureau Pierre-André Guitard pour les bons moments passés durant ces trois années.

Pour finir je tiens à adresser un grand remerciement à l'ensemble de ma famille, belle-famille et amis, pour m'avoir toujours soutenu et accompagné au quotidien durant toutes ces années.

Contents

Introduction

Multiferroics [1] are materials in which several ferroic order parameters coexist and can be coupled in different fashions.

Magnetostriction describes the coupling between deformation (ε) and magnetization (M); electrostriction, the coupling between ε and electric polarization (P); and magnetoelectric effect the coupling between P and M. The mutual control of the order parameters by strain, electric and magnetic field, results in unique hysteretic behaviors.

The need for novel multifunctional materials has led to the renewal of interest in multiferroics [2] as these compounds were first discovered in the 1960's and studied for about a decade. They have a very rich physics and are appealing for applications as they possess simultaneously several order parameters [3]. Competitions between energies associated to order parameters leads to the apparition of regions with a coherent ordering state, called "domains" and the boundaries between adjacent domains, called "domain walls".

In the domains, multiferroicity can provide complex entanglement of the order parameters whereas in the domain walls, resulting from the broken symmetry of the order parameter, they can have rather different properties from those in the domains : e.g. uncompensated magnetic moments [4], a reasonable conductance [5] as well as promising photovoltaic properties [6]. This offers exciting opportunities to control these nanometric objects using number of external fields and allows to establish a new paradigm of ferroic devices where the domain walls, rather than the domains, are the active elements.

Among all multiferroics, $BiFeO_3$ is a material of choice because its two ordering temperatures are well above 300K [7]. It is a ferroelectric antiferromagnet, and magnetoelectric coupling has been demonstrated in bulk [8] and in thin films [9]. Remarkably, $BiFeO_3$ has the largest polarization of all known ferroelectrics ($100\mu C/cm^2$)[10, 11]. A huge research effort is carried out worldwide to understand and exploit the physical properties of this material, which requires to design and tailor $BiFeO_3$ on many scales in order to control the domain structure [12]. In this sense, developing methods and tools to control the domain structure is essential to explore new emergent phenomena

arising at domain walls. These entities are very peculiar and despite the significant effort invested in those study, many aspects remain to be addressed. This is the aim of the present PhD work.

Some of the original properties of $BiFeO_3$ have been investigated including its photoelectric and magnetic properties. A particular attention is given to characterize in a parallel fashion bulk properties and domain walls properties, using original techniques of characterization such as Scanning Photocurrent Microscopy [13], scattering synchrotron facilities or high field pulses.

The first chapter will thus give the basic physics of multiferrocity and $BiFeO_3$.

The photovoltaic effects typically involve two basic processes, including generation of electron-hole pairs as the electrical-charge carriers, and spatial separation of these pairs to form a net electric current. Generation and separation of electrons and holes are usually achieved at a pn junction in a conventional semiconductor solar cell. Ferroelectrics are also natural candidates [14] as they possess the essential necessary ingredients, including the key advantage of an internal built-in electric field [15]. In that case, photovoltaic effects are not constrained to an interfacial region and can produce overbandgap photovoltages [16].

In chapter 2, I will describe ferroelectric photovoltaic mechanisms and review the history and highlight works of this research field. Thereafter, experimental studies will be described where new insights are given on the surprising bulk photovoltaic effect as well as on the role of domain walls in photovoltaic mechanisms.

Spintronic applications hold a large part in $BiFeO_3$ literature [17]. Indeed, using a voltage to write a magnetic memory element and a magnetic field to read it, presents significant advantages over the existing techniques. Applying a voltage for writing allows a much reduced energy consumption as well as higher reliability and size can be scaled down. Reading the memory magnetically has the advantage of being non-destructive, unlike direct ferroelectric reading, which requires switching the polarization. For such memories to actually work, the magnetic state must be electrically switchable and magnetically readable. The first condition is met in $BiFeO_3$, because the easy plane of its antiferromagnetic domains is correlated with the polar direction, and rotating the ferroelectric polarization results in a rotation of the antiferromagnetic sublattice magnetization [8, 9] , i.e., the magnetic state of the sample can be changed by a voltage. On the other hand, the second condition is not directly met, because antiferromagnetic (or, at best, weakly canted antiferromagnetic) domains cannot be easily read.

In chapter 3, two approaches to this problem will be addressed. The first one consists in studying exchange bias, i.e. the magnetic interaction between the spins at the uppermost layer of an antiferromagnet and a thin ferromagnetic layer attached to it. The exchange interaction modifies the magnetic reversal of the ferromagnetic layer, thus translating a voltage-induced change in the underlying antiferromagnetic domains into

a change in the hysteresis of the upper layer. This can then be read by conventional mechanisms. The second aims at probing the theoretically predicted net ferromagnetic moment which can exist in antiferromagnetic domain walls.

These Synchrotron studies have been performed in SOLEIL synchrotron on SEXTANT beamline.

Finally, in chapter 4, an ongoing original study is introduced. The antiferromagnetic structure of domains and domain walls are characterized using high pulsed magnetic fields and atomic magnetic simulations. The preliminary results are very promising as they evidence the magneto-electric coupling and provide clear hints about the contribution of domain walls.

Chapter 1

Multiferroic $BiFeO_3$

Multiferroics are defined as materials that exhibit simultaneously at least two primary ferroic orders : ferromagnetism, ferroelectricity, ferroelasticity or ferrotoroidicity. The benefit of this multifunctionnality comes from the coupling between these orders as shown on figure 1.1. For instance, spontaneous electrical polarization and magnetism often coexist in iron based perovskites. This allows in principle to control the magnetic order of the material with an applied electric field or the electric polarization with an applied magnetic field.

Figure 1.1: Schematic of the three main ferroic orders and the associated coupling. The magnetization M (controlled by a magnetic field H) is linked to the electric polarization P by the magnetoelectric coupling. The deformation ε (controled by the strain σ) is linked to M by the magnetostriction and the electric polarization P (control by the electric field) is linked to ε by the electrostriction or piezzoelectricity. Reproduced from ref [18].

Many magnetic materials and also most of the classical ferroelectrics belong to transition metal perovskite, which makes this class the most promising one for multiferroic materials. In these conventional ferroelectric perovskites, the transition metal atom is usually displaced from the middle of the unit cell through an oxygen. If there is no electron in the d-shell, this displacement is energetically favorable because only the bounding orbital will be occupied. However if there is one d-electron in the d-orbital, this electron will occupy an anti-bounding hybridized state and increase the total energy of the system. As a result, a necessary condition (but not sufficient) for ferroelectricity is that species possess an empty d-shell "$d^0 - ness$" which is not compatible with magnetism originating from partially filled d-shell. This "exclusion" rule [3] allows only a few materials to be simultaneously ferroelectric and ferromagnetic. This rarity can

also be understood using symmetry considerations. To be a ferroelectric/ferromagnetic multiferroic, a material has to show neither spatial reversal symmetry nor time reversal symmetry. Taking into account this symmetry consideration, only 13 groups of Shubnikov out of 122 allow this. Finally, it turns out that (so far) only one material shows a magnetic order and ferroelectricity at room temperature, $BiFeO_3$. This is possible because the ferroelectricity in this material does not only originate from the transition metal but mainly from the bismuth atom.

Based on the microscopic origin of ferroelectricity, multiferroic materials can be classified in two classes [19] :

- Type I multiferroic : ferroelectricity and magnetism appear separately, with different microscopic origins and different order temperatures. The magnetoelectric coupling is usually small.
- Type II multiferroic : ferroelectricity and magnetism appear together, with a common microscopic origin and the same order temperature. In this case, magnetic ordering induces ferroelectricity and the magnetoelectric coupling is strong.

In this chapter, I will come back on the microscopic origin of ferroelectricity and magnetism. I will also describe how these two order parameters can coexist and be used inside materials. Finally I will detail the case of $BiFeO_3$.

1.1 Ferroelectricity

In dielectric materials, the presence of an external electric field induces an internal electric field. Contributions come from free charges, electric dipoles or atomic polarisability which tend to screen the applied electric field. Under certain conditions, electric dipoles of the material can be aligned in the same direction and give rise to a spontaneous polarization. This phenomenon is called ferroelectricity in analogy to ferromagnetism and was discovered by Valasek in 1920 [20]. Ferroelectric materials are characterized by a transition temperature, the Curie temperature T_c between a paraelectric phase and a ferroelectric phase.

1.1.1 The paraelectric phase

In the paraelectric phase, the polarization is proportional to the applied electric field, the response is linear and can be written as :

$$\mathbf{P} = \varepsilon_0 \chi \mathbf{E} \tag{1.1}$$

where ε_0 is the vacuum permittivity, χ the dielectric susceptibility tensor and E the applied electric field.

The total response of a paraelectric material to an applied electric field is given by the electric displacement field D :

$$\mathbf{D} = \varepsilon_0 \mathbf{E} + \varepsilon_0 \chi \mathbf{E} \tag{1.2}$$

where $\varepsilon_0 E$ is the contribution of free charges and $\varepsilon_0 \chi E$ the contribution of bound charges. We introduce the material dielectric constant :

$$\varepsilon_r = 1 + \chi \tag{1.3}$$

which can be seen as the ratio between the response of a material and the vacuum, to an applied electric field :

$$\varepsilon_r = \frac{\varepsilon_0 E + P}{\varepsilon_0 E} \tag{1.4}$$

1.1.2 The ferroelectric phase

In the ferroelectric phase, the center of mass of crystal positive charges is different from that of negative ones. There is a spontaneous electric dipole (or polarization) even for zero applied electric field. This dipole (or polarization) is oriented along a crystallographic direction and can be reversed along an equivalent direction with an applied electric field. Figure 1.2 shows the polarization versus applied electric field curves for an ideal ferroelectric material in the paraelectric phase and, in the ferroelectric phase below the Curie temperature.

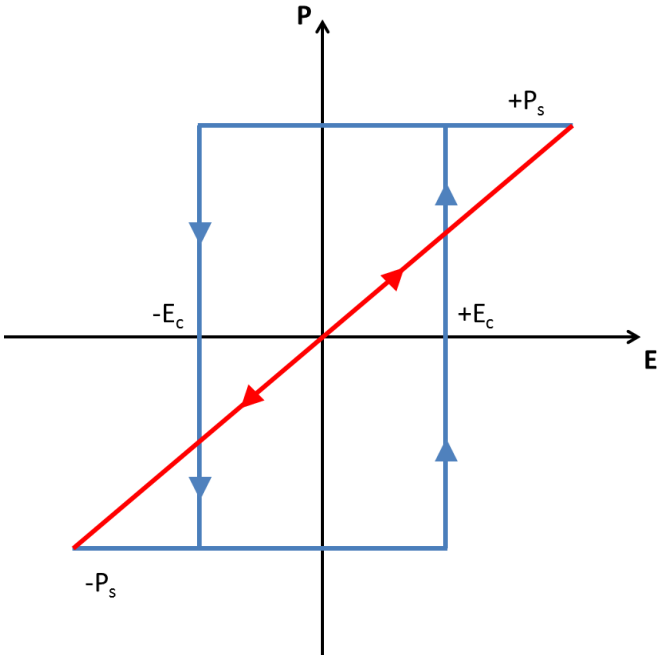

Figure 1.2: In red, schematic of the polarization response versus applied electric field (E) for a ferroelectric material in the paraelectric phase. The slope of the line is the dielectric susceptibility. In blue, schematic of the ideal hysteresis loop of a ferroelectric material below the Curie temperature. The spontaneous electrical polarization can be switched from one saturation state ($+P_s$, $-P_s$) to the other by applying an electric field (E) larger than the coercive field ($+E_c$,$-E_c$) of the material.

The response of the material describes a hysteresis loop between saturation polarizations $\pm P_s$. The orientation of this polarization can be returned by applying an external electric field which is larger than the coercive field E_c. For an ideal ferroelectric, at zero electric field, polarization can be P_s or $-P_s$, depending on the poling history. In the ideal case, the remnant polarization P_r is equal to the saturation polarization.

We can classify ferroelectric materials in two classes which depend on the nature of their phase transition :

- The phase transition is called displacive when electric dipoles are not present in the paraelectric phase. They appear in the ferroelectric phase due to the displacement of the ion in the unit cell which is contracted by the decrease of temperature. This is a first order phase transition with a discontinuous variation of the polarization at the transition temperature.
- The phase transition is called order-disorder when electric dipoles are already present in the paraelectric phase. The phase transition results in dipoles ordering

and leads to the apparition of a spontaneous electrical polarization. This is a second order phase transition with the polarization tending continuously towards zero at the Curie temperature.

Microscopic origin of ferroelectricity is linked to phase transition and thus can be described with thermodynamics and the Landau theory [21].

In the Landau assumption, free energy is an analytical function of the order parameter which comes from the symmetry of the high temperature phase. Therefore the free energy of the system can be described as a power expansion of the order parameter P close to T_c. For a non polarized crystal, the symmetry imposes $F(P) = F(-P)$. Therefore, the free energy does not contain odd terms and can be written as :

$$F = \alpha_0 + \frac{\alpha_2}{2}P^2 + \frac{\alpha_4}{4}P^4 + \frac{\alpha_6}{6}P^6 + \ldots - EP \tag{1.5}$$

where $\alpha_i$are temperature dependent coefficients, E the applied electric field along the polarization P.

At thermal equilibrium, the configuration of the system is given by :

$$\frac{\partial F}{\partial P} = 0 = -E + \alpha_2 P + \alpha_4 P^3 + \alpha_6 P^5 + \ldots \tag{1.6}$$

To obtain a ferroelectric state, we need that α_2 vanishes for a temperature T_0. Thus it can be expressed as : $\alpha_2 = \gamma(T - T_0)$ where γ is a positive constant and T_0 is equal or inferior to T_c. A negative value of α_2 means that the non-polarized lattice is unstable and the next term has to be considered :

If α_4 is positive, α_6 can be neglected and the transition is second order. The shape of the free energy at zero field with respect to the temperature is shown on figure 1.3. Above T_c, F has only one minimum. Below T_c F shows two minima for P_s and $-P_s$. The material is therefore ferroelectric with a spontaneous electrical polarization P_s .

If α_4 is negative, α_6 cannot be neglected anymore and must be positive to counterbalance the continuous decrease of the free energy. The transition is first order. At T_c, the free energy shows simultaneously several minimums for $P = 0$ and $P = \pm P_s$ as shown on figure 1.4. Thus $T_0 < T_c$.

Below the Curie temperature T_c, the electric displacement can be written :

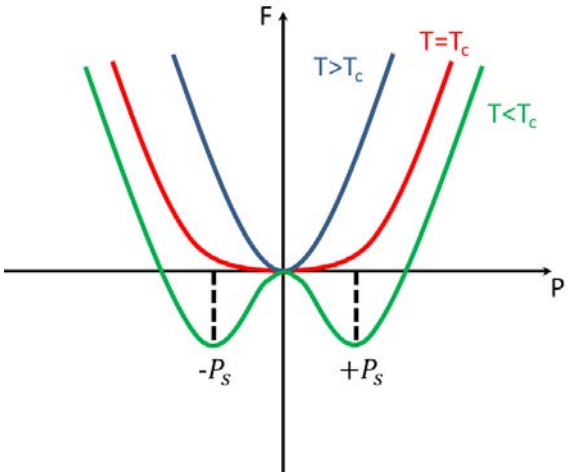

Figure 1.3: Schematic of the evolution of the free energy versus polarization for temperatures around a second order phase transition.

$$\mathbf{D} = \varepsilon_0 \varepsilon_r \mathbf{E} + \mathbf{P_s} \tag{1.7}$$

If P_s is much larger than E, $\varepsilon_0 \varepsilon_r E$ is negligible. Therefore, the Gauss law for an infinite sample with P_s normal to the sample surface gives :

$$P_s \approx \frac{Q}{S} \tag{1.8}$$

The unit commonly used for polarization is $\mu C/cm^2$ and spontaneous polarization is usually in the $\mu C/cm^2$ range for perovskite based ferroelectrics.

1.1.3 Depolarizing field

Usually the polarization inside a sample is uniform with respect to its geometry. Only the applied electric field E_0 and the depolarizing field E_d contribute to the macroscopic electric field E :

$$\mathbf{E} = \mathbf{E_0} + \mathbf{E_d} \tag{1.9}$$

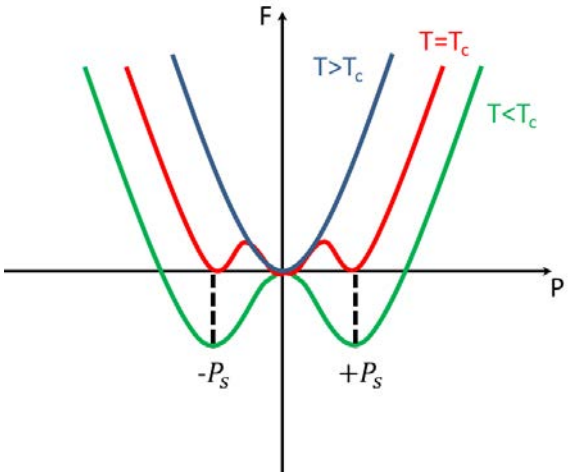

Figure 1.4: Schematic of the evolution of the free energy versus polarization for temperatures around a first order phase transition.

For an ellipsoid shape sample a uniform polarization produces a uniform depolarizing field opposite to the spontaneous polarization as shown on figure 1.5.

If P_x, P_y, P_z are polarization components with respect to the ellipsoid axis, then the depolarizing field components can be written :

$$E_{d,x} = -\frac{N_x P_x}{\varepsilon_0} \tag{1.10}$$

$$E_{d,y} = -\frac{N_y P_y}{\varepsilon_0} \tag{1.11}$$

$$E_{d,z} = -\frac{N_z P_z}{\varepsilon_0} \tag{1.12}$$

where N_x,N_y,N_z are the depolarizing factors which depend on the ratio between the ellipsoid axes.

By taking N_x,N_y,N_z as eigenvalues of a tensor, we can generalize the previous case :

$$\mathbf{E_d} = -\tilde{N}\frac{\mathbf{P_s}}{\varepsilon_0} \tag{1.13}$$

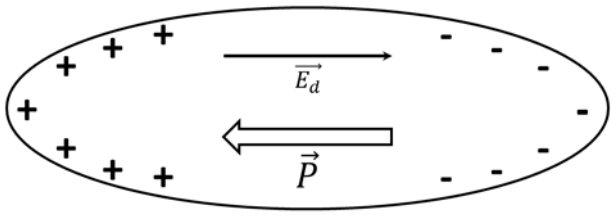

Figure 1.5: Ellipsoid shape sample with a uniform polarization. The polarization surface charges are indicated and induced a depolarizing field $\overrightarrow{E_1}$ which is opposite to $\overrightarrow{P}$.

where $\tilde{N}$ is a tensor of depolarizing factors.

The depolarizing field is only related to the shape of the sample.

In the infinite thin layer case, a polarization arising in the out-of-plane direction will induce a surface charge density :

$$\sigma_{pol} = \mathbf{P} \cdot \hat{n} \tag{1.14}$$

where $\hat{n}$ is the unit vector perpendicular to the surface.

These charges generate a depolarizing field which acts against the ferroelectric polarization :

$$\mathbf{E_d} = -\frac{\mathbf{P}}{\varepsilon_r \varepsilon_0} \tag{1.15}$$

where $\varepsilon = \varepsilon_r \varepsilon_0$ is the dielectric constant of the material. A simple numerical application gives a depolarizing electric field of 3 GV/m for $BiFeO_3$ which is much larger than the electrical breakdown of the material. The screening of the polarization charges then appears as a fundamental parameter of ferroelectric systems and moreover the boundary conditions will be a key to understand the ferroelectric behavior.

1.1.4 Screening

A standard device configuration with electrodes on top of ferroelectric surfaces can provide an efficient screening of the polarization charges. The free charges of the metal electrodes are accumulated at the metal/ferroelectric interface and screen the polarization charges. For an ideal contact, all the polarization charges are screened by the

metal free charges. In realistic system, the quality of the interface is not perfect and a few Angstroms of roughness can lead to an imperfect screening of the polarization [22]. The potential at the interface directly depends of the imperfect contact width λ_{eff} :

$$\triangle V = \lambda_{eff} \frac{P_s}{\varepsilon_0} \tag{1.16}$$

As a result, a small depolarizing field remains, as illustrated on figure 1.6, which modifies the electronic properties of the interface. The depolarizing field is thus given by :

$$\mathbf{E_d} = -2\lambda_{eff} \frac{\mathbf{P_s}}{d\varepsilon_0} \tag{1.17}$$

where d is the sample thickness. Therefore, one can change the interface properties by reversing the polarization below the electrodes.

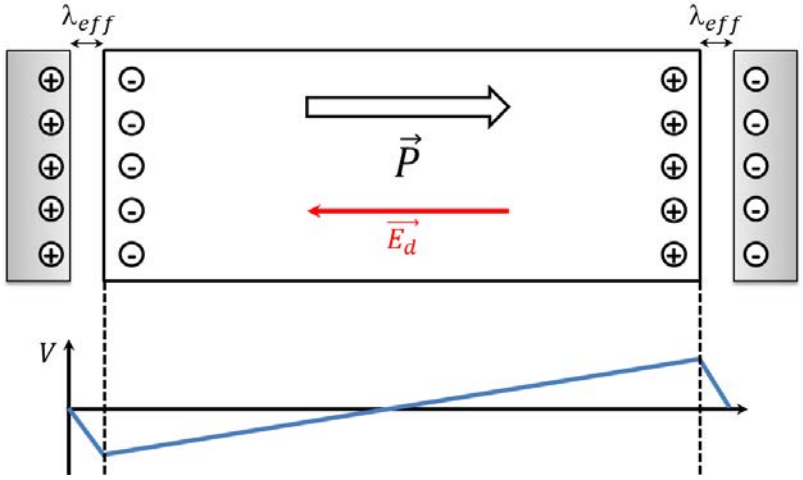

Figure 1.6: Schematic of a metal/ferroelectric/metal structure in capacitor configuration. The imperfect screening of the polarization charges leads to a depolarizing field $\mathbf{E_d}$ which in turn influence the electric fields at the interface.

There are several other screening processes, illustrated on figure 1.7, which contribute to decrease the depolarizing field even when there are no electrodes on top of the ferroelectric surfaces :

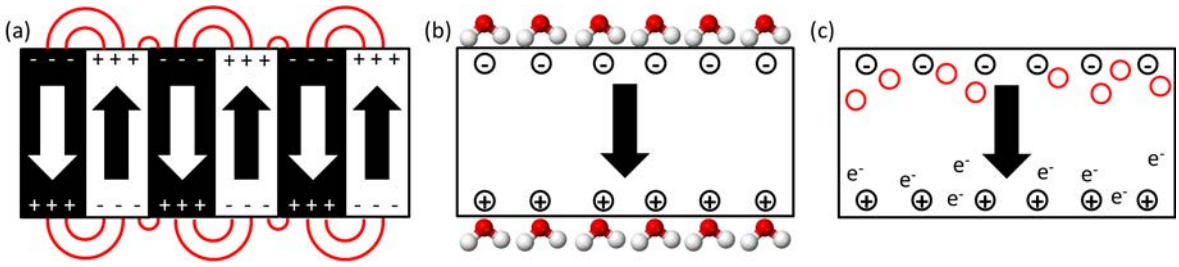

Figure 1.7: Schematics of screening processes in ferroelectric materials : (a) Each domain stray field induce by polarization surface charges decrease the depolarizing field of each neighboring domain. (b) Adsorbat of polar molecules (water) on the surface screens the polarization surface charges. (c) Free charges as electrons or oxygen vacancies (red circle) can migrate in the material to screen the polarization surface charges.

- In a ferroelectric material one can generally find different domains. Inside each domain, the spontaneous polarization has a unique direction which changes between different domains. On the figure, the polarization is opposite in each domain and the depolarizing field is zero because each domain screens the adjacent one. This is why, naturally, ferroelectric materials show a domain pattern when they are elaborated without specific precaution.
- Free charges inside the ferroelectric material can also be a screening source. As ferroelectrics are usually good insulators, the free charges come from defects. In oxide ferroelectrics oxygen or cation vacancies are the main defects and provide a efficient screening of the polarization.
- Adsorbates on the sample surface (like water, organic compounds...) provide dipoles to screen the depolarizing field.

1.2 Magnetism

The filling of the atomic orbitals with electrons is given by Hund's rules, and results from the competition between the Pauli exclusion principle and the Coulomb repulsion. As the Pauli exclusion prevents two spins to occupy the same quantum state simultaneously, two parallel spins have to reside in different orbitals whereas two anti-parallel spins can reside in the same orbital. Therefore two parallel spins save some Coulomb energy compared to two anti-parallel spins. A mechanism able to induce magnetic moments on atoms with partially filled external orbitals. The exchange interaction between magnetic species in a solid leads to a magnetic order which depends of the system symmetry :

- For positive exchange interaction, magnetic ordering leads to a net magnetic moment at zero field, one talks about ferromagnetism.
- For negative exchange interaction, magnetic ordering leads to a zero net magnetic moment, one then talks about antiferromagnetism.

These energy terms are in competition with thermal agitation and above a Curie temperature (T_C) for ferromagnetism and Néel temperature (T_N) for antiferromagnetism, the magnetic order disappears in a paramagnetic phase.

1.2.1 Paramagnetism

The magnetization M, which is defined as the magnetic moment per unit volume, is proportional to the applied magnetic field :

$$\mathbf{M} = \chi \mathbf{H} \tag{1.18}$$

Where χ is the magnetic susceptibility tensor and H is the applied magnetic field.

Materials that show negative magnetic susceptibilities, $\chi < 0$, are called diamagnetic whereas materials with positive magnetic susceptibilities, $\chi > 0$, are called paramagnetic.

The magnetic susceptibility can also be described by the Curie law :

$$\chi = \frac{C}{T} \tag{1.19}$$

where C is the Curie constant.

Both the applied magnetic field H and the depolarizing field H_d contribute to the macroscopic magnetic field H:

$$\mathbf{H} = \mathbf{H_0} + \mathbf{H_d} \tag{1.20}$$

$$\mathbf{H_d} = -\tilde{N}\mathbf{M} \tag{1.21}$$

Where $\tilde{N}$ is the depolarizing tensor which only depends on the material's shape.

The response of a paramagnetic material to an allied magnetic field is given by :

$$\mathbf{B} = \mu_0(\mathbf{H} + \mathbf{M}) \tag{1.22}$$

Where $\mu_0$is the vacuum permeability and B the magnetic induction.

We introduce the material's permeability constant μ to define the reaction of a material to an applied magnetic field. The relation between the induction B to the excitation H is expressed as follows :

$$\mathbf{B} = \mu_0(1 + \chi)\mathbf{H} \tag{1.23}$$

$$\mu_r = 1 + \chi \text{ and } \mu = \mu_0\mu_r$$

Thus :

$$\mathbf{B} = \mu\mathbf{H} \tag{1.24}$$

The larger the permeability of the material, the bigger its ability to concentrate the magnetic flux.

1.2.2 Exchange interaction and anisotropy

Below the ordering temperature, the exchange interaction leads to a parallel arrangement of the direction of the spins. This interaction can be described by the Heisenberg Hamiltonian :

$$H = -2J_{ij}\mathbf{S_i} \cdot \mathbf{S_j} \tag{1.25}$$

Where $J_{ij}$is the exchange integral between spin S_i and spin S_j.

If $J > 0$ then the interaction is ferromagnetic otherwise if $J < 0$ the interaction is antiferromagnetic.

The macroscopic magnetization will tend to be oriented in an "easy" axis direction which is determined by the symmetry of the crystal through the magnetocrystalline energy.

In fact, the crystal field resulting from the material's symmetry tends to modify the shape and the orientation of the charge distribution (orbital). As a result, the spin-orbit coupling leads to favorable directions of the spins. The result is a preferential orientation of the macroscopic magnetization in some crystallographic directions of the crystal.

1.2.3 Ferromagnetism

For a ferromagnetic material, the exchange integral is positive ($J > 0$). Then spins are parallel and oriented in the same direction as shown on figure 1.8. This induces a spontaneous microscopic magnetization.

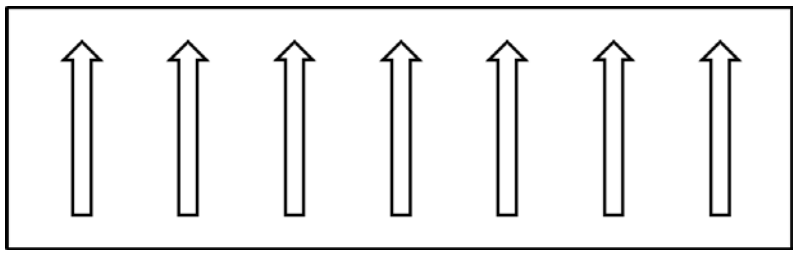

Figure 1.8: Schematic of parallel alignment of the spins in a ferromagnetic material which induce a spontaneous microscopic magnetization.

The exchange interaction is a short-range force. Then after a certain number of aligned spins, the minimization of the magnetostatic energy tends to favor spins aligned in the opposite direction. At the macroscopic scale, the magnetostatic energy imposes different orientations of the magnetization in what are called magnetic domains. Two adjacent domains are separated by a domain wall where the magnetization smoothly rotates between the two orientations of the magnetization. Magnetic and ferroelectric domain walls will be introduced later in this manuscript.

This domain structure is the steady state of a virgin magnetic sample, which induce a zero net magnetic moment. Applying a magnetic field leads to the displacement of the domain wall and the saturation of the sample with a magnetization parallel to

the applied magnetic field. Often this also leads to a spontaneous magnetization at zero field. The representation of the magnetization versus applied magnetic field is an hysteresis loop.

1.2.4 Ferrimagnetism

In many ferromagnetic crystals, the magnitude of the spontaneous magnetization at 0 K is not consistent with a ferromagnetic ordering of the total magnetic moments of the constituting ions. We call ferrimagnets compounds which have two antiferromagnetically coupled magnetic sublattices with different saturation magnetizations as shown on figure 1.9. This results in a net magnetic moment.

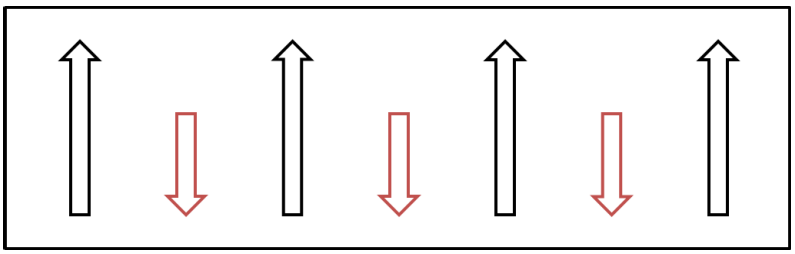

Figure 1.9: Schematic of anti-parallel alignment of two magnetic sublattices in a ferrimagnetic material. Each lattice has a different magnetic moment and this arrangement leads to a spontaneous magnetization.

For instance, ferrites, which have a spinel structure, have one lattice of Fe^{3+}antiferromagnetically coupled with a lattice of Fe^{2+}. The resulting magnetic moment is therefore non zero. In this case, the three exchange integrals J_{AA}, $J_{BB}$and J_{AB} are all negatives but J_{AB} is larger and induces a predominant antiferromagnetic coupling between the lattice A and the lattice B with a ferromagnetic coupling inside each lattice A and B. This simple example is not representative of the complexity of ferrimagnetic materials where usually ionic species A and B are from different nature.

1.2.5 Antiferromagnetism

In an antiferromagnetic material, the exchange integral is negative ($J < 0$) and results in an antiparallel coupling between two ferromagnetic sublatices as shown on figure 1.10. For an homogeneous sample, there is no net magnetization.

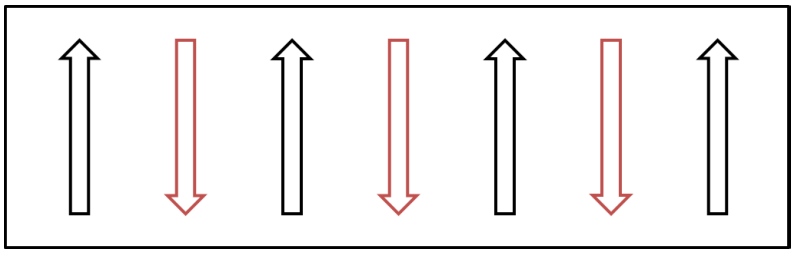

Figure 1.10: Schematic of anti-parallel alignment of two magnetic sublattices in an antiferromagnetic material which results in a zero net macroscopic magnetization.

For perovskite structures, depending on the system symmetry, different organizations of the sublattices are possible. This results into three structure classes which are described on figure 1.11.

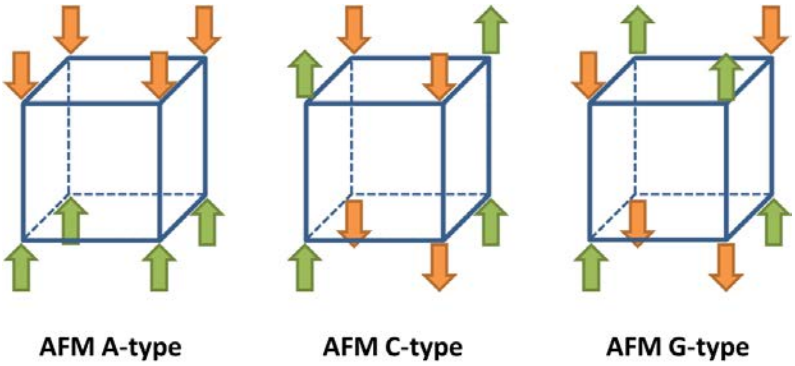

Figure 1.11: Antiferromagnetic structures in perovskites.

The superexchange mechanism is the main exchange interaction in magnetic insulators. The coupling takes place between two magnetic cations through a non-magnetic anion resulting from the overlap of the localized orbitals of the magnetic element with those of intermediate ligands. As shown on figure 1.12, 3d wave functions hybridize with p wave functions of the ligand resulting in a delocalization of the 3d electrons by hopping between the two metallic sites through the ligand. The antiparallel spin configuration between the two metal ions increases the probability of hopping since two spin up or spin down electrons cannot occupy the same state by the Pauli exclusion principle.

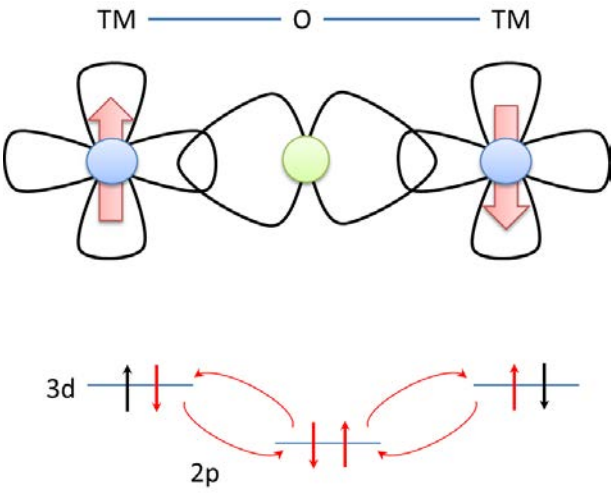

Figure 1.12: Schematic of the superexchange mechanism. 3d wave functions hybridize with p wave functions of the ligand resulting in a delocalization of the 3d electrons by hopping between the two metallic sites through the ligand. The antiparallel spin configuration between the two metal ions increases the probability of hopping.

The superexchange interaction is predicted by empirical Goodenough-Kanamori-Anderson rules and can describe the exchange behavior in most of the cases. According to these rules, a 180^{o} superexchange (the magnetic ion-ligand-magnetic ion angle is 180^{o}) of two magnetic ions with partially filled d shells is antiferromagnetic, whereas a 90^{o} superexchange interaction is ferromagnetic.

Often, the antiferromagnetic ordering is not perfect and shows a canting of neighboring spins. To understand this, one needs to consider an additional anti-symmetric exchange coupling between electron spins on neighboring metal ion sites : The Dzyaloshinskii-Moriya (DM) interaction [23, 24]. This interaction favors a canting of antiparallel spins, leading to a small net magnetization of the originally antiferromagnetic crystal, called weak ferromagnetism. This interaction gives a contribution to the total energy of the form :

$$H_{DM} = \mathbf{D_{ij}} \cdot (\mathbf{S_i} \times \mathbf{S_j}) \tag{1.26}$$

This energetic contribution forces the net ferromagnetic moment originates from the spin canting to be perpendicular to the coupling vector D. This coupling vector is due to spin-orbit coupling and can only be non-zero in a low-symmetry environment, in which the ligand ion is displaced from its ideal crystallographic position as shown on figure 1.13. D vanishes for local inversion center between the spin sites.

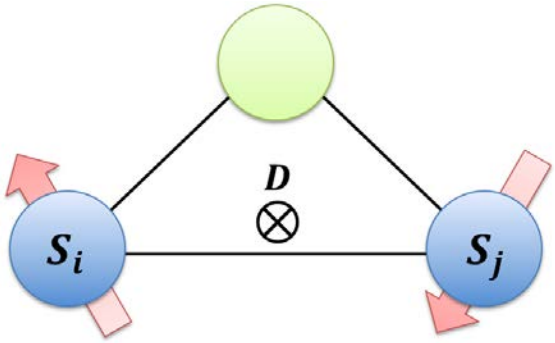

Figure 1.13: Dzyaloshinskii-Moriya (DM) interaction where two spins S_i, S_j interact through a ligand (green circle). The displacement of the ligand decreases the symmetry and promotes the canting of the spins through the spin-orbit coupling. D is the coupling vector which is correlated to the exchange interaction.

A rearrangement of the magnetic structure can result in the apparition of a magnetic spiral when the consecutive canting angles have to be of similar sign. As shown on figure 1.14, two types of spirals can be observed :

- Cycloidal, which gives a zero net magnetization
- Spiral which gives a small net magnetization.

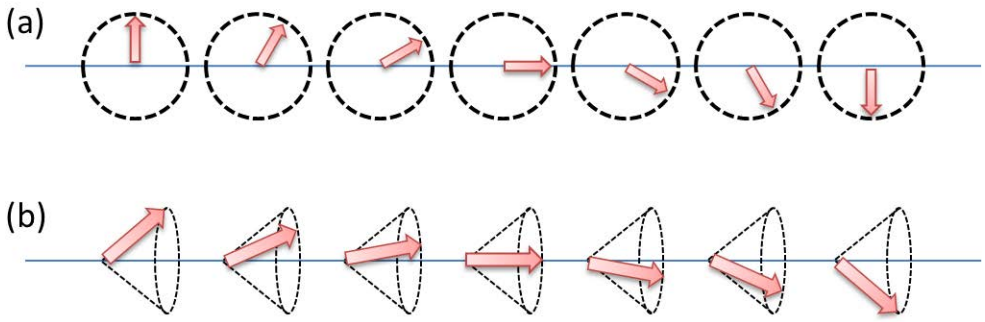

Figure 1.14: Magnetic structures : a. Cycloidal arrangement of the spins which gives a zero net magnetization. b. Spiral arrangement of the spins which gives a small net magnetization.

The response of an antiferromagnetic system to an applied magnetic field depends on its magnetic structure and will be detailed in chapter 5.

1.3 Magnetoelectrics

Magnetism and ferroelectricity have been considered exclusive because of the apparent "exclusion" of their microscopic origin as mentioned above. They are also distinguished in many respects. From a symmetry point of view, ferroelectricity is related to inversion symmetry whereas magnetism is related to time reversal symmetry. Ferroelectricity can be approached with a classical model of point charges, while magnetism is essentially a quantum mechanical phenomenon. However, Maxwell's equations unify the electric (E) and the magnetic fields (B) into the electromagnetic field. This suggests that the electric and magnetic properties should be seen in a unified way.

The magnetoelectric effect is the phenomenon of inducing magnetic (electric) polarization by applying an external electric (magnetic) field.

Since 1894, and the prediction of P. Curie [25] about the magnetoelectric effect, measurements usually show weak coupling. The reason is that electrons contributing to the electric polarization and magnetization are different. On the other hand, strong magnetoelectric coupling can be seen when the effect originates from the same species.Therefore we can separate magnetoelectric materials in two different classes which depend on the microscopic origin of the coupling :

Direct coupling : Magnetic species are involved in the ferroelectric ordering. An applied electric field acts on magnetic ion positions which change the crystal field and tunes the overlapping wave functions. This magnetism-induced ferroelectric material is called improper ferroelectric. The two orders have the same ordering temperature and induce a strong magnetoelectric coupling. Direct coupling is responsible for multiferroicity of type I.

Indirect coupling : The electric and magnetic orders result from different species with two coupling sublattices. The displacement of one species by an applied field induces an elastic rearrangement of the other species in the unit cell. This new configuration gives rise to new magnetic and electric configurations. This usually concerns proper ferroelectrics and induces a low magnetoelectric coupling. Indirect coupling is responsible for multiferroicity of type II. An other form of indirect coupling consists in using one ferromagnetic material and one ferroelectric material to create a composite heterostructure. Despite their interest, the origin of this coupling is too far from that of single phase magnetoelectrics and thus they will not be described in this manuscript.

The magnetoelectric effect can be described with the Landau theory by writing the free energy of the system in term of an applied magnetic field and an applied electric field. From this, we derive the polarization and the magnetization as follows :

$$\mathbf{P_i} = \Sigma\alpha_{ij}\mathbf{H_j} + \Sigma\beta_{ijk}\mathbf{H_j}\mathbf{H_k} + \dots \tag{1.27}$$

$$\mathbf{M_i} = \Sigma\alpha_{ij}\mathbf{E_j} + \Sigma\beta_{ijk}\mathbf{E_j}\mathbf{E_k} + \dots \tag{1.28}$$

where $\alpha_{ij}$is the 1st order susceptibility tensor and β_{ijk} is the 2nd order susceptibility tensor.

A direct magnetoelectric coupling involves the linear coefficient α_{ij} which is bounded by the relation :

$$\alpha_{ij}{}^{\mathbf{2}} \leq \varepsilon_{ii}\mu_{jj} \tag{1.29}$$

According to this equation, a ferromagnetic (which has a high permeability) and a ferroelectric (which has a high permittivity) material will have a strong magnetoelectric coupling. Nevertheless, a lot of magnetoelectric materials have a low permettivity or/and permeability which result in a negligible linear magnetoelectric coupling. Consequently it is suitable for these materials to consider the quadratic coefficient β_{ijk} which will dominate the magnetoelectric coupling.

The indirect magnetoelectric coupling is specific in each multiferroic material and the case of $BiFeO_3$ will be described at the end of this chapter. As $BiFeO_3$ also shows direct magnetoelectric coupling, where the magnetic ordering leads to a net electrical polarization, I will thus now detailed how a spin ordering can lead to ferroelectricity.

Direct coupling : spin origin

Various types of spin order [26] can potentially break the inversion symmetry and produce a spontaneous electrical polarization. There are three major mechanisms for ferroelectricity of spin origin : exchange-striction, spin current and spin dependent p-d hybridization which are depicted on figure 1.15.

Figure 1.15: Three major mechanisms of ferroelectricity of spin origin: (a)–(c) exchange-striction mechanism arising from the symmetric spin exchange interaction; (d)–(f) spin-current model arising from the antisymmetric spin exchange interaction or inverse DM model; and (g)–(i) spin dependent p–d hybridization mechanism due to the relativistic spin orbit coupling. Here, M and X indicate magnetic and ligand ions, respectively. S_i and S_j represent the spin orientations at each magnetic site, and e_{ij} and e_{il} are the unit vectors. The unit vector connecting two selected sites (M–M for (d) and M–X for (g), respectively). For each mechanism, the expected direction of magnetically induced electric polarization P is also indicated. Reproduced from ref [26].

Exchange-striction For a one-dimensional system, the Peierls' theorem states that a "*one-dimensional equally spaced chain with one electron per ion is unstable*". The total energy of this system will be lower if there is a distortion of the lattice where every ion moves closer to one neighbor. This is also known as dimerization. Thus the two different dimerized charges become a dipole moment and the periodic array of these dipole moments produces a ferroelectric order. When an antiferromagnetic exchange coupling between two neighboring spins is modulated by this atomic displacement, spin singlet pairs are spontaneously created as mentioned above. This phenomenon is called spin-Peierls instability which forms a periodic array of spin-singlet pairs by alternating the strength of the exchange coupling between up-up (down-down) or up-down (down-up) pairs.

This can be summarized as follows :

$$\mathbf{P_{ij}} \propto \mathbf{\Pi_{ij}}(\mathbf{S_i}.\mathbf{S_j}) \tag{1.30}$$

where the symmetric exchange interaction between the neighboring spins S_i and S_j induces striction along a specific crystallographic direction and result in a spontaneous electrical polarization.

This effect needs a commensurate spin order and a low symmetry. It was observed in material such as perovskite type rare-earth (R) manganites, $RMnO_3$ for $R = Ho, Er, Tm, Yb$ and Lu [27].

Spin current model In the superexchange interaction, the hoping of electrons between the two metallic sites can be seen as generating a spin current, which is non-zero when the spins are canted (for instance due to the DM interaction). In turn, the spin current induces an electric field, i.e an electrical polarization given by the following expression :

$$\mathbf{P_{ij}} \propto \mathbf{e_{ij}} \times (\mathbf{S_i} \times \mathbf{S_j}) \tag{1.31}$$

where e_{ij} is the propagating vector connecting the spins S_i and S_j.

An other point of view suggests that the apparition of a canting between two neighboring spin (in metal-ligand-metal configuration) leads to the displacement of the ligand atom and therefore to an electrical polarization. This arises from the inverse DM effect.

Both theories point to the same equation, and show that non colinear spin structures lead to an electrical polarization perpendicular to the propagation vector.

This effect only needs spin-orbit coupling and can lead to incommensurate structures. It was also observed in perovskite type rare-earth (R) manganites, $RMnO_3$ but for $R = Tb$ and Dy [28].

Spin dependent p-d hybridization The spin dependent p-d hybridization is a single spin site mechanism. The locally polar bond e_{il} connecting the spin site i and the ligand site l can be modulated by the spin-direction dependent hybridization arising from spin orbit coupling. When the sum over the crystal lattice sites is not canceled, a macroscopic electrical polarization can be observed and thus, formulated as follows :

$$\mathbf{P_{il}} \propto (\mathbf{S_i} \cdot \mathbf{e_{il}})^2 \mathbf{e_{il}} \tag{1.32}$$

This effect needs spin-orbit coupling and a specific lattice symmetry. However it can be commensurate or incommensurate. It was observed in frustrated spin systems with triangular lattices as delafossite or CdI_2 structure.

1.4 $BiFeO_3$

$BiFeO_3$ is the most studied type I multiferroic material as it is the only one which shows electric and magnetic ordering at room temperature.

1.4.1 Structural properties

Between 1200K and 1100K, $BiFeO_3$ shows two structural phases, still not well defined due to the proximity of the decomposition temperature. The most recent neutron studies [29, 30] indicate that both the β and γ phases are paraelectric orthorhombic phases with $Pnma$ structure. γ is the high temperature phase ($>$ 1198K) and β, the phase between 1198K and 1100K.

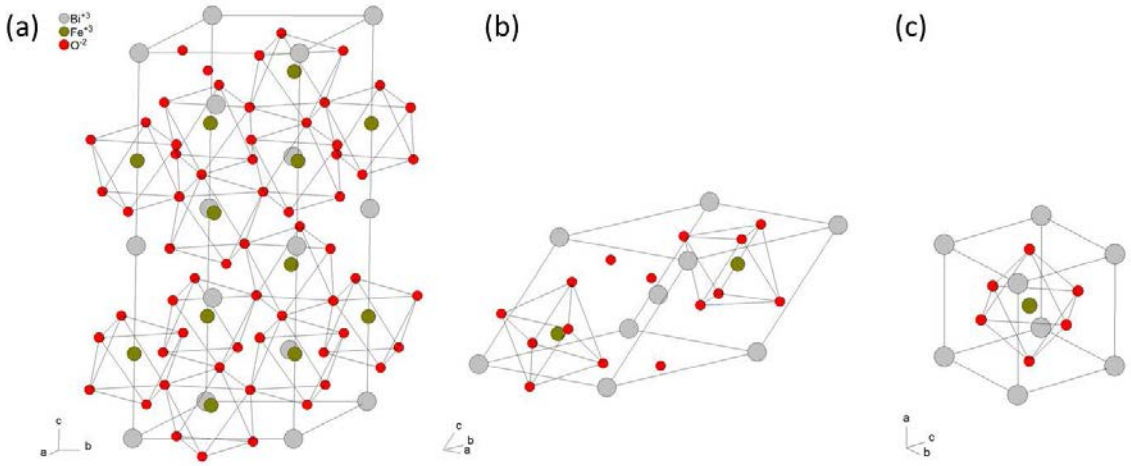

Figure 1.16: (a) Hexagonal, (b) rhombohedral and (c) pseudocubic cells of $BiFeO_3$ in the ferroelectric phase.

Below 1100K, $BiFeO_3$ shows a rombohedral α phase, which belongs to the $R3c$ space group [31]. The perovskite-type unit cell is stretched along the diagonal of the cube which leads to a lattice parameter $a_{rh} = 3.965$Å and a rombohedral angle $\alpha_{rh} = 89.4$Å at room temperature (figure 1.16b). Equivalently, the unit cell can also be described in an hexagonal structure with lattice parameters, $a_{hex} = 5.58$Å and $c_{hex} = 13.90$Å (figure 1.16a). The rombohedral cell is so close to the ideal perovskite unit cell that it can be considered as a pseudocubic (pc) unit cell (figure 1.16c).

In addition, the slight rombohedral deformation leads to large oxygen octahedra tilts ($\omega \approx 11°$) around the trigonal axis. In the crystal structure, two following oxygen octahedra rotate in opposite directions leading one to consider two pseudocubic cells which are connected by their vertices to fully describe the unit cell.

The $BiFeO_3$ crystal structure at room temperature breaks both inversion and time symmetry allowing the coexistence of electric and magnetic orders.

1.4.2 Ferroelectric properties

In $BiFeO_3$, the spontaneous electrical polarization mostly originates from Bi^{3+} ions containing lone pairs of $4s$ electrons which do not participate in the chemical bond. This lone pair is highly polarisable and is displaced along the $[111]_{pc}$ direction [32]. This induces a deformation of the perovskite unit cell where bismuth ions are displaced by 54pm and in turn leads to a 13pm displacement of the iron ion Fe^{3+}. The displacement of the positive ions results in the oxygen octahedra buckle as mentioned above. This

distortion of the unit cell breaks inversion symmetry, the centers of mass of positive and negative charges are not superimposed anymore and thus a spontaneous electrical polarization appears in the $[111]_{pc}$ direction. As a result, the $\{111\}$ axes are the "anisotropy" of the polarization and leads to four possible in-plane variants of the polarization : $[111]$, $[\bar{1}11]$, $[1\bar{1}1]$, $[11\bar{1}]$. For each in-plane variant, the polarization can point upwards or downwards and this finally gives rise to eight equivalent possibilities for the polarization in $BiFeO_3$ as depicted on figure 1.17.

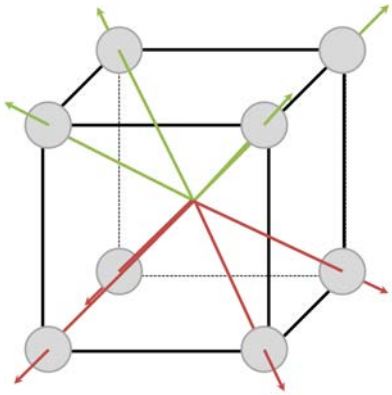

Figure 1.17: Schematic of the eight possible variants of the polarization in $BiFeO_3$.

The insulating behavior of a ferroelectric is an important property in order to measure the ferroelectric polarization. The high quality of $BiFeO_3$ single crystals synthesized by Lebeugle *et al.* in 2007 [10] were determinant to obtain polarization loops at room temperature and measure the largest ferroelectric polarization ever measured with 100 $\mu C/cm^2$.

During a polarization loops, the direction of the polarization switches through a new position depending on the direction of the applied electric field. As the [111] direction is the polarization easy axis, the application of an electric field along a different axis switches the polarization in an equivalent long diagonal which will become the new polarization easy axis. In figure 1.18, an electric field is applied along the [001] direction. The polarization switches along this direction through the closest equivalent direction of the easy axis polarization.

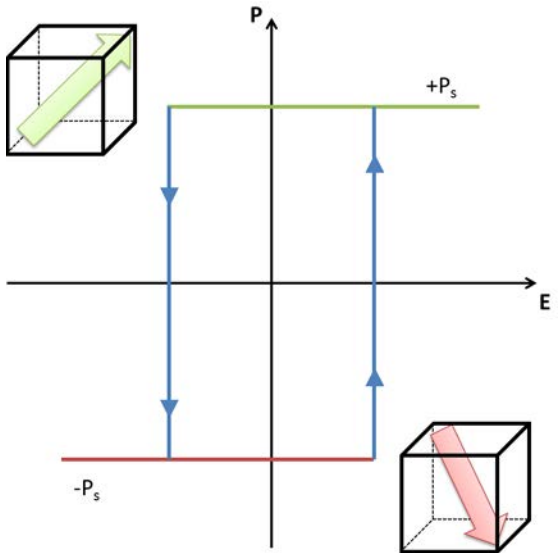

Figure 1.18: Schematic of the hysteretic behavior of a $BiFeO_3$ single crystal under an applied electric field. The ferroelectric polarization switches along {111} equivalent directions during the electric field sweep.

The polarization is generally measured along the direction of the applied electric field. Thus each characteristic value results from the projection of the polarization along the relevant axes.

The switching of the polarization leads to a rearrangement of the unit cell with the interchange of the distortion axis between the old and the new direction of the polarization. This results in an elastic strain in the crystal and the formation of elastic domains which follow the ferroelectric domains. Fatigue measurements on $BiFeO_3$single crystals show that the structure and then the electric properties decrease rapidly with the increasing number of strain loops performed.

1.4.3 Ferroelectric domains

In $BiFeO_3$, the ferroelectric polarization has eight different orientation possibilities. Consequently, two adjacent domains are separated by a domain wall which can be from three different types depending on the angle between polarizations on both sides of the domain wall :

- When only one component of the polar vector is reversed ($[111] \rightarrow [\bar{1}11]$), the polar vectors form an angle of 71° and the domain wall is called a 71° domain wall.

- When two components of the polar vector are reversed ($[111] \rightarrow [\bar{1}\bar{1}1]$), the polar vectors form an angle of 109° and the domain wall is called a 109° domain wall.
- When all components of the polar vector are reversed ($[111] \rightarrow [\bar{1}\bar{1}\bar{1}]$), the polar vectors form an angle of 180° and the domain wall is called a 180° domain wall.

The latter is a purely ferroelectric domain wall, while the former two are also ferroelastic domain walls (since there is a difference in spontaneous strain between the separate domain regions). Consequently, the coupling between ferroelectricity and ferroelasticity in $BiFeO_3$ imposes orientation of domain walls. 71° walls are parallel to {110}planes, 109° to {100}planes and 180° to {111}planes. The different types of domains and domain walls are illustrated on figure 1.19.

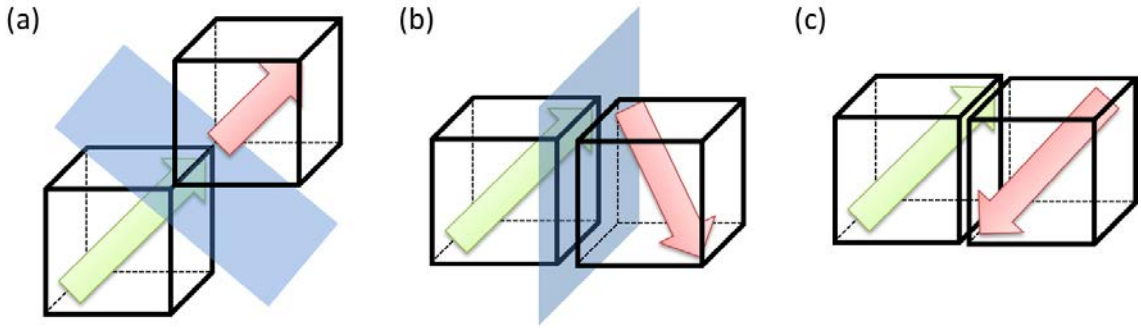

Figure 1.19: Schematic representation of (a) 71°, (b) 109°, (c) 180° domain configurations in $BiFeO_3$. The green and red arrows indicate the direction of the spontaneous polarization, while blue planes represent the most stable domain walls.

Since the work of Landau and Lifshitz in 1935 [33], and later Kittel in 1946 [34], on ferromagnetic materials, we know that domain sizes scale as the square root of the film thickness. This result from a competition between a surface energy coming from the depolarizing field thus directly proportional to domain width (w) and a domain wall energy that is proportional to the density of walls, inversely proportional to w. Both energies can also be related to the film thickness (d) and the minimization of these components leads to the following expression :

$$w = A\sqrt{d} \tag{1.33}$$

where A is a constant.

This scaling has been extended experimentally to ferroelectric [35] and multiferroic [36] materials. However for ultrathin films, the domain pattern does not follow this law

anymore and could be explained by the non-trivial behavior of the polarization close to the surface of ferroelectric (and multiferroic) ultrathin film [37].

1.4.4 Magnetic properties

Below the Néel temperature, T_N =643K, $BiFeO_3$ shows a G-type antiferromagnetic ordering, where each Fe^{3+} is surrounded by six antiparallel spins on the nearest Fe^{3+} neighbors. These spins are not exactly antiparallels because of the DM interaction and thus the local magnetoelectric coupling induces a long range superstructure consisting in an incommensurate cycloidal ordering of the spins [38]. The cycloid has a long period of 64nm and is described by a propagation vector $\mathbf{q}$ along the $[1\bar{1}0]_{pc}$, $[10\bar{1}]_{pc}$, and $[0\bar{1}1]_{pc}$ directions. Antiferromagnetic moments are rotating in the planes defined by the propagation vectors and the polarization $[111]_{pc}$ direction .

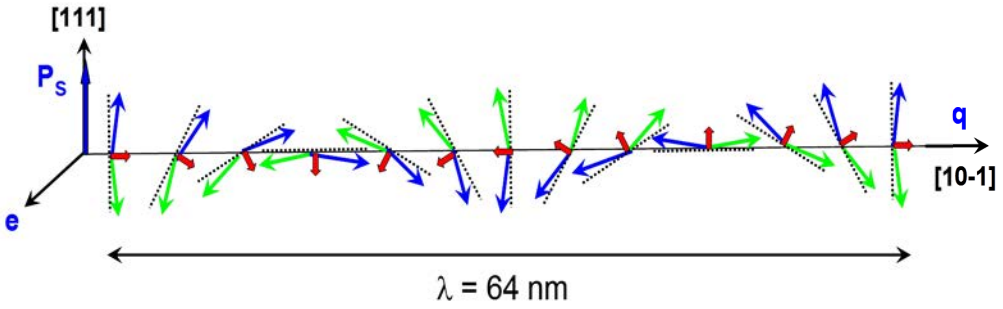

Figure 1.20: Schematic representation of the spin cycloid. The canted antiferromagnetic spins (blue and green arrows) give rise to a net magnetic moment (red arrows) that is spatially averaged out to zero due to the cycloidal rotation. The spins are contained within the plane defined by the polarization vector ($\mathbf{P_s}$) and the cycloidal propagation vector ($\mathbf{q}$). Reproduced from ref [8]

1.4.5 Magnetoelectric coupling

In 1993, Popov *et al* observed, by polarization measurements, the quadratic magnetoelectric coupling linked to the cycloidal ordering. By applying a magnetic field above 20T, the cycloidal order vanished and gave way to a linear magnetoelectric coupling. These measurements revealed that the measured polarization in $BiFeO_3$ has two different contributions of different natures : a first one which comes from the cell distortion and a second one, from the cycloid. However, this will only be understood ten years later [39].

In 2006, Zhao *et al* [9], demonstrated by X-ray photoemission electron microscopy measurements on thin film, the first observation of electrical control of antiferromagnetic domain structure in $BiFeO_3$ at room temperature. These results in agreement with theoretical calculations, show that the switching of the ferroelectric polarization by applying an electric field, leads in turn to the rotation of the antiferromagnetic planes. In fact, the ferroelectric polarization seems to be fixed perpendicular to antiferromagnetic planes and the rotation of the polarization induces a reorientation of the antiferromagnetic order.

Later, in 2008, neutrons measurements on $BiFeO_3$ single crystals have shown that the direction of the ferroelectric polarization is fixed into the propagation's plane of the cycloid [8]. These neutron measurements bring out that an applied electric field can rotate the polarization by 71° but it also rotates the cycloidal plane of 71°. The cycloid and the ferroelectric polarization staying in the same plane as illustrated in figure 1.21.

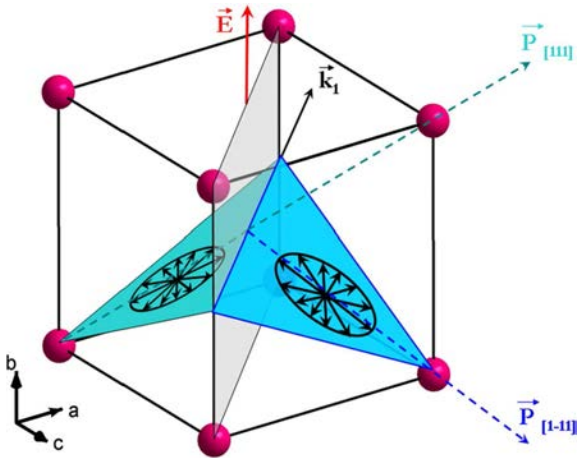

Figure 1.21: Schematics of the planes of spin rotations and cycloids k vector for the two polarization domains separated by a domain wall (in gray).

In $BiFeO_3$, the predicted magnetoelectric effect is an indirect and non-linear quadratic coupling because of the apparent decorrelation between the apparition of the ferroelectricity and the antiferromagnetism. Nevertheless, $BiFeO_3$ is a particular case as this compound possesses both a proper polarization arising from the Bi lone pairs off-centering cations with different charges and a spin cycloid associated to a small 'improper' polarization (see spin current model). Both couple to minimize the total energy, which imposes that the global polarization belongs to the spin rotation plane and is perpendicular to its propagation vector [40].

More details on magnetoelectric coupling in $BiFeO_3$ are given in chapter 4.

1.4.6 Optical properties of $BiFeO_3$

The propagation of light through matter is driven by the polarization of the materials. As the polarization response to the oscillating field of light involves motion of masses, there is a strong correlation between the frequency and the oscillating species. Depending on the frequencies of the incident light, dipoles, electrons, ions will contribute together or independently to the material polarization. The electric displacement field D gives the total response of the dielectric media under an applied electric field :

$$\mathbf{D_i} = \varepsilon_{ij}\varepsilon_0\mathbf{E_j} \tag{1.34}$$

For all rhombohedral media, in the principal axes system, the second rank tensor is only characterized by two elements :

$$\varepsilon_i = \begin{pmatrix} \varepsilon_1 & 0 & 0 \\ 0 & \varepsilon_1 & 0 \\ 0 & 0 & \varepsilon_3 \end{pmatrix} \tag{1.35}$$

They are called uniaxial media and $BiFeO_3$ is one of them. In the pseudocubic reference frame, there are six equivalent$[1\bar{1}0]$ axes normal to the [111] direction that form a plane. Since a second-rank polarizability tensor cannot support a threefold rotational anisotropy, the optical properties are essentially the same for any polarization in this plane. Consequently, $BiFeO_3$ has uniaxial optical anisotropy with the optic axis along the [111] axis. In the optical system of axes, two particular modes of propagation can be described, an ordinary beam polarized in a plane perpendicular to the optic axis and an extraordinary beam polarized in a plane containing the optic axis. The Maxwell equations for harmonic plane waves in media with no free charges and no charge currents, are given by :

$$\Delta \times \mathbf{E} = -j\omega\mu_0\mu\mathbf{H} \tag{1.36}$$

$$\Delta \times \mathbf{H} = j\omega\varepsilon_0\varepsilon\mathbf{E} \tag{1.37}$$

Taking the curl of these equations gives the wave propagation equations :

$$\nabla^2 \mathbf{E} = -\omega^2 \mu_0 \mu \varepsilon_0 \varepsilon \mathbf{E} \tag{1.38}$$

an identical wave equation can be derived for the magnetic field.

Finally, by considering solutions as sinusoidal plane waves, we obtain two different solutions depending on the relative orientation of the incident polarized light with respect to the optic axis.

- For an ordinary beam polarized :

$$k^o = \omega \sqrt{\mu_0 \mu \varepsilon_0 \varepsilon^o} = \omega \frac{n^o}{c} \tag{1.39}$$

- For an extraordinary beam polarized :

$$k^e = \omega \sqrt{\mu_0 \mu \varepsilon_0 \varepsilon^e} = \omega \frac{n^e}{c} \tag{1.40}$$

where n^o, n^e are the ordinary and the extraordinary index, whereas k^o, k^e are the wave vectors associated to the ordinary and the extraordinary waves.

The two states develop a phase difference as they propagate, which changes the total polarization of the wave depending of the thickness crossed. Such media are called birefringent and gives an optical contrast, as shown on figure 1.22, between two different domains which will present two different orientations of the optic axis.

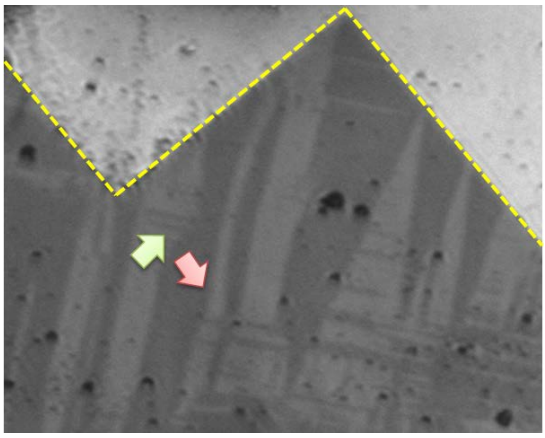

Figure 1.22: Cross polarized optical image of ferroelectric domains in a $BiFeO_3$ crystal. Yellow dash line indicates the edge of a gold electrode. Green and red arrows show the possible in-plane orientation of the polarization in two adjacent domains which leads to an observable optical contrast.

For linearly polarized light in the $(001)_{pc}$ surface plane of $BiFeO_3$ as depicted on figure 1.23c, the incident beam polarization is never completely aligned with the optic axis of the material ([111]). Therefore, there is never a unique extraordinary wave propagating in the material.

Figure 1.23: (a) Real and (b) imaginary parts of the dielectric function ε spectra measured along four different orientations of a single-domain $BiFeO_3$ (001) crystal. (c) Schematic depicting the direction of measurements. Reproduced from ref [41]

In a similar measurement configuration, Choi *et al.* [41] measured by spectroscopic ellipsometry the complex dielectric function along four crystal orientations (figure 1.23a). They finally deduced the extraordinary and the ordinary index as well as the corresponding extinction coefficient (figure 1.23b), giving rise to a detailed description of the optical properties of $BiFeO_3$ versus the energy of the incident light.

1.5 Synthesis of $BiFeO_3$ single crystals

$BiFeO_3$ single crystals are synthesized in the laboratory by Anne Forget and Dorothée Colson [11]. The quality of their work gives us the opportunity to use single crystals with low defect density, high resistivity and in a ferroelectric monodomain configuration.

The alloy $BiFeO_3$has no congruent melting point which means that, at the melting temperature, with the right stoechiometry, the compound will be separated in a liquid phase and a solid phase of $Bi_2Fe_4O_9$. As can be seen on figure 1.24, a solution to crystallize the desired phase, is to introduce a solvent which is called the flux. Usually, the flux is an excess of one species of the alloy, here Bi_2O_3, and it will shift the melting point to a lower temperature where it will lead to the right phase (+ liquid). In the case of $BiFeO_3$, the flux method allows to directly crystallize the α-phase which is already ferroelectric and thus, essential to grow monodomain ferroelectric crystals. The melting point has to be as close as possible to the β-phase border as the proportion of $BiFeO_3$ will be given by the ratio N'P/M'P.

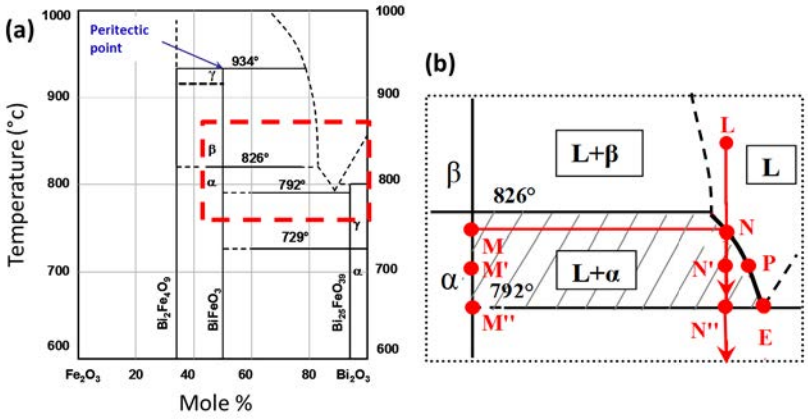

Figure 1.24: (a) Binary phase diagram of Bi_2O_3 and Fe_2O_3. (b) The red dash rectangular region is magnified around the melting point.

With a ratio between 80 : 20 and 90 : 10 in molar percentage of mixing composed by Bi_2O_3: Fe_2O_3, the α-phase of $BiFeO_3$ can be crystallized. The mixing powder is then placed in a crucible made in materials with no interaction with the contents (Pt, Au, Al_2O_3...), and is introduced in a furnace. By following a well defined thermal procedure, the powder is melted at the temperature of 850 °C, and slowly cooled down to 750 °C allowing the single crystal growth. Finally the high proportion of liquid solidifies and stops the crystallization process. The solid mixing in the crucible is composed of $BiFeO_3$ and $Bi_{25}FeO_{39}$.

The crucible is then broken and inside the solidified $Bi_{25}FeO_{39}$ phase, one can find cavities where crystals have grown as shown on images from figure 1.25a,b. The extraction of the crystals from the crucible is done mechanically. Since $BiFeO_3$ is ferroelectric and ferroelastic, this extraction method is not the most efficient one because it can induce strain in the crystals which lead in turn to the formation of multidomains. As

the single domain is very useful to study ferroelectric properties, an observation with a cross polarized microscope needs to be done before further experiments.

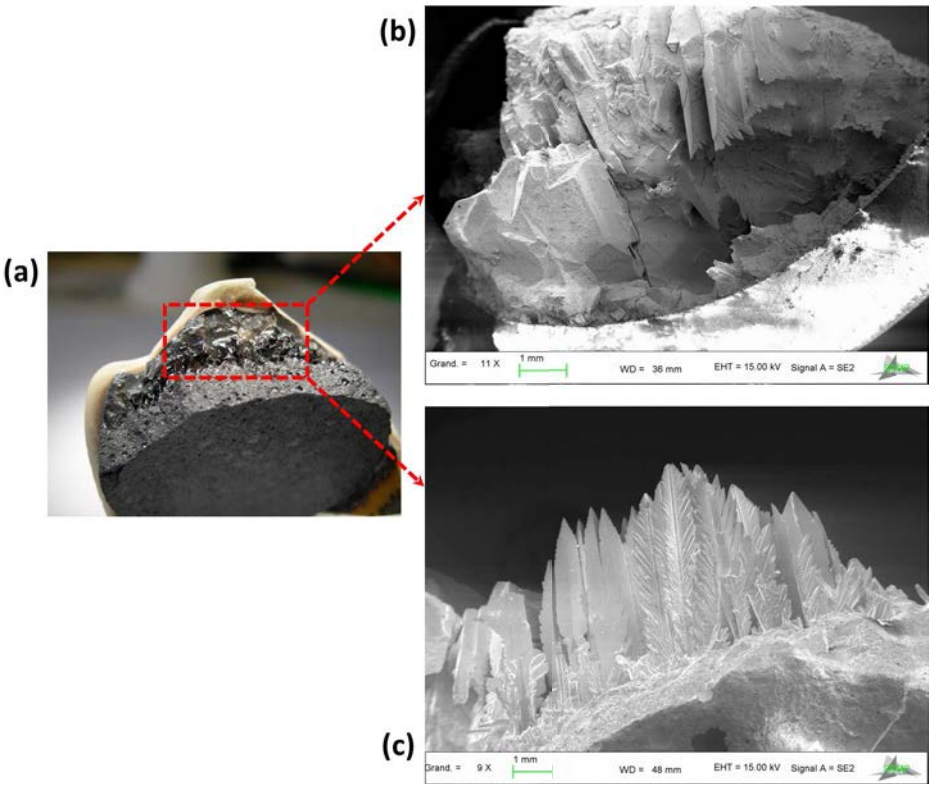

Figure 1.25: (a) Optical image of a broken crucible. Red dash square indicates a cavity where crystals have grown. (b) MEB image of as grown crystals in the cavity. (c) MEB image of dendritic shape crystals. Crystals present an unusable rough face (middle of the image) and a smooth face (left of the image) which can be used for measurements.

The crystals have thin dendritic shapes of hundreds of micrometers, with usually the polarization lying along the long axis of the dendrite which is coherent with the strong anisotropy of $BiFeO_3$ and the minimization of electrostatic energy induced by the depolarizing field. The thickness does not exceed 100 microns. Some crystals can also have a plate shape with similar dimensions. Usually only one face is smooth, thus usable for contacting, lithography etc... The other side is either covered by the $Bi_{25}FeO_{39}$ phase or its surface is rough.

Chapter 2

Ferroelectric photovoltaics

Nowadays, energies that come from resources which are naturally replenished on a human timescale are needed to decrease our dependency on fossil fuels. Solar energy appears to be one of the most reliable and abundant energy sources which can be used to produce electricity. Photovoltaic systems convert incident photons into flowing charge carriers by taking advantage of the photoelectric effect discovered by Einstein in 1905. After decades of development, there are numerous types of photovoltaic solar cells based on amorphous silicon, dye-sensityzed, organic etc ... which are competing to achieve the best efficiency for the lowest price. Ferroelectrics are thus also natural candidates as they possess the essential necessary ingredients, including the key advantage of an internal built-in electric field. Unfortunately, ferroelectrics have several critical drawbacks including too high bandgaps and recombination rates, which make them noncompetitive for mainstream applications. These materials could however be appealing for some specific applications owing to the multifunctionalities offered by many of them. In particular, they are piezoelectric and some of them even possess magnetic orders.

In this chapter, I will start by describing pn junctions which are used to separate photogenerated charge carriers in standard solar cells. This system is well suited to introduce the fundamental principles of photovoltaic. I will also review the actual knowledge on photoelectric effects in ferroelectric materials to finally discuss our photoelectric studies on mono and mulidomains $BiFeO_3$.

2.1 Semiconductor photovoltaics

A pn junction is formed when a p-type region is placed in close contact with a n-type region in a semiconductor. Since they are doped differently, they have different chemical

potentials and Fermi levels. At the interface between the two regions, the concentration gradient of charge carriers is strong and a diffusion of electrons occurs from the region of high electron concentration (n-type region) to the region of low electron concentration (p-type region) as defined by Fick's law :

$$\mathbf{J_{D_n}} = qD_n\nabla\mathbf{n} \tag{2.1}$$

$$\mathbf{J_{D_p}} = qD_p\nabla\mathbf{p} \tag{2.2}$$

where J_{D_n}, $J_{D_p}$are diffusion currents for electrons and holes respectively, ∇n and ∇p are the concentration gradient and D is the diffusion coefficient for the appropriate charge carrier and is given by Einstein's relation :

$$D = \frac{kT}{q}\mu \tag{2.3}$$

where k is the Boltzmann constant, T the temperature, q the elementary charge and μ the charge carrier mobility. When the electrons diffuse across the p-n junction, they recombine with holes on the p-type side. While charge carriers are exchanged, an electric field is building-up against the diffusion of charge carriers and a depletion region is formed across the interface. The gradient of electric potential which is formed, leads to the apparition of a drift current :

$$\mathbf{J_n} = qn\mu_n\nabla\varphi \tag{2.4}$$

$$\mathbf{J_n} = qp\mu_p\nabla\varphi \tag{2.5}$$

where J_n, J_p are drift currents for electrons and holes respectively, $\nabla\varphi$ is the gradient of electric potential and μ is the mobility of the appropriate charge carrier. J_n and J_p flow in opposite directions.

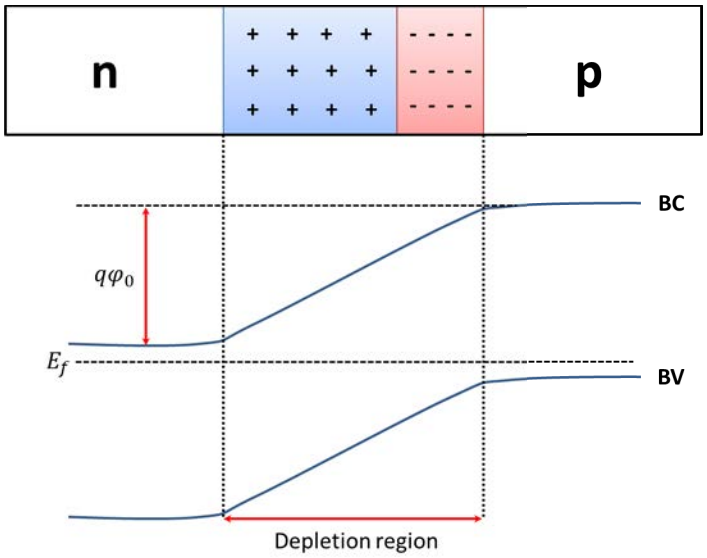

Figure 2.1: Schematics of a pn junction with its associated energy band diagram. φ_0 is the voltage resulting from the imbalance of net charges at both side of the interface and E_f the fermi level.

The width of the depletion region is related to the doping concentration on both sides of the junction and at equilibrium, the drift current due to the built-in electric field exactly compensates the diffusion current. Finally, there remains a net charge ρ at both sides of the interface. Figure 2.2 shows the electric potential φ and the electric field ξ in the pn junction. It depends on the charge density distribution ρ on both sides, and is given by the Poisson's equation :

$$\nabla^2\varphi = -\frac{\rho}{\varepsilon} \tag{2.6}$$

with $\xi = -\nabla\varphi$ and $\varepsilon{=}\varepsilon_0\varepsilon_r$ the material dielectric constant. This description can be extended to all interfaces and especially for metals/semiconductors where a depletion region can be formed in the semiconductor to balance Fermi levels. These interfaces are called Schottky contacts.

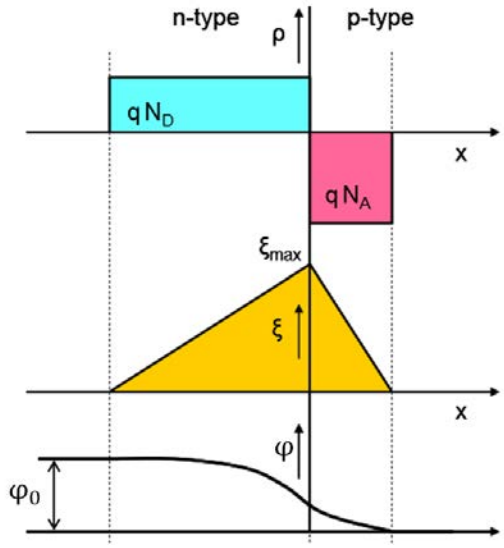

Figure 2.2: Schematics of the electric potential φ, electric field ξ and net charges ρ profiles in the depletion region of a pn junction. φ_0 is the voltage resulting from the imbalance of net charges at both side of the interface.

2.1.1 pn junction in the dark

The current-voltage (I-V) characteristics for a non-illuminated pn junction can be expressed by the equation :

$$J_{dark} = J_s \left[exp(\frac{eV}{k_B T}) - 1 \right] \tag{2.7}$$

where J_s is the saturation current, e the elementary charge value, k_B the Boltzmann constant, T the temperature and V the applied voltage. Depending on the applied bias, I-V curves show two different regimes :

- The forward regime : extra electrons are injected in the n-type region, increasing the diffusion current, and thus decreasing the depletion region and the barrier height.
- The reverse regime : extra electrons are injected in the p-type region, increasing the drift current, and thus increasing the depletion region and the barrier height.

2.1.2 pn junction under illumination

The absorption of a photon of energy greater than band gaps of semiconductor materials, sends one electron of the valence band into the conduction band. This generation of electron-hole pairs leads to an excess of carriers concentration Δn and Δp. The total carrier concentration is then given by :

$$n = n_0 + \Delta n \tag{2.8}$$

$$p = p_0 + \Delta p \tag{2.9}$$

where n_0 and p_0 are the equilibrium concentrations of electrons and holes, respectively. As a result, under illumination, the number of electrons and holes generated increases with time and should tend to infinity without a limiting process. The recombination of the electron-hole pairs, drives the system back towards equilibrium. Generation and recombination are always happening in semiconductors, and their rate are in balance at equilibrium. The recombination processes can be radiative when the electron in the conduction band relaxes into the valence band with the emission of a photon or non-radiative when the energy of the recombination is dissipated (electrons, phonons...). Two main non-radiative recombination processes can be considered :

- The Auger recombination, where the energy is given to a third carrier, which is excited to a higher energy level without moving to another energy band. Its energy is then released to the lattice. Due to the three-particle interaction process, Auger recombination is only significant for high carrier densities.
- The Schockley-Read-Hall (SRH) process, where the recombination occurs through a trap or a deep impurity by a two steps process. First, a conduction electron is captured by an impurity whose level lies deep in the band gap. At a later time, this occupied center may capture a hole from the valence band or equivalently emit an electron into the valance band, finally ensuring the recombination of an electron hole pair. The resulting energy is exchanged with the lattice in the form of phonons. Most crystalline imperfections (impurities, grain boundaries...) can produce states in the band gap. Moreover dangling bonds or defects at the surface also produce localized states with an energy within the band gap which can be very effective recombination states. Localized states can absorb differences in momentum between the carriers, hence they compose the dominant generation and recombination process in indirect bandgap materials. SRH can also dominate in direct bandgap materials under conditions of very low carrier densities.

Taking into account these recombination processes, we can describe the evolution of carrier concentration under illumination as a function of generation G and recombination R rates :

$$\frac{dn}{dt} = \frac{d\triangle n}{dt} = G_e - R_e \tag{2.10}$$

$$\frac{dp}{dt} = \frac{d\triangle p}{dt} = G_h - R_h \tag{2.11}$$

Where G and R are simply related to the lifetime of charge carriers τ, and therefore are closely dependent on the dominant recombination process in the material. However, the presence of an internal electric field, as in pn junctions, allows to separate the electron-hole pairs and thus largely decrease the recombinaison rate (increasing the lifetime of charge carriers). In fact, upon illumination, with an energy higher than the semiconductor's bandgap, electron-hole pairs are generated in both regions. The intrinsic Fermi level is thus split into a quasi fermi level for holes (E_{Fh}) and for electrons (E_{Fe}). Electrons flow from the p-type into the n-type region and holes from the n-type into the p-type region. The flow of the photo-generated carriers causes the so-called photocurrent , J_{ph}.

Ohmic metal-semiconductor contacts are made on both the n-type and p-type sides of the solar cell, and the electrodes connected to an external load. In open circuit condition, no net current flows inside the p-n junction. The photocurrent is balanced by the opposite recombination current. The recombination current will increase through lowering of the electrostatic potential barrier across the depletion region. In short circuit condition, the photocurrent flows through the external circuit and gives rise to the so-called photovoltaic current. The current-voltage (I-V) characteristics for a pn junction under illumination can be expressed by the equation :

$$J = J_s \left[exp(\frac{eV}{k_B T}) - 1 \right] - J_{ph} \tag{2.12}$$

where J_{ph} is the generated photocurrent.

2.2 Ferroelectric photovoltaics

2.2.1 The Bulk Photovoltaic Effect (BPV)

Ferroelectric photovoltaics was discovered in the early 50's with the work of Chynoweth *et al* [42]. They showed the existence in $BaTiO_3$ of a weak pyroelectric current, as well as a steady photocurrent above the Curie temperature. They attributed these phenomena to the electric field related to a surface charged layer which persists above the Curie temperature when the polarization vanishes. It took twenty more years to see the first quantitative studies of the ferroelectric photovoltaic effect. In 1974, Glass *et al.* [43] described the steady photocurrent and the high photovoltage observed in $LiNbO_3$ bulk crystals under illumination by an asymmetric scattering of photoelectrons due to the non centrosymmetry of their materials. The short circuit current J_{sc} is therefore proportional to the intensity I of the monochromatic incident light :

$$J_{sc} = k_1 \alpha I_{light} \tag{2.13}$$

where α is the absorption coefficient and $k_1$is the Glass constant that depends on the material and the energy of the incident photons. The total currents density through materials can be described as :

$$J = (\sigma_d + \sigma_{ph})E \tag{2.14}$$

where E is the applied voltage, σ_d the dark conductivity and σ_{ph} the photoconductivity of the materials. Therefore the photocurrent J will produce an open circuit voltage, V_{oc} :

$$V_{oc} = \frac{Jd}{\sigma_d + \sigma_{ph}} \tag{2.15}$$

with d the distance between the electrodes. According to this equation, ferroelectric crystals, with very low dark conductivity and photoconductivity, should provide very high voltage. This unique characteristic of the ferroelectric photovoltaics devices was called the anomalous photovoltaic effect (APV) and show an outstanding output photovoltage, a few orders of magnitude larger than the bandgap of the ferroelectric materials. A V_{oc} as large as 10^4 volts in some cases [43], was measured in $LiNbO_3$ bulk crystals.

Figure 2.3: (Left) Schematic of measurements of the bulk photovoltaic current in polarized light. (Right) Illustration of the tensorial nature of the bulk photovoltaic current in x, y directions. Reproduced from ref [44]

In order to stress the tensorial nature of the photocurrent (figure 2.3) , one should prefer considering the Glass constant as a third rank tensor which gives the second order optical response of the material[45]. Therefore, in a non-centrosymmetric material, under an incident electromagnetic plane wave :

$$\mathbf{E_i} = \mathbf{e}E_0 e^{i(\mathbf{q}.\mathbf{r}-\omega t)} + \mathbf{e}^\star E_0 e^{i(\mathbf{q}.\mathbf{r}-\omega t)} \tag{2.16}$$

where e, $e*$ are the projection of the polarization vector of the radiation on the crystal axes. The current density in the material can be given by :

$$\mathbf{J_i} = \chi_{ijlm} q_j \mathbf{e_l} \mathbf{e_m^\star} I + \beta_{ijl} \mathbf{e_j} \mathbf{e_l^\star} I \tag{2.17}$$

where the first term is the light entrainment effect and the second term the Bulk Photovoltaic effect (BPV). Phenomenologically, the electric current density j is quadratic in the electric field and the complex photovoltaic tensor β_{ijl} can be separated into a real part which is associated to the linear part of the incident light (LPVE) and a complex part which is associated to the circular part of the incident light (CPVE). The short-circuit current density is thus given by :

$$\mathbf{J_i^{sc}} = \beta_{ijl}^l \mathbf{e_j} \mathbf{e_l^\star} I + i\beta_{il}^c [\mathbf{e} \times \mathbf{e}^\star]_i I \tag{2.18}$$

Since the current density is a polar vector and, therefore, odd under the operation of space inversion, the BPV effect is allowed only in materials that lack inversion symmetry, respectively, in gyrotropic media for CPVE and piezoelectrics for LPVE. Consequently, all non-centrosymmetric materials can exhibit BPV effect and this assumption was largely confirmed experimentally on a large variety of materials including non-ferroelectric materials such as GaP, Te, ZnO or HgS [46]... In 1981, this model was detailed by von Baltz *et al.* [47] with a fully quantum calculation of the scattering of excited electrons, leading to the modern shift current theory.

2.2.2 The shift current theory

Non-symmetric optical excitations in k-space can take place in materials which have no center of symmetry, as ferroelectrics, and leads to a net current flow from the asymmetry of the potential. Bulk polarization is not required (no internal electric field), only inversion symmetry must be broken. Perturbative analysis treating the electromagnetic field classically yields the shift current expression :

$$\mathbf{J_q} = \sigma_{rsq}\mathbf{E_r}\mathbf{E_s} \tag{2.19}$$

where the BPV coefficients can be seen as a product of two terms [48, 49]:

$$\sigma_{rsq}(\omega) = e\sum_{n',n"} \int dk I_{rs}(n', n", k; \omega) R_q(n', n", k) \tag{2.20}$$

with :

$$I_{rs} = \pi(\frac{e}{m\hbar\omega})([n"k] - f[']k])\times < n'k|\hat{P}_r|n"k >< n"k|\hat{P}_s|n'k > \times\delta(\omega_{n"}(k) - \omega_{n'}(k) \pm \omega) \tag{2.21}$$

is the transition intensity, which is also proportional to the imaginary part of the permittivity and thus to the absorption.

$$R_q = -\frac{\partial\phi_{n'n"}(k,k)}{\partial k_q} - [\chi_{n"q}k - \chi_{n'q}k] \tag{2.22}$$

is the shift vector, which gives the direction and the average distance traveled by the coherent carriers during their lifetime. Recently, the modulation of the BPV effect in ferroelectrics was studied by first principle calculation in terms of structural parameters. It was found to originate from :

- Absorption, through the influence of the linear dichroism (birefringence).
- Shift vector direction and magnitude, through electrostatic control of electron density delocalization.

Despite these new insights, the correlation between the shift current mechanism, the structural and the electronic properties of ferroelectric materials is not well understood. Especially the origin of the driving force of the charge carriers separation and transport, which is usually provided by an internal electric field.

2.2.3 Influence of the depolarizing field

In 2009, Choi *et al* [15] reported a diode like effect in $BiFeO_3$ single crystals in a capacitor configuration. Results are shown on figure 2.4a. The forward direction of the diode was closely related to the direction of the polarization and could be reversed by an external electric field. Associated to the diode effect, a steady photovoltaic current was measured and modulated with the incident light polarization. However they only made assumptions on the possible origins of the observed PV effect : Optical rectification, bulk effect, defects assisted or interface based photovoltaic, but none of these explanations totally fitted with the results.

Figure 2.4: (a) J(E) curves of $BiFeO_3$ after +150V, –150V. and +150V pulses, in sequence. The diode forward and reverse directions switch when the direction of out-of-plane polarization (P) is reversed by 150V pulses. (b) Schematic energy band diagrams after upward poling. The electromigration of oxygen vacancies played a role in the polarization switching, the diode like effect and therefore in the photoresponse of each metal/ferroelectric interface. Reproduced from ref [15, 50]

Finally, Yi *et al.* [50] demonstrated that the diode effect is simply due to the remnant depolarizing field induced by the imperfect screening of the polarization charges[51, 22, 52]. The forward direction gives the direction of holes flow and can be reversed with the polarization switching. They have also shown that the electromigration of oxygen vacancies played a role in the polarization switching and thus in the diode like effect as illustrated on figure 2.4b. This observation was used by Moubah *et al.* [53] to measure a diode like effect associated to photocurrent in a planar device of $BiFeO_3$ single crystals (electrodes on top of the same polarization side). By applying an electric field under strong illumination, they managed to move the oxygen vacancies in the direction of the field. The resulting diode like effect which was observed was related to the change of the electrostatic environment of the interfaces induced by the oxygen vacancies. A year later, in 2010, Yang *et al* [16] worked on a periodic domain pattern, in $BiFeO_3$ thin films, and observed a steady photocurrent of $120\mu A/cm^2$ flowing against the net polarization as shown on figure 2.5. Associated to this short circuit photocurrent, they measured an over bandgap photovoltage up to 16V. These effects scale with the number of domain walls and vanish when electrodes are perpendicular to the domain walls. According to their simulations, they ascribed the effect to the potential drop inside the domain walls. Consequently this creates a high electric field in the domain wall which makes an efficient driving force to separate the electron-hole pairs. In the domain, the internal electric field is too low and the recombination rate is high. This model can be seen as an array of standard pn junctions in parallel configuration and

opens new routes for domain wall nanoelectronics. At this time, the role of interfaces, domain walls and depolarizing fields in ferroelectric photovoltaics seemed obvious.

Figure 2.5: Schematics of (a) the perpendicular device geometry and (b) four domains (three domain walls) in an ordered array of 71° domain walls and detailed picture of the build-up of photo excited charges at a domain wall. (c) Corresponding I–V measurements of the perpendicular device geometry. Reproduced from ref [16]

By using an atomic force microscope (AFM) with a conductive tip, Alexe *et al.* [54] attempted to measure the efficiency of charge carriers separation into $BiFeO_3$ domain walls. They found that charge carriers are generated and separated uniformly across the sample regardless of where the tip is lying : on top a domain, or a domain wall. In addition, Ji *et al.* [55] measured a photovoltaic current perpendicular to the ferroelectric polarization in (111) $BiFeO_3$ thin films (figure 2.6a). By using symmetric Au electrodes the effect of interfaces was ruled out and the sinusoidal modulation of photovoltaic current with the incident light polarization, shown on figure 2.6b, remind that the BPV is a part of the photovoltaic effect observed in $BiFeO_3$.

Figure 2.6: (a) Schematic of the epitaxial $BiFeO_3$ thin film with in-plane electrodes and polarization along thickness direction under polarized light. The angle between the polarizer transmission axis and the y axis is ϑ. (b) Normalized J_y at different polarizer angles. Reproduced from ref [55].

By using first principle shift current theory [48, 49], Young *et al.* computed the bulk photovoltaic effect in $BiFeO_3$ [56] and found a good agreement with experimental results. They emphasized that several processes can be part of the photocurrent and thus one has to pay attention to the direction of each components of the photocurrent. The efficiency of ferroelectric photovoltaics should be improved with cooperative rather than antagonistic interaction between different mechanisms : bulk, depolarizing field, domain walls and metal/ferroelectric interfaces which are playing a major role in the measured photocurrent. These observations lead Bhatnagar *et al.* [57] to verify the behavior of samples with stripe domains under linear polarized light illumination. They showed that the photovoltaic current measured in these samples could also show sinusoidal response with respect to the rotation of the incident light polarization. Moreover, they calculate all the BPV tensor coefficients which were consistent with previous calculations. They also observed that contrary to previous observations, 71° and 109° domain walls showed different behaviors in parallel or perpendicular configurations. They concluded that the BPV is the main photovoltaic effect in stripe domain samples. However, the different domain wall conductance leads to a modulation of the

measured photovoltage depending on the orientation of the domain wall with respect to the electrodes.

Figure 2.7: (a) Left. Schematics of a sample showing stripes, which represent the domain walls and how the vector E of the linearly polarized light is aligned with the direction of the current flow J for the perpendicular case. Right. Normalized photovoltaic current measured at different incident light polarization angles for samples with 71° (circles) and 109° (triangles) domains, respectively. (b) Schematic showing the periodic arrangement of domains and domain walls in $BiFeO_3$ thin films for parallel (right) and perpendicular (left) geometry with respect to the domain wall. An equivalent circuit considering that the domains bulk and domain wall have different resistances, R_{bulk} and R_{DW}, is shown for both geometries. Reproduced from ref [57].

2.2.4 Summary and outlook

Ferroelectrics have several critical drawbacks including too high bandgaps and recombination rates, which make them uncompetitive for mainstream applications. In fact, as most of the commonly used ferroelectric materials have a band gap larger than 3eV, only light above the UV edge can be harvested which represents about 3.5% of solar energy. $BiFeO_3$ has a band gap of 2.7eV [58] which makes it more competitive with around 25% of the sun energy harvesting. Moreover $BiFeO_3$ is a most interesting material as it combines, at room-temperature, coupled ferroelectric and magnetic orders, as well as remarkable optical properties. Especially, most oxides have low absorption coefficients, which require thicker samples that possess higher recombinaison rates than thin films and thus a bad charge collection. Whereas $BiFeO_3$ has an absorption coefficient three to four times larger than $BaTiO_3$ or $LiNbO_3$. However, the reports of high output photovoltages, the possible interesting role played by their domain walls, or the direction switching of the photovoltaic current are making these materials reconsidered for targeted applications. For instance, Guo *et al.* [59] demonstrated a novel non-volatile memory array (figure 2.8) based on the photovoltaic effect in $BiFeO_3$. The writing consists in voltage pulses to switch the polarization whereas the read-out signal is given by the sign of the photovoltaic current.

Figure 2.8: Performance of a prototype 16-cell memory based on the cross-bar architecture. (a) Topography of the device with preset polarization direction. Blue: polarization up, red: polarization down. (b) Voc of all 16 cells are indicated. These are measured under 20mWcm2 light. Reproduced from ref [59].

The long date study of ferroelectric photovoltaics has highlighted some physical properties of particular interest such as above band gap photovoltage, domain wall photovoltaics, switchable diode like effect or photocurrent modulation with the incident light polarization. Two main causes stand out of the literature, the depolarizing field and the BPV effect. Despite this relatively well identified phenomenon, the origin of experimental observations remains often under debate. This emphasizes the complexity of photovoltaic processes standing in ferroelectric materials. In fact, disentangling all the photocurrent components is not an easy task but is on purpose to understand and improve the photovoltaic properties of ferroelectric materials.

2.3 Experimental techniques

2.3.1 Scanning PhotoCurrent Microscopy (SPCM)

The Scanning Photocurrent Microscope (SPCM) [13] is a powerful technique to address the photoactive region of a sample. Specifically, a focused laser spot is scanned across the sample surface, while the reflected light and the photocurrent are recorded simultaneously, providing reflection images and a correspondent photocurrent map of the device. The photoresponse can be therefore correlated to its spatial origin.

The setup consists in a original scanning microscope [60] and a picoammeter which communicate via a LABVIEW interface. The whole setup is sketched in figure 2.9. After passing through a linear polarizer and a beam splitter, the laser beam, generated by a red 632nm or blue 405nm laser diode, is highly focused on the sample by a Mitutoyo BD PlanAPO 100 infinity-corrected microscope objective lens at normal incidence. The spot size is expected to be of the order of the wavelength. The polarization of the incident beam can be controlled by rotating a half-wave plate. The sample is mounted on high precision XY translation stages, controlled down to 5 nm steps by dc motors and piezoelectric actuators. The positioning of the studied zone of the sample is made easier thanks to a standard coaxial optical microscope, using a green light emitting diode as a light source and a camera, which allows to optically image the sample over a wide field (few microns).

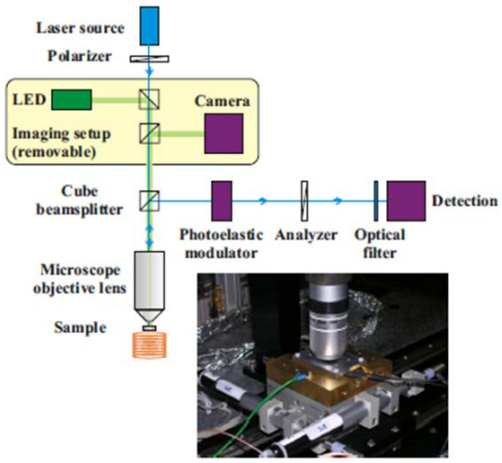

Figure 2.9: Optical scheme of the SPCM setup. The sample is illuminated through a microscope objective lens by a highly focused polarized laser beam. The reflected beam is deviated toward a light intensity detection system, through a photoelastic modulator, an analyzer, and an optical filter. An auxiliary imaging system allows a large scale inspection of the sample. The picture shows the sample environment. Reproduced from ref [60].

Optical measurements at the nanoscale are not possible without an enhanced stability and sensitivity of the measurement setup. The whole setup is thus mounted on a vibration isolated workstation, and thermally regulated at 300 K to avoid thermal shift of optical elements. In order to decrease the residual noise, the polarization state of the laser beam is modulated at a frequency of 50 kHz by a photoelastic modulator. The ellipticity and rotation can be measured at locked high frequencies f and $2f$, respectively, and normalized by the quasicontinuous incoming light intensity. After interacting with the sample, the reflected light beam is deviated by the cube beam splitter, passes through the photoelastic modulator (Hinds PEM-90), the analyzer and an optical filter peaked at the laser wavelength, to finally illuminate a large area silicon photodiode (Hamamatsu S1336-8BQ). The detected signal is made of a DC contribution I_0 and AC components at the fundamental f and harmonic $2f$ frequencies. The normalized magnitudes of AC components, I_f/I_0 andI_{2f}/I_0, are measured thanks to a homemade lock-in acquisition system.

Since the long working distance 6 mm of the microscope objective lens allows the connection of the sample to measurement setups, a Keithley 6487 picoammeter is used to measured the current while the beam is scanning the sample surface. The acquisition process is then operated by an homemade LABVIEW interface where at a given time interval, DC, AC optical signals and electrical current are simultaneously measured. An image reconstruction via step-by-step scanning of the sample under the laser beam is realized. The integration time of the picoammeter, which is the period of time

the input signal is measured has to be well chosen because, it affects the amount of reading noise, as well as the ultimate reading rate of the instrument. Therefore the integration time need to be shorter than the optical measurements sampling to be sure that each current is measured at the right image corresponding position. As a result, this homemade Scanning Photocurrent Microscope allows us to simultaneously measure the reflection image of the sample with the DC signal, as well as the rotation of the light polarization with the AC signal and finally the corresponding photocurrent.

2.3.2 Piezoresponse Force Microscopy (PFM)

The piezzoresponse force microscopy takes advantages from the piezoelectric properties of ferroelectric materials to characterize their domain structures. It is a near field microscopy technique, using a tip to locally measure an interaction with the surface. The PFM analyses the piezoelectric response of a sample to an applied AC voltage between the surface and a bottom electrode. Due to the coupling between strain and an electric field, through the converse piezoelectric effect (CPE), the surface will be deformed depending on the relative sign of the applied voltage and the polarization. The induced deformation is given by :

$$\sigma_{ij} = d_{ijk} E_k \tag{2.23}$$

where σ_{ij} is the strain tensor, d_{ijk} is the piezoelectric third-rank tensor and E_k the applied electric field. The 27 possible coefficients of the piezzoelectric tensor can lead to a quite complex piezoresponse from a material to an applied voltage. Fortunately, in ferroelectric materials, the response can be considered as largely governed by the deformation along the direction of the spontaneous polarization. Therefore, the tip induces a bending of the cantilever where a laser spot is reflected on a quadrant photodiode detector. The position of the laser spot on the photodiode follows the deflection of the cantilever and converts it to an electrical signal. Two measurements can be performed :

- The tip oscillates in the plane and the torsional bending of the cantilever leads to a change in lateral deflection on the quadrant photodiode.
- The tip oscillates out of plane and vertical displacement of the cantilever leads to a change in vertical deflection on the quadrant photodiode.

By using a lock-in amplifier, it is possible to extract the phase and the amplitude of the electrical response, giving rise to images of the ferroelectric domain structures. For

$BiFeO_3$ (001) crystals, the ferroelectric polarization is along the [111] direction which leads to eight possible polarization variants. Consequently, the in-plane and out-of-plane signals are given by the projections of the polarization. For the out-of-plane component, there are only two possible variants which can thus always be determined in a single scan. However for the in-plane signal, the response depends of the scan direction. Therefore, to analyze a sample, one needs to scan in two orthogonal crystallographic direction to fully determine the in-plane component of the ferroelectric polarization.

2.4 Bulk photovoltaic effect in single crystalline $BiFeO_3$

The bulk photovoltaic effect is responsible for a non-trivial behavior of the photoresponse in non-centrosymmetric materials. This results in a modulated photovoltaic current depending on the incident light polarization and the crystallographic direction. In addition, the low conductivity of these materials gives rise to large photovoltages which are much higher than their band gaps. Despite the relatively old research on this topic, the origin of the effect is still under debate, especially its microscopic origin i.e. the driving force on the charge carriers. In fact, it is very complicated to separate the different contributions of the photovoltaic current in ferroelectrics where the bulk component can be small compared to other sources coming from internal electric fields.

In this section, we use the SPCM setup, described above, to study the BPV in a $BiFeO_3$ single crystal. An original electrodes shape allows to measure the photoresponse in all crystallographic directions, without the necessity to rotate the sample, while the incident linear light is fixed. This experiment gives a new insight on the BPV effect and especially on the anisotropic nature of the photocurrent flow and its close relation with the incident light polarization.

2.4.1 Photoelectric measurements

In order to study the BPV effect in $BiFeO_3$ single crystals, one needs to cancel the internal electric fields to ensure that the measured photocurrent will only originate from a bulk effect and not from a classical electric field assisted photovoltaic effect. In $BiFeO_3$ single crystals, the polarization is expected to be efficiently screened to preserve the monodomain state. However, the good quality of our crystals, which show very low leakage current (or strong resistivity), leads to a small internal screening of the ferroelectric polarization. Consequently, an efficient external screening maintains the ferroelectric monodomain state and is provided by a layer of adsorbates or/and metallization of $BiFeO_3$ surfaces. As a result $BiFeO_3$ single crystals provide an appropriate model system to study the BPV effect.

2.4.1.1 Samples selection

Symmetric gold electrodes were deposited on top of $BiFeO_3$ single crystal (001) surfaces. Circular electrodes were fabricated by e-beam lithography and aim at measuring the photocurrent as a function of the crystallographic orientation of the crystal.

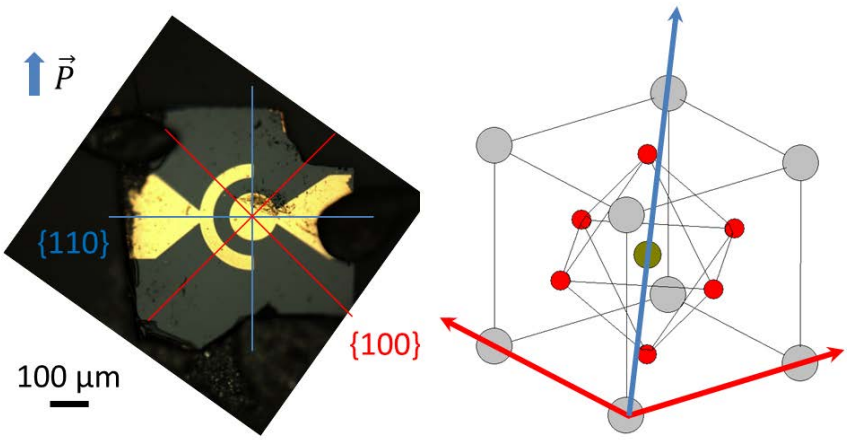

Figure 2.10: Microscope image of the $BiFeO_3$ single crystal (001) surface with two circular shape electrodes. The main crystallographic directions are indicated as they are projected on the surface. The projection of **P** is along the [110] direction. On the right, these main directions are located in the pseudocubic unit cell.

The crystal shown on figure 2.10 has a 40µm wide circular gap and has no bottom metallic contact. PFM images as well as cross-polarized microscope images performed on the surface confirmed the saturated monodomain state and give the main crystallographic orientations. The $Au/BiFeO_3$ contacts lead to schottky barriers at the interfaces and thus localized electric fields in the depletion regions which can be responsible for a photovoltaic current. In ferroelectrics, it is well known that a metal/ferroelectric interface is never perfect and a small roughness can behave as a thin dielectric layer which will decrease the screening of polarization charges at the interface. The resulting imperfect screening of the polarization by top metal electrodes leads to a Schottky barrier height dependent on the ferroelectric polarization direction and magnitude [52, 61, 62]. The difference in barrier height is given by [22, 51]:

$$\Delta\varphi_B = \lambda_{eff}\frac{P_s}{\varepsilon_0} \tag{2.24}$$

Where P_s, ε_0 and λ_{eff} are respectively the spontaneous ferroelectric polarization, the vacuum permittivity, and the effective screening length. The built-in potential at the interface depends on the sign and magnitude of this quantity. In our devices, this results in symmetric contacts which can be ohmic or schottky depending if the polarization is pointing upwards or downwards respectively, as detailed below. Therefore, by choosing the right crystal we expect to minimize the internal electric field and thus observe the BPV effect alone.

2.4.1.2 Macroscopic measurements

We performed current versus voltage measurements in the dark and under macroscopic illumination with a non-polarized white light. These measurements were carried out under a microscope where the light source is used to image and homogeneously illuminate our sample. The electrodes are connected to a Keithley 6487 picoammeter/voltage source which allows us to apply bias and measure the current flow.

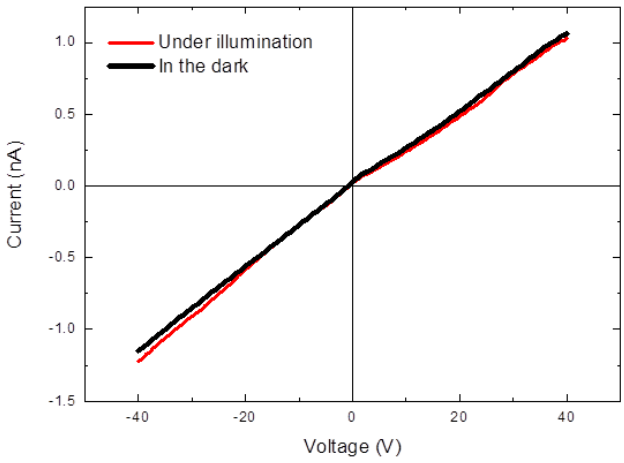

Figure 2.11: The I(V) curves measured in the dark and under illumination show negligible photoconductance and zero voltage photocurrent.

The voltage is ramped from -40V to +40V and the current variation is shown in figure 2.11. The measured I-V characteristics show an ohmic behavior for both curves, from which a global dark resistance (R$\approx 36G\Omega$) can be extracted, indicating that the Schottky barriers at the $Au/BiFeO_3$ interfaces are rather low. As the light is turned on, no photocurrent is observed and the slight shift between both curves is associated to a bulk

capacitance. As long as we measure with a non-polarized macroscopic illumination, the circular symmetry of our electrodes averages all the components of a photovoltaic current coming from the crystal symmetry. Breaking this spatial symmetry by illuminating locally with linear polarized light should allow us to observe the BPV effect. This was done by using the SPCM setup.

2.4.1.3 Spatially resolved photocurrent images

A polarized local illumination is coming from a 405 nm (blue) laser which is focused on the $BiFeO_3$ surface with a spot size around 600 nm and measured density of approximately $3 \times 10^4 W/cm^2$. The $BiFeO_3$ single crystal is placed on a XY translation stage. We then measure the macroscopic current flowing between the two electrodes during scans of the microscopic illumination. We are then able to spatially map simultaneously the optical contrast coming from ferroelectric domains (if present) and the photovoltaic current. Several scans were needed to cover the entire half circular area between the electrodes. Photovoltaic measurements were performed with both electrodes grounded. Resulting images are shown on figure 2.12 and clearly show a photocurrent which is modulated by the crystallographic orientation and the incident light polarization state.

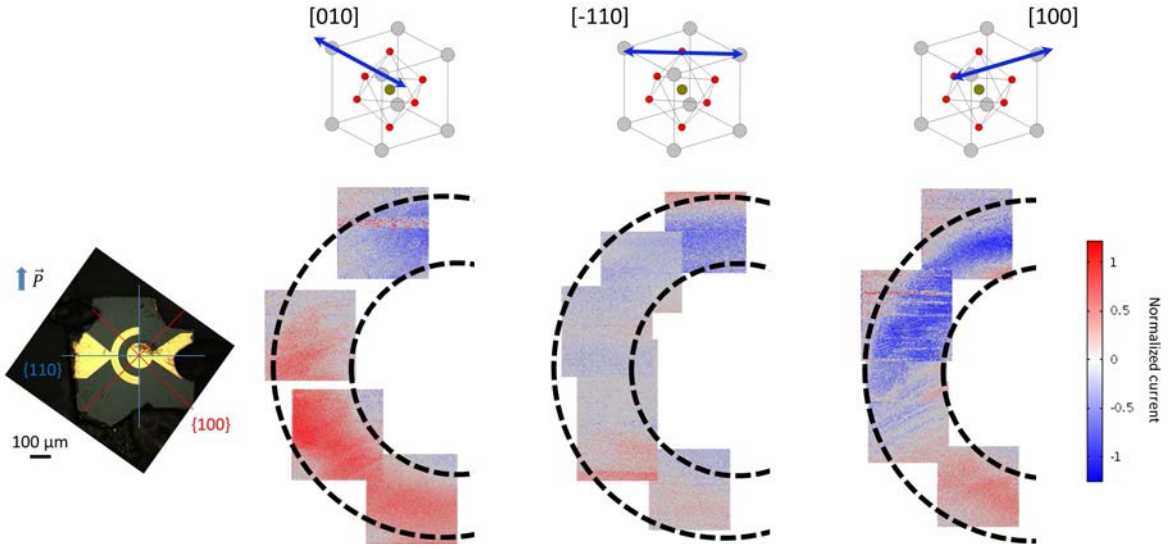

Figure 2.12: Spatially resolved photocurrent images in the circular shape electrodes gap (each frame corresponds to a full scan). Above each set of measurements the schematic orientation of the linearly polarized incident light is represented with respect to the $BiFeO_3$ pseudocubic unit cell. The measured current is modulated by the incident polarized light and the crystallographic direction.

We observe three main behaviors :

- When the polarization of the incident light is along the $[\bar{1}10]$ directions, the measured photocurrent appears to be almost zero everywhere in the gap except, in the direction of the spontaneous polarization.
- When the polarization of the incident light is along the [110] directions, the measured photocurrent appears to be almost zero everywhere in the gap (not shown).
- When the polarization of the incident light is along a {100} direction, the measured photocurrent modulates with the crystallographic orientation and the incident polarization state.

These images clearly show that the photocurrent profile depends on the rotation of the incident light polarization as well as the position along the half circle i.e. the crystallographic direction. A quantitative analysis requires looking at radial line profiles from one electrode to the other one as shown in figure 2.13.

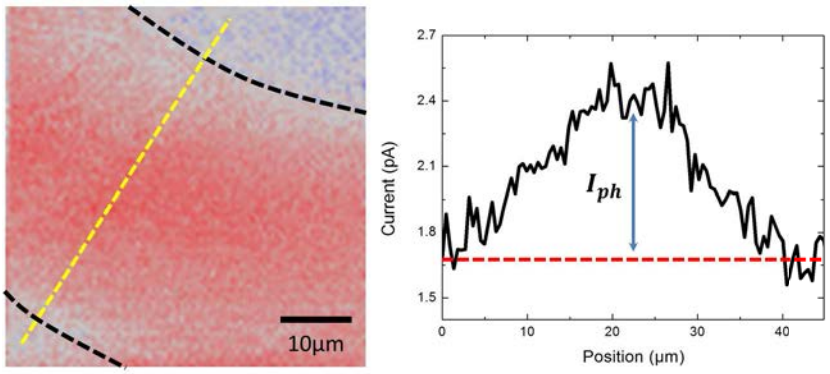

Figure 2.13: A line profile (yellow line) is taken on photocurrent images. The photocurrent is extracted by taking the difference between the base line (red line) and the top of the Gaussian shape profile.

The measured shape of the current with a rather flat maximum halfway between the electrodes, indicates that the observed photocurrent is not coming from a $Au/BiFeO_3$ interface-based photovoltaic process. The fact that it is centered implies that the transport phenomena is balanced between holes and electrons which thus have similar mean free paths. As it is likely that the mean distance traveled before recombination is much shorter that the inter-electrode distance, the yield of collection is expected to be very low. By considering a continuous illumination for each measurement point, we can estimate the yield of collection with a simple diffusion model from a constant source. The concentration of photoelectrons reaching the electrode $N(x,t)$ is thus given by :

$$N(x,t) = N_0 \,\mathrm{erfc}\left(\frac{x}{2\sqrt{Dt}}\right) \tag{2.25}$$

where N_0 is the initial concentration, x the minimal distance between the electrode and the laser spot, D the diffusion coefficient given by the Einstein relation $D = \frac{KT}{q}\mu$ ($\mu \approx 0.1 cm^2/Vs$) and $t = 75\mu s$ is the electrons lifetime from ref [63]. As a result, the ratio N/N_0 gives the yield of collection which is approximately 0.1% for the laser spot positioned in the middle of the electrodes gap (maximum of the signal).

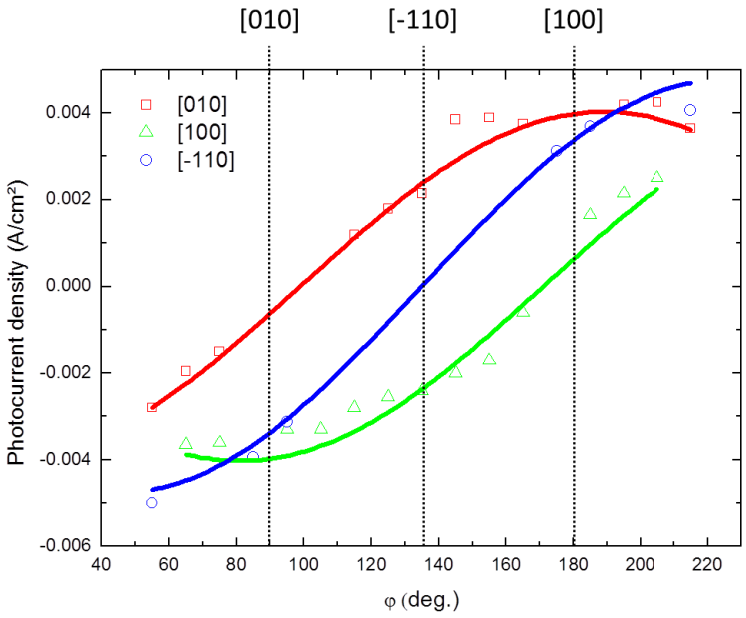

Figure 2.14: Measured photocurrent density versus crystallographic angle for three directions of light polarization. A rotation of 90° of the incident light polarization leads to a shift of 90° of the maximal photocurrent. Lines are the data fitted with the formula described in the following part of this section.

In order to associate a photocurrent value to a crystallographic direction, we have taken the maximal variation of the current along its radial profile. Then, the current density is estimated by considering that the photocurrent flows through a surface given by the product of the spot diameter (500nm) and the absorption depth ($\frac{1}{\alpha}$ =32, 40, 50nm for light polarization parallel to $[\bar{1}10]$, {100}, [110] respectively [54, 64, 41]) as shown in figure 2.16. From this procedure, it is then possible to plot the photocurrent density as

a function of the angle φ and affect a specific crystallographic direction for each value of angle. The results shown on 2.14, show a sinusoidal modulation of the photocurrent with the crystallographic direction. The main direction of current flow is directly visible on the photocurrent map as schematically shown on figure 2.15. Thus, these images show an anisotropic current flow, with the anisotropy direction depending on the light polarization.

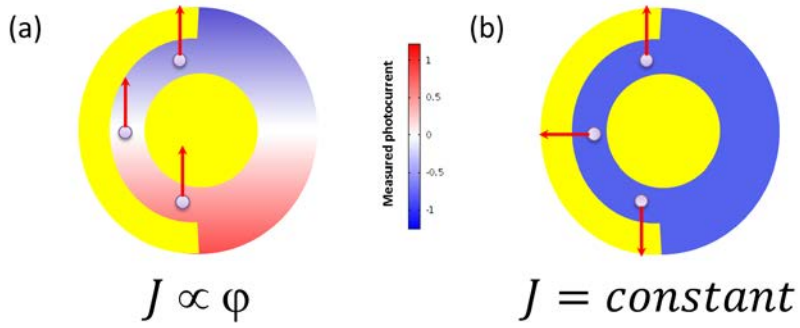

Figure 2.15: Schematics of the measured images depending on the current flow (a) An unidirectional vertically oriented current leads the electrons to be collected by the upper electrode in the upper part of the detector whereas they are collected by the middle electrode in the lower part. This results in an opposite contrast between the lower part and the upper part of the detector which indicates the direction of the current flow. (b) An isotropic current flow leads the electrons to be collected by the same electrode, resulting in no contrast.

2.4.2 Bulk photovoltaic calculations

The observed behavior of the photocurrent is in good agreement with the BPV effect. In order to confirm this statement, measurements have to be fitted with the BPV model. The incident linear polarized light induces a photocurrent given by :

$$j_i^{sc} = \beta_{ijl}^{l} e_j e_l I_{light} \tag{2.26}$$

where β_{ijl} is a third rank tensor which has the symmetry of the crystal. $BiFeO_3$ belongs to $R3c$ space group and gives in Voigt notation :

$$\begin{pmatrix} 0 & 0 & 0 & 0 & \beta_{15} & -\beta_{22} \\ -\beta_{22} & \beta_{22} & 0 & \beta_{15} & 0 & 0 \\ \beta_{31} & \beta_{31} & \beta_{33} & 0 & 0 & 0 \end{pmatrix} \tag{2.27}$$

where many of the 27 elements of the third rank tensor are reduced to zero owing to symmetry operations. Generally the $BiFeO_3$ symmetry is considered in the hexagonal coordinate system which could be relevant for sample with (111) pseudocubic surface. In our case, the laser spot hits the (001) pseudocubic surface and therefore we need to rotate the matrix to match with our experiment. We used the methodology introduced in Ref [57] to calculate the J_x, J_y current densities. The β_{ijl} third rank tensor can be rewritten as :

$$\begin{pmatrix} 0 & -\beta_{112} & \beta_{113} & -\beta_{211} & 0 & 0 & \beta_{311} & 0 & 0 \\ -\beta_{121} & 0 & 0 & 0 & \beta_{222} & \beta_{223} & 0 & \beta_{322} & 0 \\ \beta_{131} & 0 & 0 & 0 & \beta_{232} & 0 & 0 & 0 & \beta_{333} \end{pmatrix} \tag{2.28}$$

The following matrix is used to transform the β_{ijl} third rank tensor from hexagonal to pseudocubic coordinates :

$$R = \begin{pmatrix} \frac{-1}{\sqrt{2}} & \frac{1}{\sqrt{6}} & \frac{1}{\sqrt{3}} \\ \frac{1}{\sqrt{2}} & \frac{1}{\sqrt{6}} & \frac{1}{\sqrt{3}} \\ 0 & \frac{2}{\sqrt{6}} & \frac{1}{\sqrt{3}} \end{pmatrix} \tag{2.29}$$

with the transform operation given by :

$$(\beta_{pqr})_{pc} = \sum_{\substack{ijl \\ 1}}^{3} R_{pi} R_{qj} R_{rl} (\beta_{ijl})_h \tag{2.30}$$

The incident light propagates along the $[001]_{pc}$ axis and thus the $(\beta_{pqr})_{pc} e_j e_l$ term will be reduced to a few coefficents :

$$\begin{pmatrix} \beta_{11} & \beta_{12} & \beta_{13} & \beta_{14} & \beta_{15} & \beta_{16} \\ \beta_{21} & \beta_{22} & \beta_{23} & \beta_{24} & \beta_{25} & \beta_{26} \\ \beta_{31} & \beta_{32} & \beta_{33} & \beta_{34} & \beta_{35} & \beta_{36} \end{pmatrix} \begin{bmatrix} {e_1}^2 \\ {e_2}^2 \\ 0 \\ 0 \\ 2e_1e_2 \end{bmatrix} = \begin{pmatrix} {e_2}^2\beta_{12} + {e_1}^2\beta_{11} + 2e_1e_2\beta_{16} \\ {e_2}^2\beta_{22} + {e_1}^2\beta_{21} + 2e_1e_2\beta_{26} \\ {e_2}^2\beta_{32} + {e_1}^2\beta_{31} + 2e_1e_2\beta_{36} \end{pmatrix} \tag{2.31}$$

Finally, after applying the transform operation and easy trigonometric transformations, the photocurrent along the x and y axes are given by :

$$\begin{cases} J_x = & I_{light}\eta\left[A + Bcos(2\theta) + Csin(2\theta)\right] \\ J_y = & I_{light}\eta\left[A - Bcos(2\theta) + Csin(2\theta)\right] \end{cases} \tag{2.32}$$

With :

$$\begin{cases} A = & -\frac{\beta_{22}}{3\sqrt{6}} + \frac{\beta_{15}}{3\sqrt{3}} + \frac{2\beta_{31}}{3\sqrt{3}} + \frac{\beta_{33}}{3\sqrt{3}} \\ B = & \frac{\beta_{15}}{\sqrt{3}} - \frac{\beta_{22}}{\sqrt{6}} \\ C = & \frac{2\beta_{22}}{3\sqrt{6}} + \frac{\beta_{15}}{3\sqrt{3}} - \frac{\beta_{31}}{3\sqrt{3}} + \frac{\beta_{33}}{3\sqrt{3}} \end{cases} \tag{2.33}$$

I the intensity of the incident light, η the yield of collection and θ the angle between the crystal axis y and the incident light polarization. The obtained formula allows us to calculate the expected BPV current in the x, y crystal directions ([100], [010]). The photocurrent in all crystallographic directions is thus given by the projection of J_x and J_y on the direction of the measurement as illustrated in figure 2.16.

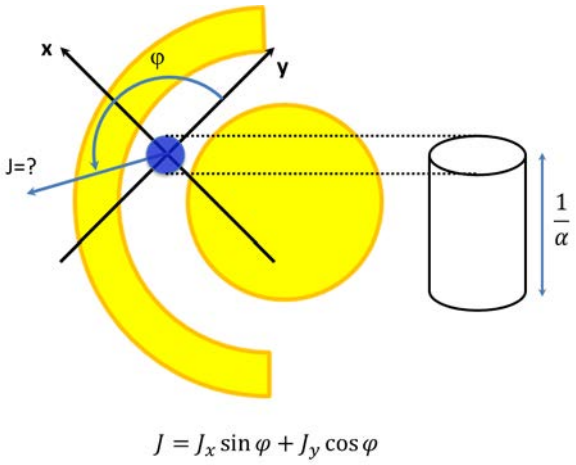

Figure 2.16: Schematic of the model used to calculate the BPV current density. The measured photocurrent in one direction is the projection of the J_x and J_y BPV components on the direction of the measurement. The generated photocurrent flows through a surface given by the product of the absorption depth $\frac{1}{\alpha}$ [54] and the spot diameter d.

where φ is the angle between the x axis and the measured direction i.e. the crystallographic direction. The R-variant is then rotated in order to coincide with the crystal polarization variant and a minus sign is introduced in front of the formula for the reverse connection of the picoammeter. Finally, this leads to the expression below :

$$J_{BPV} = I_{light}\eta\,[[-A + Bcos(2\theta) + Csin(2\theta)]sin(\varphi) + [-A - Bcos(2\theta) + Csin(2\theta)]cos(\varphi)] \tag{2.34}$$

where J_{BPV} is the current density, and A, B, C the fit parameters associated to the BPV coefficients for θ, the direction of the light polarization, along three crystal directions ([100], [010] and [$\bar{1}$10]).

This formula is found to give a very satisfactory fit to our results, as shown on 2.14. The extracted coefficients, can be found in table 2.1 which reproduce quite well our results. The θ is found for each curve and coincides with the experimental rotation with a slight variation of 1.5°.

A	B	C
$7.7 \times 10^{-5} A/cm^2$	$-5.6 \times 10^{-5} A/cm^2$	$3.6 \times 10^{-5} A/cm^2$

Table 2.1: Fit parameters

Based on the reported value of $\beta_{15} = 0V^{-1}$ given in supplementary materials of ref [56], we thus calculate all the associated BPV coefficients :

Theoreticalβ from ref [56]	Experimental β
$\beta_{22} = 2 \times 10^{-4} V^{-1}$	$\beta_{22} = 1.4 \times 10^{-4} V^{-1}$
$\beta_{15} = 0V^{-1}$	$\beta_{15} = 0V^{-1}$
$\beta_{31} = 1.6 \times 10^{-4} V^{-1}$	$\beta_{31} = 1.7 \times 10^{-4} V^{-1}$
$\beta_{33} = 3 \times 10^{-4} V^{-1}$	$\beta_{33} = 1.6 \times 10^{-4} V^{-1}$

Table 2.2: Comparison between experimental and theoretical BPV coefficients (β)

which are in good agreements with the previously measured coefficient values in ref [55] and also calculated in ref [56].

We plot the expected shift current density on figure 2.17 in polar coordinates and reveal the current anisotropy given by the symmetry. According to our measurements, we observe three main directions of the current flow depending on the incident light polarization and nicely observed on our images. The current directions are associated

to a pure BPV effect with the current flowing in the direction of the polarization. For incident light polarization along the [110] directions, the photocurrent amplitude is under the detection limit of our setup and explain why no photocurrent was measured in this direction.

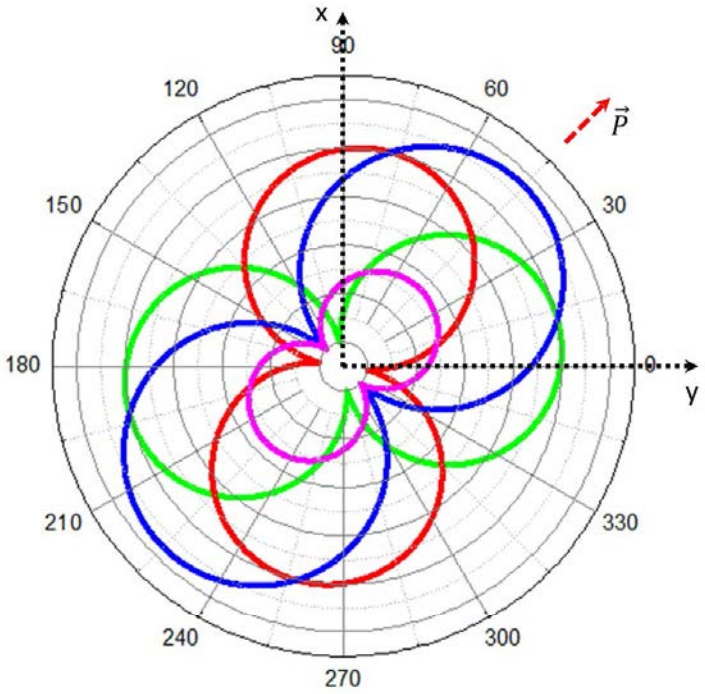

Figure 2.17: Polar representation of the calculated BPV current density in $BiFeO_3$ single crystal. The direction of the current anisotropy depends on the incident light polarization represented by the two different colors.

These calculations also emphasize that our electrodes geometry associated to the SPCM setup allows to directly image the BPV current anisotropy.

2.4.3 Multi-domain state

When a large voltage is applied between the electrodes, it is possible to generate a multidomain state. The photovoltaic response of each domain depends on the new direction of **P** as well as the internal electric fields.

After an electric field around $1 \times 10^5 V/cm$ was applied, the new ferroelectric domain structure between the electrodes is shown in figure 2.18. The resulting structure consists in two main domains where the polarization rotates by 180° between the upper part and

the bottom part of the detector. Thus, a 180° domain wall separates the two parts of the detector in the region corresponding to a measurement direction perpendicular to the polarization i.e. the maximal amplitude of the photocurrent modulation between two incident light polarization (2.14). Locally, smaller domains can be seen. This results in a quite complex structure with three types of domain walls : 71°, 109° and 180°. Nevertheless, the in-plane polarization has only two orientations along +/- y as shown on figure 2.18.

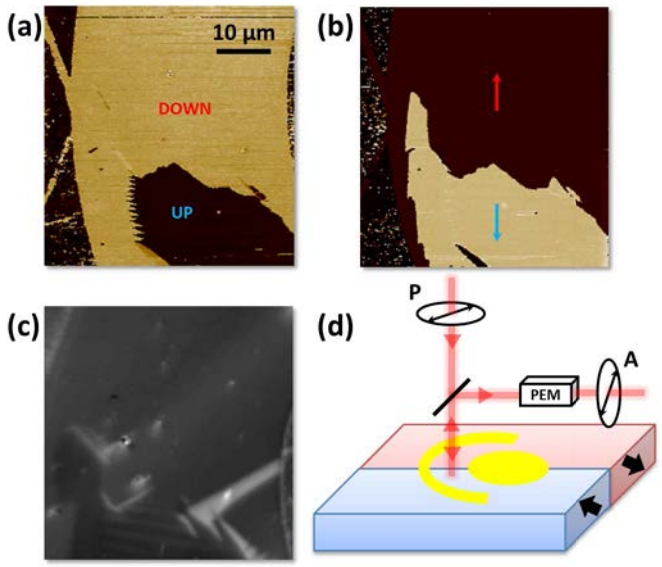

Figure 2.18: (a), (b) Out of plane and in plane PFM images which show globally two domains with 180° rotated ferroelectric polarization. (c) The corresponding scanning microscope image which shows extra features as buried planar domains (bright contrast). (d) Schematic representation of the SPCM measurement configuration with the region of interest in the middle of the detector.

In order to determine the role played by the ferroelectric polarization on the PV effect, we focus on the [100] and [010] directions of the photocurrent obtained for [010] and [100] incident light polarization respectively and associated to a pure BPV photocurrent. Theoretically, the 180° domain structure has to show no difference on the BPV photocurrent between the two domains and should lead to an even contrast on images with both domains. Resulting SPCM images taken in this region for different incident light polarizations are shown on figure 2.19.

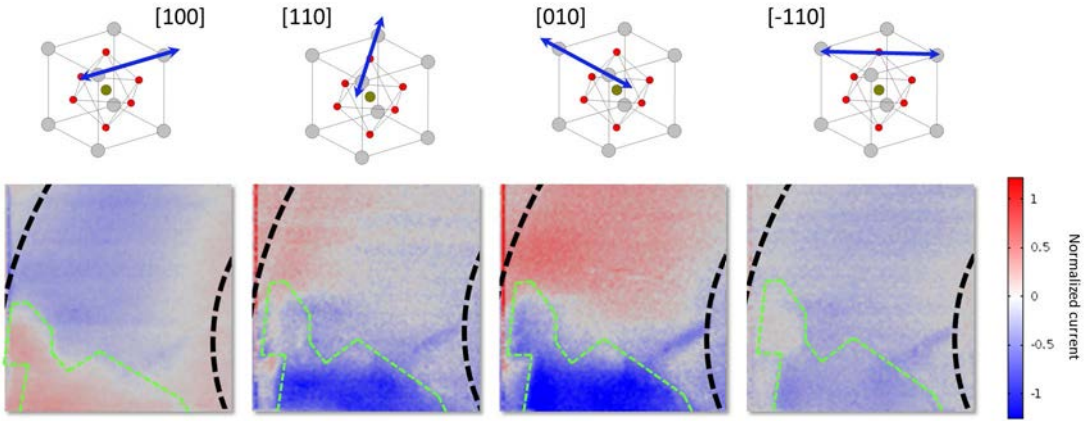

Figure 2.19: SPCM images of the region with the maximal amplitude of the photocurrent modulation. The green dash line follows the domain wall between the up and down oriented domains. The photocurrent is modulated by the incident light polarization with an opposite magnitude between the domains. A more complex behavior is associated to the light polarization along the [110] and [$\bar{1}$10].

For light polarization along [100] and [010], an opposite contrast is observed. Therefore the direction of the current flow is in opposite directions and unambiguously reveals the role of the polarization in the PV effect which gives the direction of the current flow.

For light polarization along [$\bar{1}$10] and [110], surprisingly, a PV current is measured. We attribute this photocurrent to the depolarizing field associated to the complex domain structures.

2.4.4 Conclusions

In conclusion, we have shown that the photocurrent depends both on the incident light polarization and the crystallographic directions. More than the current value, it is the direction of the current flow which rotates with the incident light polarization. This is consistent with the shift current theory and the so-called shift vectors gives the main directions of current flow linked to the direction of the light polarization. We succeeded in measuring a contribution of the BPV current which is not in the direction of the polarization and our electrodes geometry associated to the SPCM setup allows to directly image the current anisotropy i.e the shift vector direction. Finally, by switching the polarization we have been able to show that the ferroelectric polarization gives the direction of the current flow.

2.5 Photovoltaic response around a single 180° domain wall in single crystalline $BiFeO_3$

Ferroelectrics are natural candidates [65] for photovoltaic applications as they possess an internal built-in electric field [15]. This is a key advantage as one does not need to tailor the electric field using electronic band bending at an interface such as in a pn junction. Unfortunately, ferroelectrics have several critical drawbacks including too high bandgaps and recombination rates, which make them uncompetitive for mainstream applications [14]. However, the reports of high output photovoltages and the possible interesting role played by their domain walls are making these materials reconsidered for targeted applications[66, 16, 6]. In fact, large photovoltages were observed in thin films with a high density of striped domains (figure 2.5). The effect was thought to be induced in the domain-walls themselves because of the presence of significant band bending exactly in these entities. However it was argued the BPV effect could be at the origin of the observed behavior [57]. The exact role played by domain walls is therefore subject to controversy.

This section aims at measuring the photoresponse of a single domain wall in a $BiFeO_3$ single crystal. After controlling the nucleation of a domain wall between two electrodes, we will use the SPCM setup to locally map the photocurrent around the domain wall.

2.5.1 Samples and macroscopic measurements

The sample used in the present study is a high quality $BiFeO_3$ single crystal grown as detailed in chapter 1. It has the form of millimeter sized platelets with the short dimension along the [001] direction. The as grown sample is a ferroelectric monodomain with the polarization along the [111] direction. 40nm thick gold electrodes were deposited by electron beam evaporation using e-beam lithography in the pattern shown in figure 2.20a. The electrodes are spaced by 10µm and compose the plus and minus in an electrical circuit consisting of a voltage source and a picoAmpmeter. The sample is first globally illuminated in a conventional wide-field microscope to which a HeNe Laser beam (λ= 632 nm) is coupled and focused to illuminate (with an estimated density around $1kW.cm^{-2}$) the entire region between electrode E_1 and E_2 (figure 2.20b). The voltage is ramped back and forth between -40V and +40V and the current variation is shown in figure 2.20c.

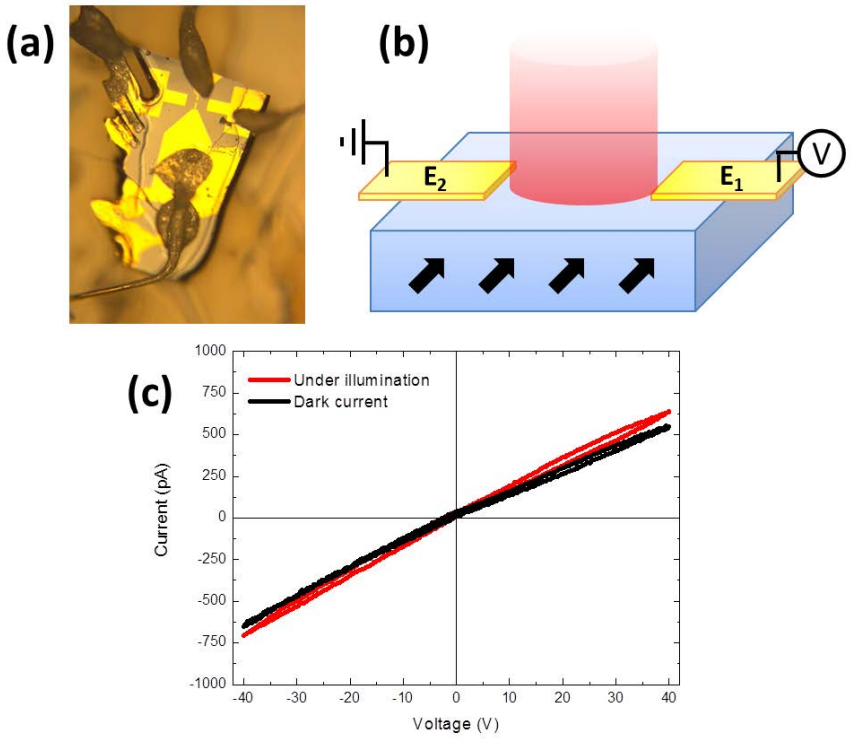

Figure 2.20: a) Single domain crystal of $BiFeO_3$ with Au electrodes deposited on top. b) Schematics of the measurement geometry where the laser light is shun in between the electrodes. c) The I(V) curves measured in the dark and under illumination show a small photoconductance with negligible zero voltage photocurrent.

The measured I-V curves show an Ohmic behavior, from which a global bulk resistance ($R \approx 68\ G\Omega$) can be extracted, indicating that the Schottky barriers at the Au/$BiFeO_3$ interfaces are rather low. In this geometry, two Schottky junctions are indeed established at the gold interfaces with crystalline $BiFeO_3$ in a head to head geometry. The low barrier height obtained here indicates that the direction of the $BiFeO_3$ polarization is such that it generates positive bound charges imperfectly screened by the metal electrodes [52, 61, 51]. Thus, the induced depolarizing field decreases the built-in field at the interfaces resulting in negligible internal electric field as depicted on figure 2.21.

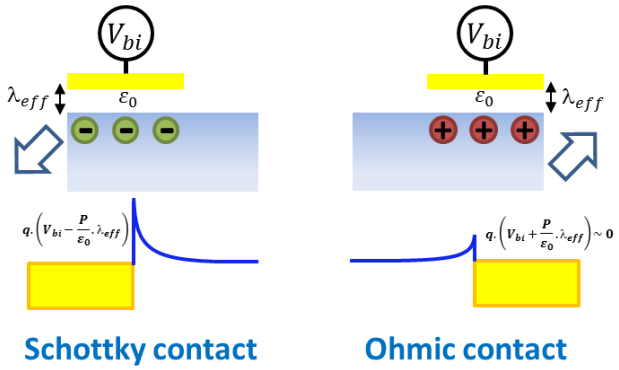

Figure 2.21: Imperfect screening at the $Au/BiFeO_3$ interface. Depending on the orientation of the polarization under the electrode, the contact can be Schottky or Ohmic.

As the light is turned on, a slight photoconductive effect appears at high voltage but no photovoltaic current is observed at 0V. Considering the physical mechanisms at play in a typical photovoltaic device, we attribute this phenomenon to the absence of an internal electric field separating the light induced electron-hole pairs. This observation corroborates the imperfect screening of the polarization charges by the electrodes.

In order to study the effect of ferroelectric domain walls, the originally single domain $BiFeO_3$ single crystal must be partially reversed. The procedure applied here was to ramp back and forth a voltage applied across the electrodes, generating an electric field around $\pm 2.5 \times 10^5$V/cm. After several cycles, the I(V) curves were found to be strongly modified as shown in figure 2.22c. Beside the capacitance associated to the measurements in the dark, one can clearly see, under illumination, the hysteretic behavior often associated to the presence of multidomain states [67]. Interestingly, the negative voltage part of this curve is almost reversible and coming back to zero, an open circuit voltage around 1.3V can be observed associated to a photovoltaic current of 0.7 pA. When coming from large positive values, the open circuit voltage is 4.6V and the photovoltaic current 4.5pA. We qualitatively attribute this behavior to a multidomain state inducing the presence of an uncompensated internal field.

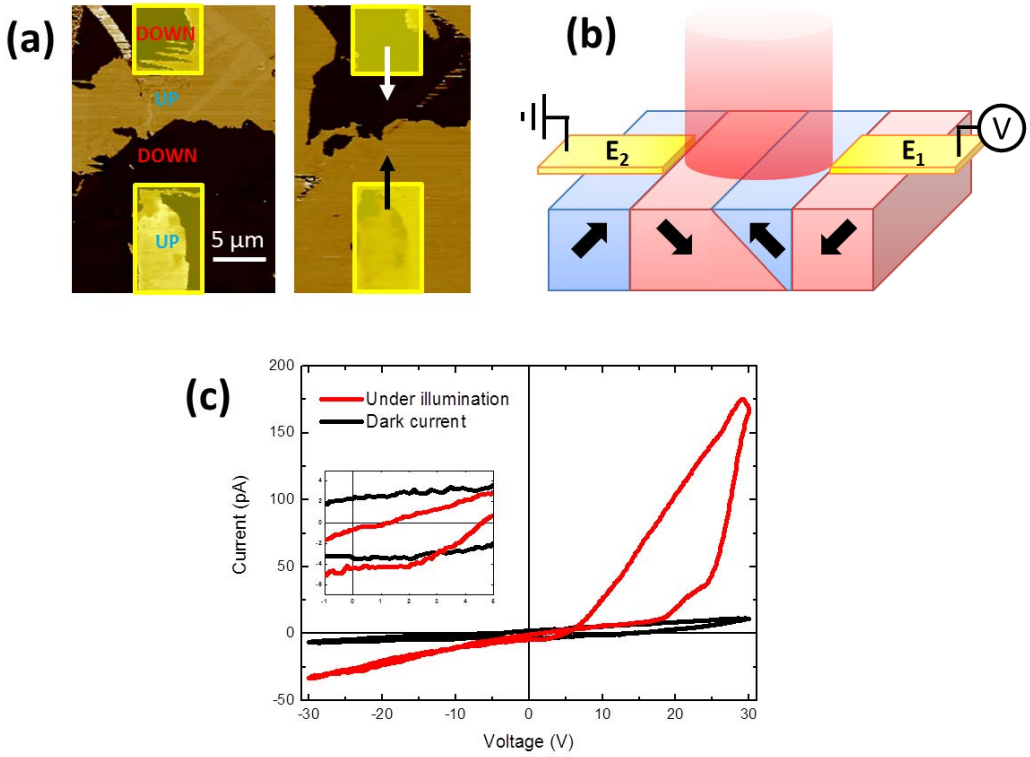

Figure 2.22: a) PFM images of the sample with perpendicular and planar contrasts after sweeping the electric field between the electrodes, evidencing the polarization configuration schematized in b). c) The I(V) curves have dramatically changed as under illumination, a large and hysteretic current appears at positive voltages. In inset: hysteretic zero voltage currents and open circuit voltages appear which depend on the polarization history.

At this point, the inhomogeneous nature of the ferroelectric configuration has to be precisely determined. Therefore, piezoelectric force microscopy has been carried out both in-plane and out of plane. As a result, one can see in figure 2.22 that under the electrodes, the polarization is pointing downwards under E_1 and upwards under E_2 indicating a change in the nature of the metal/ferroelectric contact. We can also observe that both contrasts are reversed on each side of a domain wall located roughly midway between the electrodes. Thus, as the polarization near one of the electrodes switched, a unique domain wall separating two 180° domains propagated between the electrodes, generating this model system.

This domain configuration is consistent with finite elements calculated electric fields in the monodomain where the electric field is mostly along the z axis under the electrodes, generating the antisymmetric contact, and mostly along x between the electrodes in-

ducing the 180° domain wall after sweeping the voltage as depicted on figure 2.23.

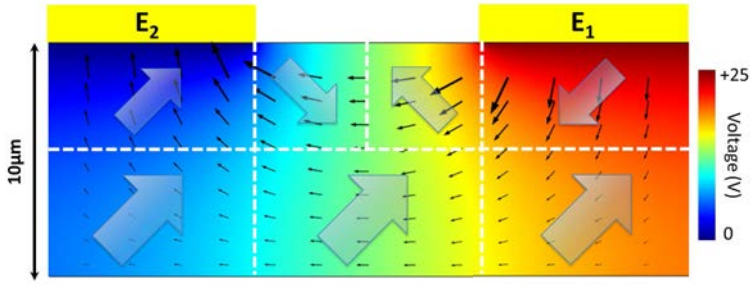

Figure 2.23: Finite elements calculation of the electric field in monodomain $BiFeO_3$. Black arrows show the direction and the magnitude of the electric field. Blue arrows indicate the resulting polarization in the domain pattern.

In addition, one can see that the intensity of the electric field quickly decreases with the thickness of the crystal. This indicates that the induced domain pattern is confined in around 5µm under the crystal surface.

2.5.2 Spatially resolved photocurrent images

In order to disentangle the exact role played by domain walls in ferroelectric and conduction properties of $BiFeO_3$, it is important to carry out local measurements in the vicinity of these entities. Considering the widespread use of scanning probes, it is convenient to use a conducting tip [54] to perform a mapping of the currents induced by a global illumination. Such studies have allowed to underline the special role of the tip in concentrating the local electric field thereby significantly amplifying the photocurrent collection . This technique is therefore well suited to studying the local collection of the globally generated photocurrent. In order to investigate the local electron-hole pair generation and separation, it would however be more appropriate to illuminate locally and collect the entire photogenerated charges.

We used the scanning photocurrent microscope to spatially map the photovoltaic response of our sample. The experimental setup is schematically shown on figure 2.24a and for each position of the laser spot, two quantities are measured : the polarization rotation of the reflected light and the photocurrent collected by micron sized electrodes

deposited in the vicinity of the scanned area. The first gives an image of the polarization domains while the second maps the local photocurrent generation. This technique provides, in a unique fashion, an interesting way to study the role of domain walls and metal/ferroelectric interfaces on photovoltaic properties. The corresponding optical polar rotation of the reflected light recorded while scanning the laser spot is shown in Figure 2.24b,c. As expected, no contrast is obtained between the two domains. However, a dip in intensity can be observed at the domain wall position as locally, the average polarization goes to zero. The optical image of the domain wall could be correlated to the presence of oxygen vacancies in the vicinity of the domain wall which changes the local optical index of $BiFeO_3$ [68].

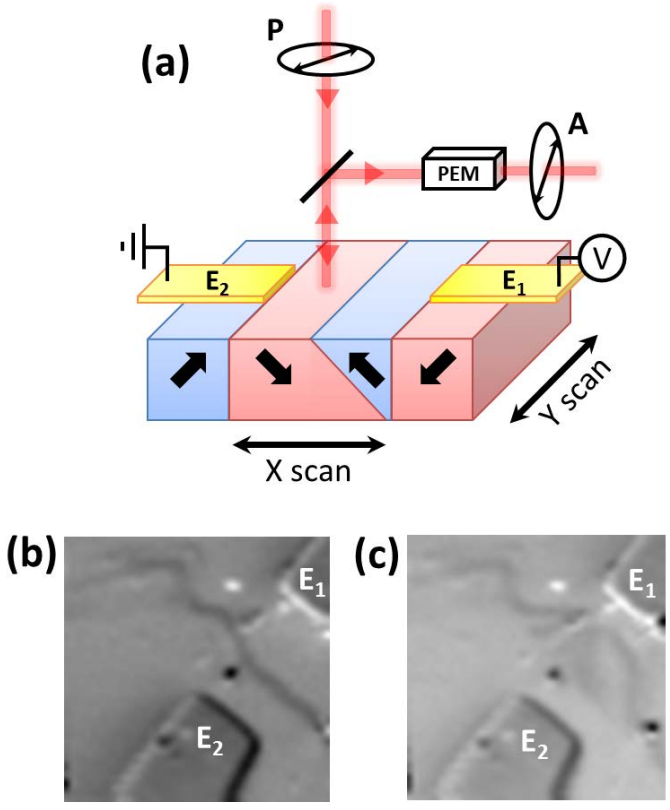

Figure 2.24: Schematics of the optical measurement where a focused laser spot is scanned on the sample and two quantities are recorded including the change of light polarization and the current extracted through the electrodes. The latter allows to map the photocurrent generation while the former gives the ferroelectric domain configuration as shown on the two images where the dark line corresponds to the domain wall.

This configuration is ideal for local photovoltaic measurements in order to disentangle

the possible contributions stemming from the presence of the 180° domain wall. The scanning photocurrent microscope developed here is the ideal tool to locally illuminate the $BiFeO_3$ crystal between the electrodes as a voltage is applied. Thus, it is optically possible to locate the 180° domain wall during electric field sweeps and it is observed that the domain wall moves hysteretically in between two positions :

- When the domain wall is in the middle of the electrodes' gap, cf. figure 2.24b, the photocurrent is low.

- When the domain wall is distorted close to electrode E_1, cf. figure 2.24c, the photocurrent is high.

The corresponding real time photocurrent images which are summarized on figure 2.25, are very instructive. For the 0V image where the domain wall is positioned in the middle of the gap, the current is mainly generated when the exciting spot is close to electrode E_1 and extending over about 2µm. This is consistent with the existence of a depletion region, stemming from a Schottky barrier at the Au interface, resulting from the polarization switching. In fact, the imperfect screening of the negative polarization charges increases the built-in field at the interfaces as shown on figure 2.21 and induces a Ohmic to Schottky contact transition under E_1. For negative (reverse) bias, this depletion region grows continuously. This correlates with our observations for the photocurrent maps and validates that it originates from this depletion. For positive (forward) bias below V_{oc}, this region shrinks and vanishes, which confirms the Schottky nature of the observed photovoltaic effect. Above V_{oc} a significant photocurrent is located between the electrode E_1 and the domain wall, with an opposite value. When the applied voltage exceeds 25V, the center of the domain wall abruptly moves to a new equilibrium position while its left and right parts remain pinned. Thus, the domain wall in this configuration is distorted [69] and a clear variation of the photocurrent is observed. It is now much more intense and it is located on the left part of the domain wall, towards the E_2 electrode. When the voltage is ramped back to zero, the domain wall keeps the same position and the photocurrent comes back close to E_1 with a different photocurrent shape and intensity. Hence, this hysteretic behavior leads to two very different states at zero voltage, depending on whether one comes back from positive or negative bias. These 0V images are directly comparable as in both cases no electric field is externally applied. The main difference here is the position of the domain wall which can thus induce a fundamental difference in the photocurrent generation.

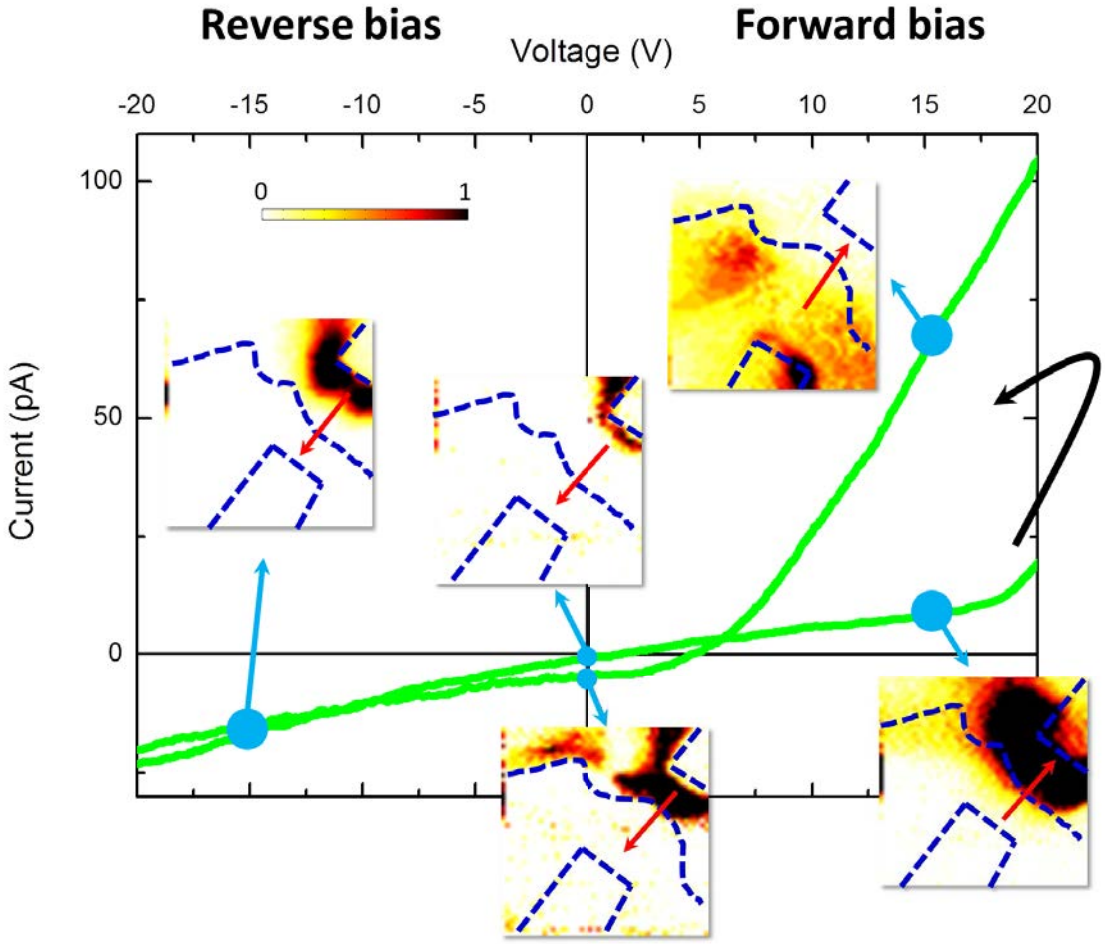

Figure 2.25: The SPCM images obtained during voltage sweeps show a hysteretic photocurrent associated to the position of the domain wall which follow the macroscopic I-V characteristic. Red arrows indicate the direction of the electrons flow. For clarity, the color contrast is not in absolute value but it shows clearly that the photocurrent is generated in different regions depending on the exact position of the DW.

We take this as evidence that the internal field is completely rearranged because of the domain wall position and in turn generates different conditions for the electron-hole pairs' separation. Another, more straightforward, conclusion from the measurement is that one cannot see any specific contribution of the domain wall itself, i.e. when the scanned light spot touches the domain wall line. Instead, the photocurrent is always located a little away from the domain wall which leads us to conclude that as an entity, this 180° domain wall is not a region of enhanced photovoltaic effect. This result is not consistent with the conclusions reached in ref [16] as it rather points to the importance

of the bulk region in the vicinity of the domain wall. We attribute this to the effect of the internal field.

2.5.3 Calculations and discussions

In order to confirm this last point, we carried out numerical simulations of the electric fields generated in our sample and schematically described in figure 2.26. By using a commercial 3D finite elements software, we solved the Poisson equation :

$$\nabla^2\varphi = -\frac{\rho}{\varepsilon} \tag{2.35}$$

for boundary conditions which are described below.

First, our Schottky contact is simulated taking a built-in potential (V_{bi}) value of -0.9 eV [58]and a 3D configuration mimicking that of our sample with two Au/$BiFeO_3$ interfaces. We simulate the barrier using an effective dielectric layer with a screening length λ_{eff} around 1nm. In order to reproduce the observation that the Au/$BiFeO_3$ contact goes from Schottky to essentially Ohmic when polarization is reversed, one needs a positive bound charge of about 1% of the full $BiFeO_3$ polarization, i.e. an incomplete screening of 99%. The obtained Schottky contact has a barrier height of -1.8V, in reasonable agreement with the -1.3V that we measure. The length of the depletion region is estimated from the 0V measurement of figure 2.25 where the photocurrent is located on a 2µm distance from the Au electrode. Considering oxygen vacancies as the main doping contribution in $BiFeO_3$, one needs around $1 \times 10^{15} cm^{-3}$ oxygen vacancy concentration to reproduce the width of the depletion region. Finally the simulation map of the internal electric field gives a strongly localized field close to the Schottky contact, in the predefined depletion region as shown in figure 2.26.

In the reverse regime, the electric field stays confined in the depletion region which grows with the applied electric field. This is also called the desertion regime.

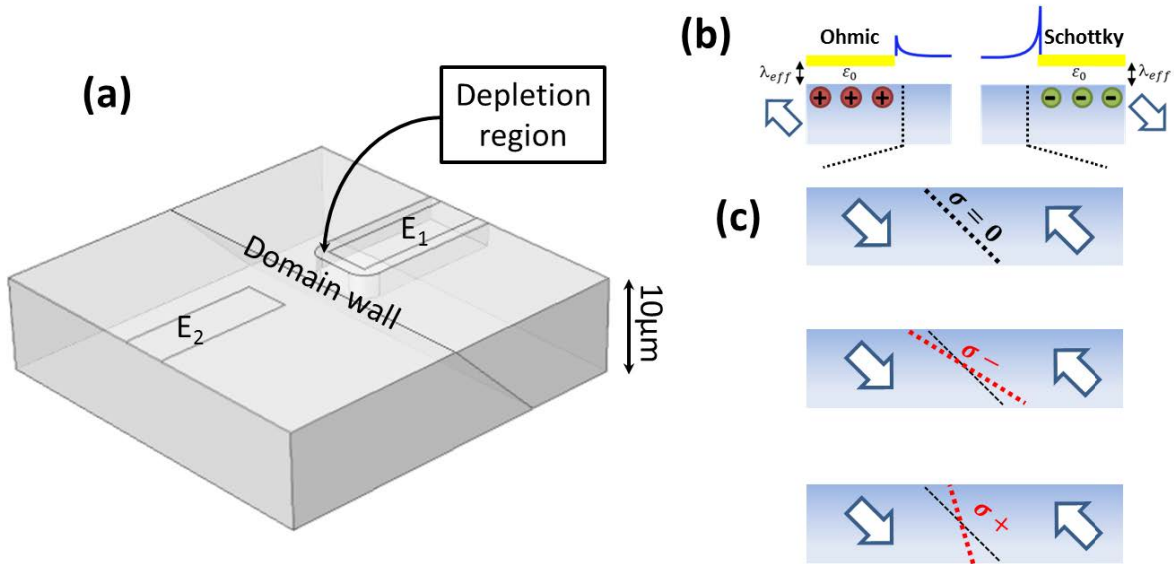

Figure 2.26: Schematics of : (a) The 3D model used for finite element calculations of the internal electric field. (b) A side view of the sample where the main boundary conditions are represented. (c) The domain wall charge depending on the angle between P and the normal to the domain wall.

In the forward regime, the simulation shown on figure 2.27a points out that positive bias induces an electric field which is delocalized in the gap between the electrodes with two maxima close to each interface. Thus it does not match our photocurrent images. Interestingly, this can be fixed by attributing a small negative charges to the domain wall, -0.00022 C/m^2, resulting in a screening of the left part of the domain wall as observed on figure 2.27b.

This domain wall charging is actually to be expected if the domain wall is distorted [70]. This is very likely to happen in our samples as response to the applied voltage, parts of the domain wall remain pinned by some sample defects as illustrated in figure 2.26c. Moreover, depending of the orientation of the bending, the domain wall can be charged by negative or positive charges according to the divergence of the polarization. Since the shape of the photocurrent mapping fits with the x component of the electric fields, E_x can be considered as the main driving force for electron-hole pairs separation. This is a clear evidence of the role played by the internal electric field in the separation of the photogenerated charge carriers.

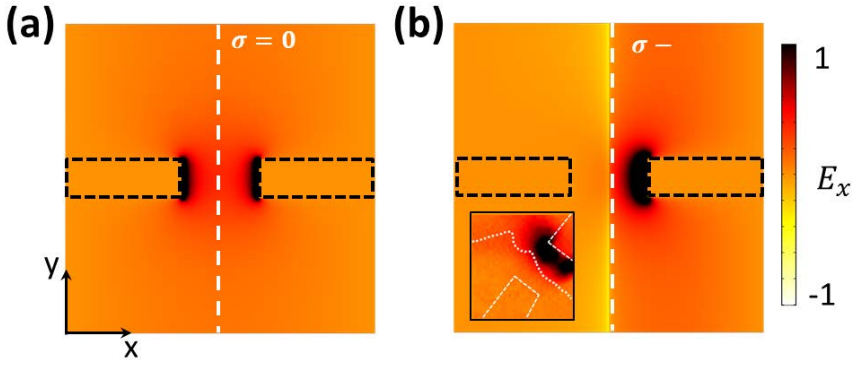

Figure 2.27: (a)(b)Positive bias induces a delocalized electric field along x which is not consistent with the measured images. A small deformation of the DW leads to a negative charge on the DW which reproduces the observations. The x component of the internal electric field reproduces quite well the SPCM measurement shown in insert.

When +25V is applied the domain wall abruptly moves close to E_1 and is now distorted in the other direction, leading to net positive charging (figure 2.26c). With this hypothesis, the simulation map of figure 2.28, with surface charges of +0.00056 C/m^2 on the distorted part of the wall, shows the presence of a strong internal field in the vicinity of the domain wall reproducing quite well the photocurrent mapping. In addition, the change of polarity of the domain wall leads to the inversion of the "photoactive" side of the domain wall. In fact, the left side is now unscreened whereas the right side is screened by the applied electric field. One can also emphasize that the modulation of the measured photocurrent along the domain wall can be perfectly reproduced by the electric field calculation which show three maxima, one at the interface and two at the edges of the distorted domain wall.

Coming back to zero voltage, the photocurrent also comes back to the right part of the domain wall. The depletion region is then extended to the domain wall as the electric field created by the positive charges is in the same direction as that in the depletion region. The distance between the domain wall and the depletion region has to be smaller than the screening length in $BiFeO_3$ to keep its influence on the interface electric field. Consequently, by applying a small negative bias, the domain wall will be slightly displaced to the right and the system comes back to the classical desertion regime with a continuous growth of the depletion region with applied voltage.

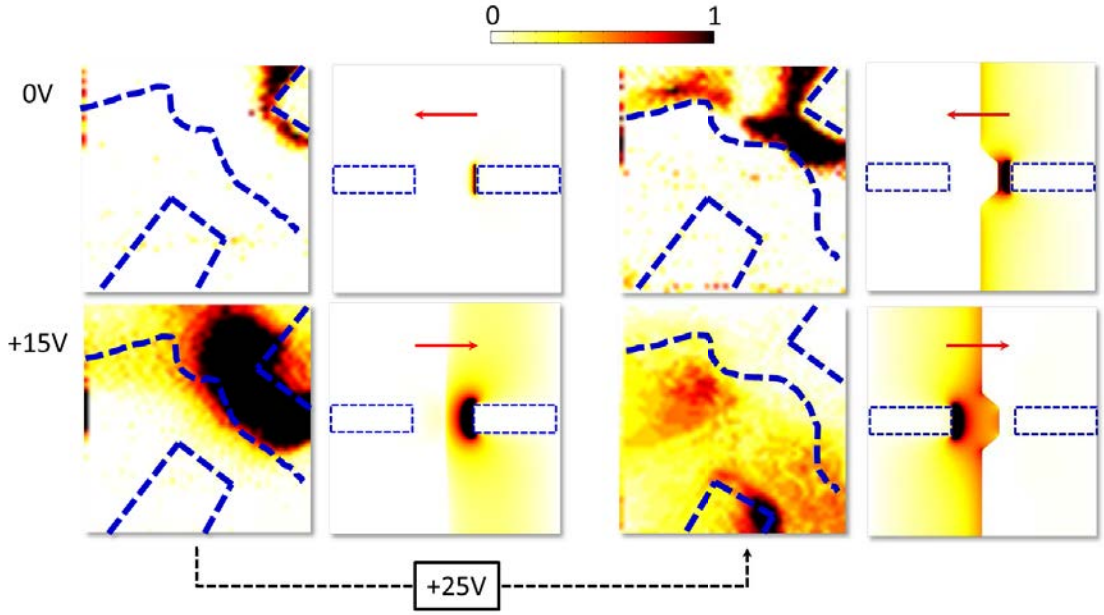

Figure 2.28: Series of photocurrent mapping obtained during a (positive) voltage sweep with associated simulations of the internal field. The domain wall is, at first, as-generated by the nucleation procedure and gets subsequently displaced when applying 25V. When coming back to zero voltage, the configuration is hysteretic. Red arrows indicate the direction of the electrons flow. The color contrast is not in absolute value but it shows clearly that the photocurrent is generated in very different regions depending on the exact position of the domain wall.

Therefore, the overall picture leads to a convincing demonstrating scenario that the photocurrent is closely associated to the presence of a significant internal electric field, generated both by the Schottky contact with the Au electrodes and the bending of the domain wall. The latter effect is responsible for the impressive difference in PV images with the position of the single 180° domain wall. The domain wall is therefore becoming an active entity as it acquires a surface charge controlled by its bending.

2.5.4 Conclusions

To conclude, we have shown that a 180° domain wall can be positioned between two electrodes and reversibly distorted by an electric field. The distortion of the domain wall leads to the apparition of charges which in turn influence the local internal electric field. Our mapping of photovoltaic effects in the vicinity of a single 180° domain wall points to the central importance of the internal field. In line with the physical mechanisms at play in traditional photovoltaic systems, we argue that the presence of an intense

local 'internal' electric field is a central prerequisite for efficient electron-hole separation. The added value of using ferroelectrics lays in the possibility to dynamically change the internal field configuration. In particular, domain walls can be generated and precisely positioned in order to tailor the local photovoltaic efficiency in their vicinity. This opportunity broadens the applicative potential of ferroelectrics for photovoltaics but also for using domain walls as electronically active entities, even though our results show that domain wall themselves do not exhibit specific photoelectric properties.

Chapter 3

Soft X-ray magnetic resonant scattering

The development of magneto-optical x-ray measurement techniques like x-ray magnetic circular dichroism (XMCD) or x-ray resonant magnetic scattering (XRMS) would have been impossible without the availability of high-brilliance synchrotron sources. Originally synchrotron radiation was observed as a parasitic effect in circular particle accelerators dedicated to nuclear and elementary particle physics. Nowadays electron and positron storage rings are built especially for the creation of synchrotron radiation.

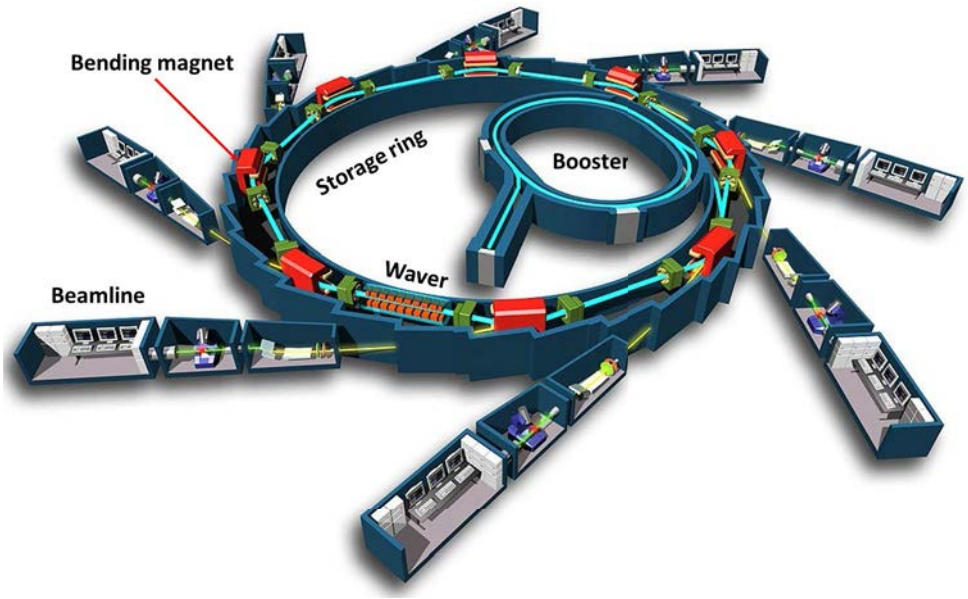

Figure 3.1: Schematic of the SOLEIL synchrotron reproduced from the SOLEIL website.

Electrons are first accelerated in a linear accelerator (LINAC), before being introduced in the booster, where they are circularly accelerated to their final energy, close to the speed of light. A relativistic batch of electrons is introduced in the storage ring where they circulate at a constant velocity through a series of bending magnets separated by straight sections.

As the electrons are deflected in the bending magnets, their acceleration gives rise to an emission of radiation with an energy range from 0.1 to 15 keV. For each magnet, a "searchlight" cone of radiation is emitted tangent to the trajectory and the angular width of the cone is inversely proportional to the Lorentz contraction factor γ . Since $\gamma \sim E$, the energy of the electrons in the storage ring, high energy electrons naturally result in low beam divergences.

Straight sections are formed with insertions devices, such as wavers or wigglers, which are composed with array of regularly spaced magnets. By passing through the insertion device, the electron beam is oscillating and a radiation is emitted for each deflection of the electrons beam. The overlapping of the produced radiations leads to constructive interference for wavelength selected by tuning the periodicity of the magnets array. This results in a monochromatic beam of X-ray with controlled polarization state and an enhancement of the photon flux.

The synchrotron radiation can thus be guided to an experiment "beamline" where it will be used to probe the electronic properties of matter.

In this chapter, I will start by describing the main parts of SEXTANTS beamline and the associated resonant magnetic scattering experimental setup. Located in synchrotron SOLEIL, this soft X-ray beamline performed magnetic scattering experiments on various samples. Then, the exchange magnetic coupling between a soft ferromagnetic layer and $BiFeO_3$ will be investigated and finally I will discuss preliminary work on the magnetization profile through network of multiferroic domain walls.

3.1 A soft X-ray scattering beamline : SEXTANTS

The first part of the beamline is composed of optical elements, such as mirror, monochromator, shutter or slit confined in vacuum chambers. They are used to define the size of the beam, as well as select the energy resolution and clean the parasitic diffusion. Depending on the energy of incident photons, experiments can be done under ambient air in a lead hut for hard X-rays or in a vacuum chamber without other protections for soft X-rays.

SEXTANTS [71] is a soft X-ray beamline which is equipped with an experimental setup from the Néel institute, called RESOX [72] for REsonant SOft X-ray scattering. This setup was developed by Nicolas Jaouen and Jean-Marc Tonnerre and is dedicated to

scattering experiments in the energy range from 50 to 1800 eV with linearly or circularly polarized incident light.

Scattering experiments are performed in $\theta - 2\theta$ configuration where the incident beam is fixed whereas the sample and the detector can rotate to reach a large angular range. Measurements are performed at a fix energy, with a chosen incident polarized light. The angle of measurements is defined by rotating the sample, and the detector measures the intensity scattered by scanning the angle around the specular reflection. The alignment of the optical path in all the parts of the measurements setup is an important step to obtain scattering spectra.

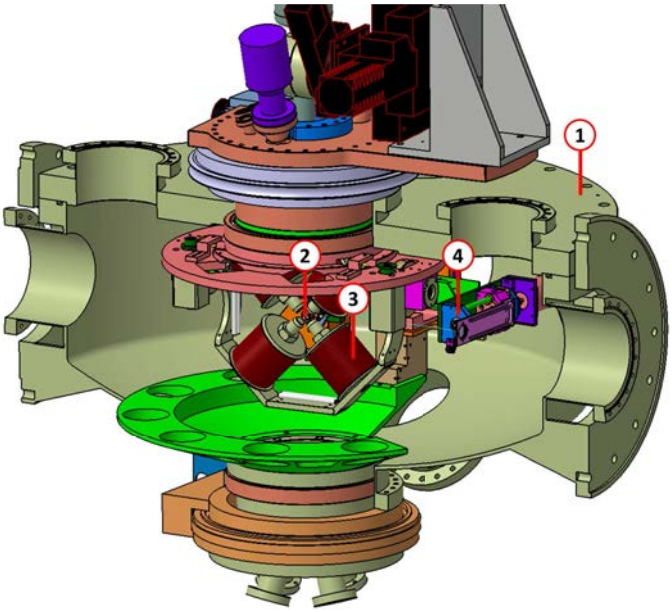

Figure 3.2: Schematic of the setup with : 1- The vacuum chamber. 2- The diffractometer. 3- The magnetic coils. 4- The detectors.

The sample environment is composed of :

1. A vacuum chamber : The soft X-ray are absorbed by air, thus a vacuum of around $10^{-6} mbar$ is needed. Moreover, the vacuum allows to preserve the sample from all sources of contamination.

2. A diffractometer : The diffractometer allows to place the sample in the incident light beam and to find the diffraction conditions by controlling the $\theta - 2\theta$, azymuthal φ and χ angles. The δ angle gives an other degree of freedom to the detector by rotating around the x axis.

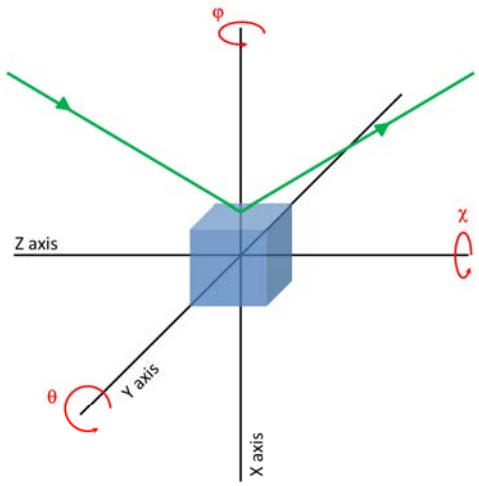

Figure 3.3: Schematic representation of the diffractometer characteristic angles.

3. Magnetic coils : In order to perform magnetic measurements, magnetic coils are placed around the sample and produce an in-plane magnetic field of 0.2T. However the need of large angular range of detection in a limited volume (vacuum chamber) prevents to apply an out-of-plane magnetic field.

4. Detectors : Two types of detectors are available on RESOX, a photodiode which allows 1D measurements and a CCD camera for 2D measurements.

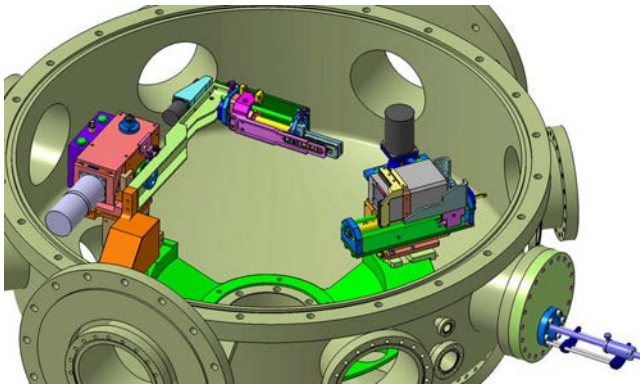

Figure 3.4: Schematic of the detectors in the vacuum chamber. On the left side, the photodiode is holding on an arm with several slits. The CCD camera is on the right side. Both detectors are fixed on a rotating plate which allows to choose one of those detectors without breaking the vacuum in the chamber.

3.2 Exchange magnetic coupling between a soft ferromagnetic layer and $BiFeO_3$

Multiferroic materials allow to control magnetization with an electric field. Since $BiFeO_3$ is antiferromagnetic and ferroelectric at room temperature, it is a good candidate for applications. Unfortunately the absence of net magnetic moment prevents to directly control a magnetization with an applied electric field.

It was previously demonstrated that a 20nm thick ferromagnetic layer of Permalloy ($NiFe$) can be coupled to a $BiFeO_3$ single crystal. These systems were studied by Lebeugle *et al* [73] who showed, by Magneto optical Kerr Effect (MOKE) measurements, that the magnetic moments in the Py layer have an easy axis of magnetization within the sample plane. The direction of the easy axis is not necessarily in the direction which minimizes the depolarizing field. Therefore this unexpected anisotropy was claimed to be caused by the coupling with the underlying cycloidal order of $BiFeO_3$. The local interfacial exchange coupling between the $BiFeO_3$ and the Permalloy layer can be written as :

$$E_{ex} = \frac{1}{2} J_{ex} \mathbf{S_F} \cdot \mathbf{S_C} \tag{3.1}$$

where $\mathbf{S_C}$ is the the local spin canting from the $Fe3+$ moment describing the cycloid and thus would tend to imprint the cycloidal structure on the ferromagnetic layer.

However, since the length scale of the cycloid (64nm) is comparable to the exchange length of the Permalloy (around 15nm), the ferromagnetic layer is not likely to adopt a cycloidal arrangement. Instead they proposed that the coupling should induce a wriggle in the ferromagnetic layer. They estimated an angle of 1.5° for the canting of the ferromagnetic moments in the wriggle. The periodicity of the wriggle is expected to be the same that of the cycloid.

In order to investigate the effect of the long range cycloid on a soft ferromagnetic layer deposited on a $BiFeO_3$ single crystal, we used soft X-ray resonant magnetic scattering (XRMS). The periodic structures are typically of dimensions that perfectly match the soft x-ray wavelength and therefore can be accessed in soft x-ray diffraction in small incidence geometry. The present results are based on a set of such measurements performed at the I06 beamline [74] of the Diamond Light Source and at the Sextants beamline [71] of the SOLEIL synchrotron storage ring using the RASOR [75] and RESOXS [72] diffractometers.

3.2.1 Samples and techniques

We use the $BiFeO_3$ single crystals described in chapter 1, and we deposit 10nm of Co on top of monodomain samples in a Molecular Beam Epitaxy (MBE) chamber. The interface is critical for exchange bias observation then we cleaned the surface with an argon ions beam before deposition of the ferromagnetic layer.

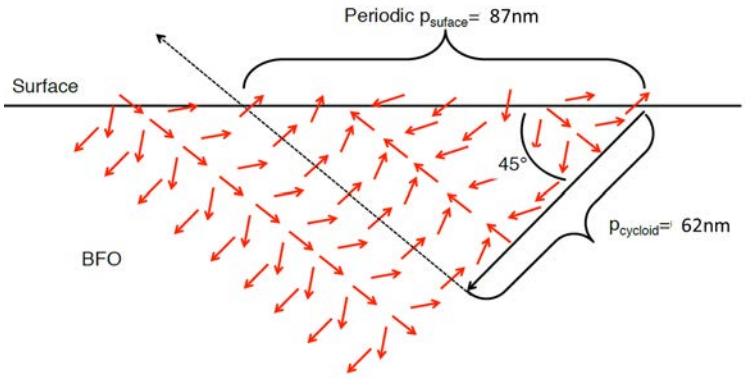

Figure 3.5: A cycloid in the $BiFeO_3$ crystal impinging the [001] surface at 45° makes an interfacial 90 nm periodic structure.

Since the measurement of the coupling between the $BiFeO_3$ single crystal and the Co layer is done at the sample surface, it is important to note that the periodicity of the cycloid is projected on the sample surface as shown in Fig. 3.5. Consequently a cycloid which propagates along the 111 direction gives a wriggle imprint with a 90nm period on the surface.

XRMS is a powerful technique to observe magnetic orders by using the chemical selectivity and the coherent beam of synchrotron radiation. A reflectivity configuration is ideal to probe magnetic depth profiles, but in-plane structures can also be investigated measuring off-specular scattering [76]. Therefore, the imprint of the cycloid in the ferromagnetic layer can be characterized in small incidence geometry by XRMS. Moreover the periodicity of the imprint can be directly compared to that of the cycloid structure by looking at Fe or Co edges.

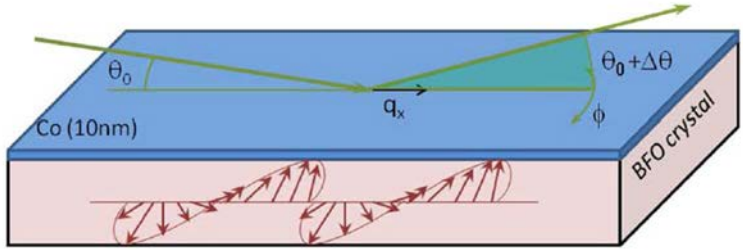

Figure 3.6: Schematics of the scattering geometry used in the soft x-ray experiment. The system is composed of a BFO crystal, an antiferromagnetic compound with long-range cycloids, on top of which a Co layer has been deposited. Measurements of the off-specular scattering allow us to access in-plane magnetic arrangements.

In the scattering configuration shown in figure 3.6, the reciprocal space is scanned in the x direction with :

$$q_x = 2\pi \frac{sin\theta sin\Delta\theta}{\lambda} \tag{3.2}$$

where $q = k' - k$ the probe scattering vector, with k' and k the x components of the wave vector of the incoming and outgoing waves respectively. This is done by controlling the motor displacements of the diffractometer to perform rocking curves by rotating the sample around the specular position with the detector ($\theta - 2\theta$) fixed. We are therefore getting information on the in-plane magnetic modulations with the periodicity $d = 1/q_x$.

In the kinematical approximation, the detected intensity is proportional to the square modulus of the scattering form factor (f), summed over all positions of the magnetic atoms. Considering dipolar processes only and neglecting linear magnetic dichroism, f can be written as follows [77] :

$$f^{res} = F^{(0)}\overrightarrow{e'^{\star}} \cdot \overrightarrow{e} + iF^{(1)}\overrightarrow{u} \cdot (\overrightarrow{e'^{\star}} \times \overrightarrow{e}) + F^{(2)}(\overrightarrow{e'^{\star}} \cdot \overrightarrow{u})(\overrightarrow{e} \cdot \overrightarrow{u}) \tag{3.3}$$

with e and e' the polarization vectors of the incoming and outgoing waves, and u the unit vector along the layer magnetization.

The fist term corresponds to charge scattering while the other two are the first and second order magnetic scattering. The first order in u consists of a polarization dependent geometrical factor multiplying $F^{(1)}$, which is the difference between the resonant

optical response of the medium for opposite magnetization-to-helicity orientations. $F^{(1)}$ is directly related to the observation of x-ray magnetic circular dichroism in absorption spectroscopy. We study here the resonant magnetic signal corresponding to an electric dipole transition between the $2p$ level and the d band of the Fe and Co atoms ($L_{2,3}$ edges), adding a resonant component to the scattering amplitude. In such a process, the spin-orbit interaction in the core-hole state ($2p1/2$, $2p3/2$) and exchange interaction in the d band act respectively as spin-dependent emitter and detector.

The experiments were performed at fixed wavelength in the soft x-ray range between 1.5 and 1.8nm. Looking at the relation for q_x, we can evaluate , the position of the satellite peaks, for a given $\lambda$and θ. Table 3.1 presents the $\Delta\theta$ values for an incoming photon of 774eV :

2θ	10°	12°	14°	18°	22°	28°
p=64nm	8.24	6.87	5.88	4.85	3.75	2.96
p=90nm	5.85	4.87	4.18	3.25	2.67	2.1

Table 3.1: Calculated values for $\Delta\theta$ at E=774eV

For small angles up to $2\theta = 10°$, due to the difference between the position of the satellite peaks, it is not possible to observe both periodicities with the same angular configuration. For higher angles than $2\theta = 28°$, the satellite peaks are too close to the specular peak and it may even not be possible to see them. During the experiments the best compromise was found for 2θ around 13°.

The penetration depth of soft-rays at the L edge of $3d$ metals is around 74nm and around 486nm far from the resonance. Since the Co layer is 10nm thick, the beam will go through and reach the $BiFeO_3$ single crystal at the Fe edge. However, the signal from the Co layer is expected to be small because of the slight canting of the Co spins (1.5°) and the low thickness with, thus, less Co atoms contribution. On the contrary the signal of the Fe atoms should be stronger (more atoms and bigger contribution), but since it has to cross the Co layer, the intensity is considerately decreased. Consequently, the beam has to be very bright to observe XRMS in both layer.

3.2.2 Results and discussion

The reflectivity spectra at the Fe and Co $L3$ edges are shown in figure 3.7 where satellites are visible on both sides of the specular reflection when at resonance. Those found at the Fe edge are expected signatures of the cycloidal antiferromagnetic arrangements at the $BiFeO_3$ surface. At the Co edge, similar humps can also be seen. These structures unveil the existence of periodic magnetic arrangements in the thin Co layer as well. The satellites associated to the wriggle in the Co layer appear less intense than at

the Fe edge. In fact, one might also expect the exchange coupling to decrease as it is stronger at the interface than at the top of theCo layer. The diffraction resulting from the average signal over the entire layer is thus attenuated. This is the central result as it directly demonstrates that the $BiFeO_3$ cycloids imprint a long-range modulation into the adjacent ferromagnetic Co layer.

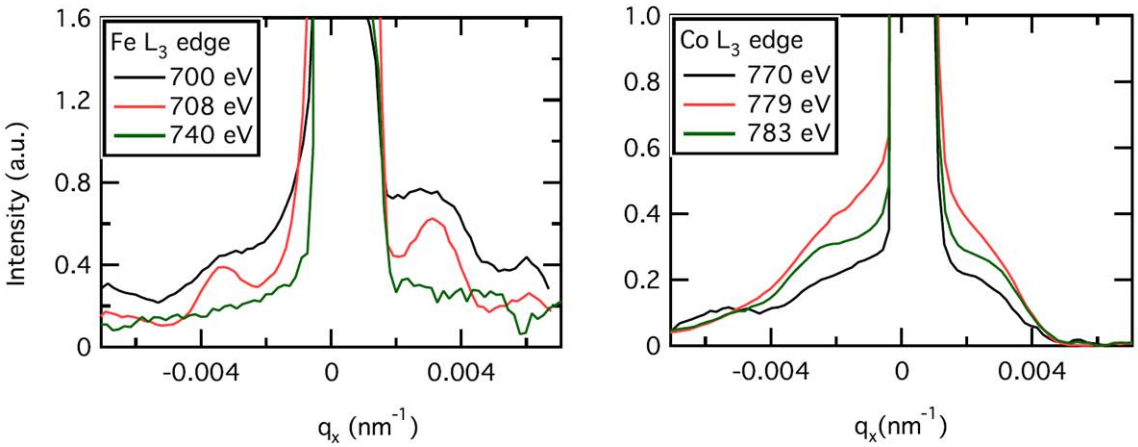

Figure 3.7: Energy dependence of the scattering spectrum around the Fe and Co edges showing the appearance of side peaks at resonance.

Antiferromagnetic cycloids in our single domain $BiFeO_3$ crystals have three symmetry-allowed propagation vectors, $\tau_1[1\bar{1}0]$, $\tau_2[10\bar{1}]$, and $\tau_3[0\bar{1}1]$, with antiferromagnetic moments rotating in the planes defined by the propagation vectors and the polarization [111] direction [38]. All cycloids have a 64 nm period, but the (001) surface of our crystal cuts cycloids τ_2 and τ_3 at 45°, thus resulting in a 90 nm periodic surface structure as shown in figure 3.5. On the other hand, cycloid τ_1 which is parallel to the surface plane simply yields to a 64-nm-periodic footprint. However, the measured period in figure 3.7 is around 120 nm, much larger than those expected at the surface. This can be accounted for by considering the azimuthal angle of the incident and reflected beams, which do not lay along the surface cycloidal propagation directions. Indeed, the apparent periodicity can be written as :

$$p = p_0/cos(\varphi) \tag{3.4}$$

where p is the cycloid pitch in the $BiFeO_3$ surface plane.

The presence of several humps in the data indicate that the x-rays are diffracted by several cycloids with propagation vectors in different directions.

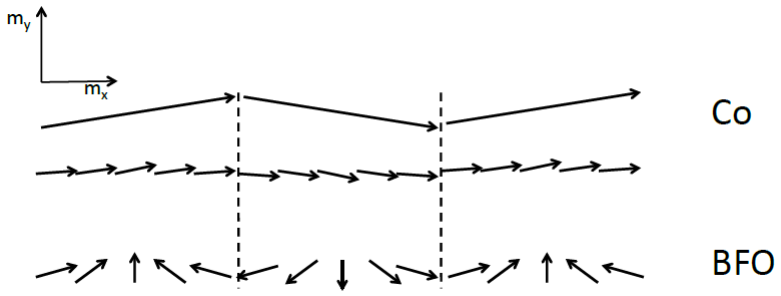

Figure 3.8: Schematic representation of spin cycloidal orientation in $BiFeO_3$ and the imprint wriggle in the Co layer which can be modeled by two sinusoidal waves in the x direction.

The Co layer has its magnetic moments coupled with those of the $BiFeO_3$ cycloid, resulting in a wriggle at the Co surface. The contribution can be thus decomposed in two components as shown in figure 3.8 which can be modeled by two sinusoidal functions. We can write the magnetization in the xy plane as two sinusoidal waves propagating in the x direction :

$$m_x = m_{x_0} cos(\tau x) \tag{3.5}$$

$$m_y = m_{y_0} sin(\tau x) \tag{3.6}$$

where $\tau = 1/p$.

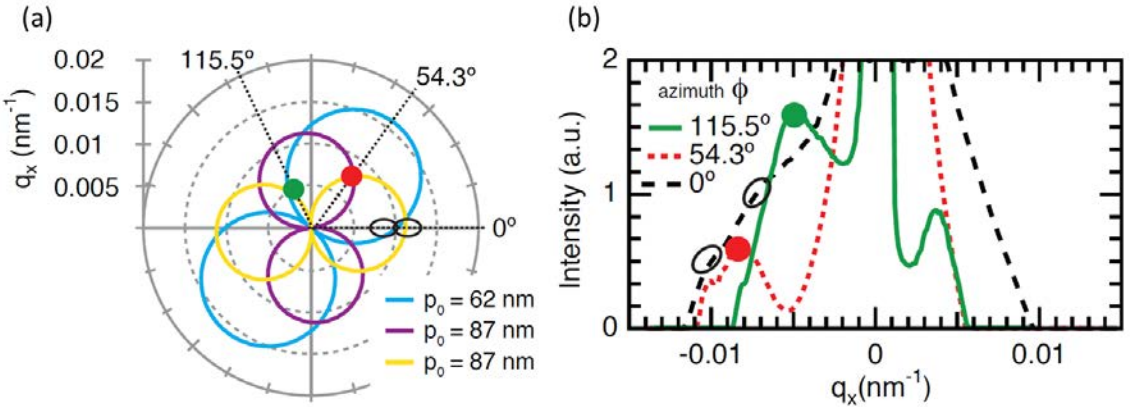

Figure 3.9: (a) Polar simulation of the satellite positions as a function of the azimuthal angle fitting very well zigzag modulations with a period of 62 nm (the dot size represents the error bars). (b) Experimental data at the Co edge for three azimuthal angles.

Figure 3.9a presents the results of our simulations in a polar graph representing the expected position of the off specular satellite peaks in reciprocal space as a function of the azimuthal angle. Figure 3.9b shows three sets of data taken at the Co edge at different azimuthal angles. The data points (color dots) fit very well on the modeled lines, which evidence the presence of at least two different zigzags at different positions in the sample. Indeed, for each azimuthal angle of figure 3.9 a different region is probed by the x-ray beam. Black hollow circles determined from the dashed black scattering curve belong to two different cycloids (blue and yellow). The attribution of the red and green circles is not univalent: while both could belong to the same yellow cycloid, they could also pertain the former to the purple cycloid and the latter to the blue one. It therefore appears that at least two of the three symmetry allowed cycloids in a single ferroelectric domain are present in our sample. This is in agreement with the recently reported multicycloidal domains in single ferroelectric $BiFeO_3$ crystals [78], but not to the previous neutron measurements which evidenced only one cycloid in a $BiFeO_3$ single crystal.

The present results directly demonstrate that the cycloids go all the way to the $BiFeO_3$ surface. The magnetic origin of the Co peaks is confirmed by their disappearance off-resonance and by their temperature dependence, as shown in figure 3.10a where the peak intensity at the Co $L3$ edge vanishes when approaching the Néel point of $BiFeO_3$, in close resemblance to the intensity of the $BiFeO_3$ antiferromagnetic peaks measured with neutrons [79].

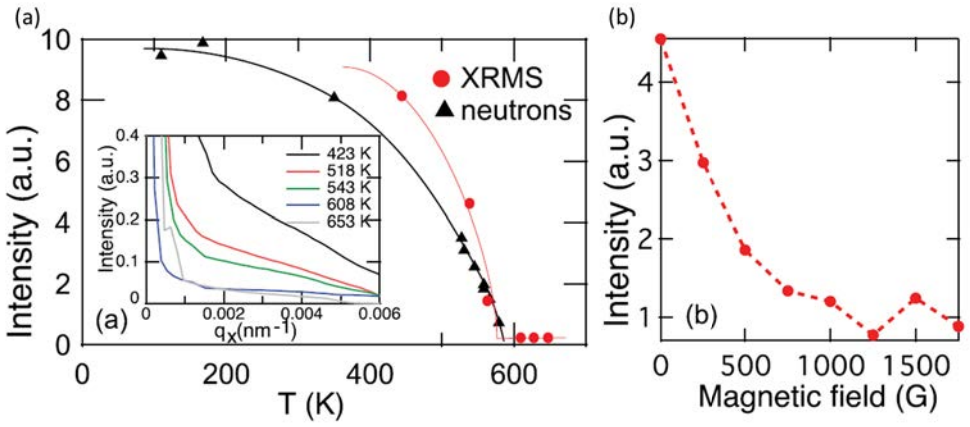

Figure 3.10: (a) Temperature dependence of the structures at the Co edge. The peaks disappear concomitantly with those at the Fe edge as the temperature is raised to the Néel point of $BiFeO_3$. Our data are compared to neutron scattering measurements of the antiferromagnetic peak of $BiFeO_3$ [79]. (b) Field dependence of the Bragg peak at the Co edge at room temperature.

To unambiguously demonstrate the magnetic origin of the Bragg peaks measured at the Co edge, a magnetic field was applied in RESOXS diffractometer within two different directions in the plane of the sample surface. We report the suppression of these peaks when applying a small field of only 1500 G, meaning that the wriggle vanishes as shown on figure 3.10b. This applied field is not strong enough to modify the cycloids in $BiFeO_3$ but enough to dominate the interfacial exchange coupling at the interface. This further evidences that the ordering of the Co magnetization is driven by the presence of cycloids in $BiFeO_3$. It is difficult, from our measurements alone, to provide a complete picture of the Co magnetic structure, beside its period. Magneto-optical measurements show an in-plane globally saturated Co magnetization, suggesting that the cycloid imprints manifest themselves as very small wriggles of the Co moments.

It is possible to model the influence of the $BiFeO_3$ structure in the Co using known parameters. Let us consider a rigid interface magnetization in $BiFeO_3$ consisting of parallel linear chains oriented along the x axis with a magnetization following a cycloid. The ferromagnetic overlayer is assumed magnetized in-plane. The total Hamiltonian can be written in the form of three terms representing the exchange and Zeeman energies along with an interface coupling interaction (anisotropy can be neglected) :

$$H = -J_{FM} \sum_{l=1}^{N} \sum_{R} (\sum_{\eta} cos[\theta_l(R) - \theta_l(R+\eta)] + cos[\theta_l(R) - \theta_{l+1}(R)] - \mu_B g H_0 \sum_{l=1}^{N} \sum_{R} cos[\theta_l(R) - \varphi_0] - J_0 \sum_{R} cos[\theta_1(R) - \varphi_0(R)]$$

where the atomic planes are indexed l, starting from 0 at the $BiFeO_3$ interface and increasing going into the Co layer, the vector R specifies a lattice site on the lth plane, and η is a nearest-neighbor lattice vector in this plane. The external field H_0 is oriented in-plane and J_0 is the exchange interaction that couples Co and Fe atoms across the $Co/BiFeO_3$ interface, while J_{FM} is the exchange interaction in the ferromagnet, the magnitude of the spin being normalized to $1.\theta_l(R)$ is the spin angle at site R in the lth layer, φ_0 is the field angle, and $\varphi_0(R)$ is the canting angle at site R on the $l = 0$ Fe layer.

Minimizing the energy with respect to the angle $\theta(r)$ at site r and introducing the canting angle relative to the field direction [80] leads to an arrangement forming a zigzag following the cycloids and decaying along the direction normal to the $BiFeO_3/Co$ interface.

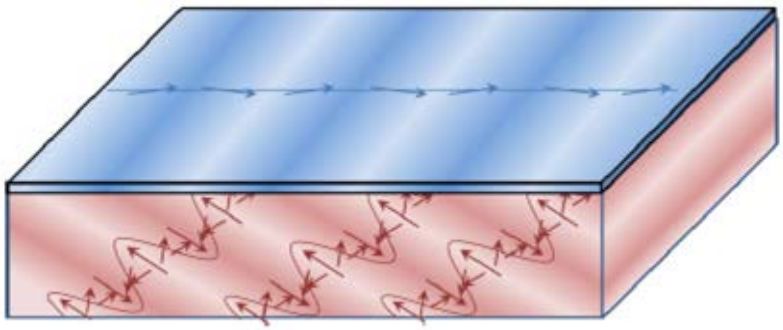

Figure 3.11: Imprinted cycloidal arrangement of the BiFeO3 crystal into a wriggle in the Co layer.

The in-plane magnetic order can also be schematized as zigzags with the same period as the surface cut of the $BiFeO_3$ cycloid as depicted on figure 3.11. As in the case of spin waves, it appears that the system's energy is minimized when the Co magnetization is parallel to the wriggle propagation vector. For an average 1° angle, consistent with the above calculation, an anisotropy around 100 Oe can be expected, close to that measured experimentally [73]. We underline here that this is conceptually quite different from exchange bias, which is generally attributed to uncompensated spins at the interface and controlled by a field-cooling procedure. In the present case, the induced anisotropy is solely controlled by the antiferromagnetic cycloids which can be toggled by changing the electrical polarization.

3.2.3 Conclusions

In conclusion, we provide a direct experimental evidence that long-range antiferromagnetic structures can be imprinted on soft ferromagnets through interface magnetic exchange. Using soft x-ray magnetic scattering reflectivity we measure the magnetic modulation in a cobalt layer deposited on multiferroic $BiFeO_3$ crystals containing antiferromagnetic cycloids. The observed magnetic wriggles are understood using a simple interfacial exchange coupling model. The propagation vectors of these structures define the anisotropy axis known to exist in soft ferromagnets deposited on $BiFeO_3$ single crystals. We underline here that the magnetic layer could thus also be used to reveal antiferromagnetic long-range structures providing that the ferromagnet can be imaged or probed, which is usually easier than magnetic imaging in antiferromagnets.

Unfortunately, the measurement of the Co layer magnetization under an applied electric field was not successful. In fact the relative orientation of the ferroelectric polarization in our $BiFeO_3$single crystal with respect to the applied electric field in a capacitor

configuration, prevents to homogeneously return the polarization. The sample becomes multidomain with a 001 domain pattern which results in twin surface. Consequently, no information from the satellite peaks could be obtained whereas we observed a splitting of the specular peak as can be seen on figure 3.12. This specular splitting originates from the multiple reflection on the twin surface.

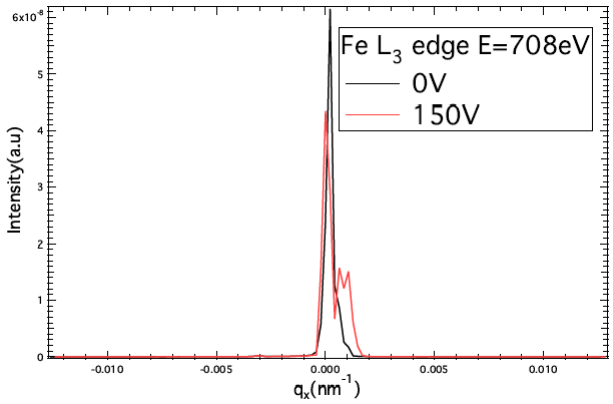

Figure 3.12: XRMS spectra at the Fe edge before and after applying an electric field. The specular splitting results of the multiple reflection on the twin surface created by the non homogeneous ferroelectric reversal.

The control of magnetization in the ferromagnetic layer is still to be demonstrated, by improving the control of the ferroelectric polarization reversal by using a unique sample presenting two regions with different in plane ferroelectric polarization, where one can expect to see a difference between the wriggle orientation.

3.3 Magnetization profile through a network of multiferroic domain walls in $BiFeO_3$

Because of the magnetoelectric interaction, each border between two polarization domains also corresponds to a magnetic wall. Privatska and Janovec [4] reported that magnetoelectric coupling could lead to the appearance of a net magnetization in the middle of antiferromagnetic domain walls. Specifically, they showed that this effect is allowed for $R3c$ space groups, which is the symmetry of $BiFeO_3$, but their group-symmetry arguments do not allow any quantitative estimate. Daraktchiev et al. [36] have proposed a thermodynamic (Landau- type) model with the aim of quantitatively estimating whether the walls of $BiFeO_3$ can be magnetic and, if so, to what extent they might contribute to the observed enhancement of magnetization in ultrathin films.

Their conclusion is that it is possible for a net magnetization to appear in the middle of ferroelectric walls even when the domains themselves are not ferromagnetic. This is, however, just a "toy model" which does not take into account the exact symmetry of $BiFeO_3$, so it cannot yet quantitatively estimate how much domain walls can contribute to the total magnetization. The exact theory of magnetoelectric coupling at the domain walls of $BiFeO_3$ remains to be formulated.

The present study aims at measuring the magnetic moment associated to 71° domain walls in $BiFeO_3$ thin films with as grown stripe domain patterns. The samples are elaborated in the UMR CNRS/Thales by Pulsed Laser Deposition on $DyScO_3$ substrates. The dichroic magnetic signal recorded in scattering conditions at the Fe $L_{2,3}$ edges will measure the uncompensated magnetization of the domain walls. The selection of the reciprocal space position corresponding to the domain walls periodicity ensures to probe the moment of ONLY the domain walls. It is important to note here that the period of electrical polarization is usually twice that of the domain walls. This allows to select the right diffraction spot for the magnetic analysis. The magnetic moment inside the walls could then be studied as a function of external parameters like magnetic field and temperature (20-320K) available at the RESOXS soft x-ray diffractometer [72]. Periods in the 50 to 200nm range are well suited to the capabilities of the instrument. The measurement will then give quantities like the average amplitude of the uncompensated magnetic moment at the domain walls and the collective spatial arrangement of these domain walls.

3.3.1 Samples and techniques

Since $BiFeO_3$ belongs to the $R3c$ space group, the polarization can point along one of the four 111 directions, giving rise to eight possible domain variants. Following the choice of substrate type, orientation, and/or vicinality, one can tailor the morphology and type of ferroelectric and/or ferroelastic domains in epitaxial $BiFeO_3$ films. In fact, the strategy to control the domain pattern is to restrict the growth of possible domain variants at the initial nucleation stage. With a four fold symmetry substrate, as (001) $SrTiO_3$, there is no restriction on the domain formation, resulting in equal probability of formation for all domain variants.

Figure 3.13: Domain engineering using miscut STO substrates (with SRO bottom electrode). With no miscut (left) the BFO grows with four polarization variants; with miscut along [100] (middle), two variants are obtained; and finally with a miscut along [110] (right), only one polarization variant is formed. Reproduced from ref [12]

By using substrates with miscuts [12], one can artificially break the original four-fold

symmetry and along particular high-symmetry crystallographic directions, the eight polarization variants of $BiFeO_3$ can be reduced to four, two, or just one polarization variant as illustrated on figure 3.13. This is due to two important parameters :

- The miscut direction reduces the number of possible domains through the structural relationship between the rhombohedral distortion of BiFeO3 and the step edge of the miscut substrate

- The miscut angle, the angle between the crystallographic plane and the physical surface of the substrate, prevents 2D nucleation on the terraces and the formation of multiple domains.

In addition, misfits introduced by using anisotropic substrates such as $DyScO_3$ can be used to tune the strain in the $BiFeO_3$ epitaxial layer. As a result, one can control the magnetic properties of the films as shown in figure 3.14.

Figure 3.14: Free energy of the system relative to a pseudo-collinear order, showing the stability regions for a number of cycloidal orders. Blue regions correspond to pseudo-collinear order; pink region to the bulk-like cycloid, and the yellow region to a new type-2 cycloid. Reproduced from ref [81]

In order to study the magnetic profile of $BiFeO_3$ domain walls, we used $BiFeO_3$ thin films with as grown stripe domains. The samples were elaborated in the UMR CNRS/Thales by Pulsed Laser Deposition on $DyScO_3$ substrates. The atomic force microscopy (AFM) image (figure3.15a) on the substrate surface shows periodic steps with a 150nm period. After deposition, in plane PFM image (figure3.15b) shows a well arranged stripe domain pattern, whereas the out of plane image (figure3.15c) shows no variation which indicates that the film is only composed of 71° domains with in plane variants. Note that the $BiFeO_3$ domains themselves are strictly non-magnetic as the antiferromagnetic cycloids are not destabilized by the strain state induced by the $DyScO_3$ substrate [81] (figure 3.14).

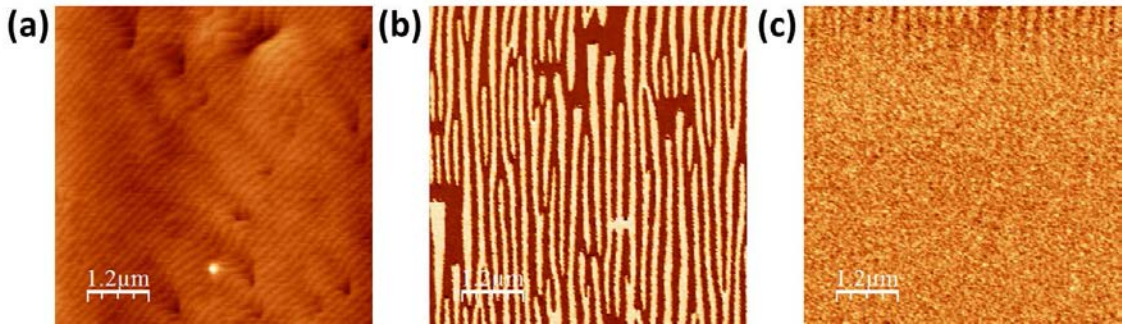

Figure 3.15: (a) AFM image of the $DyScO_3$ substrate surface shows periodic steps with a 150nm period. (b) In plane PFM image shows a well arranged stripe domain pattern. (c) Out of plane PFM image shows no variation which indicates that the film is only composed of 71° domains with in plane variants.

Soft x-ray resonant magnetic scattering was carried out at the SEXTANTS beamline at SOLEIL.

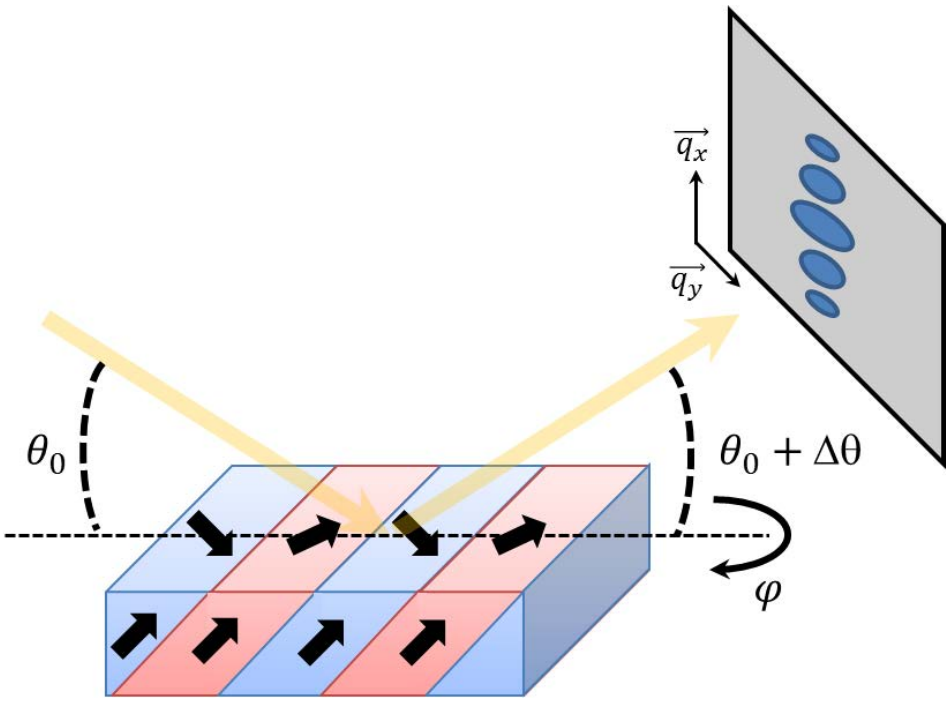

Figure 3.16: Schematics of the scattering geometry used in the soft X-ray experiment. The system is composed of a 25nm thick $BiFeO_3$ thin film with stripe domains. The ferroelectric polarization is 90° rotated in the surface plane between neighbor domains.

In the scattering configuration shown in figure 3.16, thanks to a 2D CCD camera, the

reciprocal space is directly imaged along two directions :

$$q_x = \frac{2\pi}{\lambda} sin\theta sin\Delta\theta \tag{3.7}$$

$$q_y = \frac{2\pi}{\lambda} sin\Delta\theta \tag{3.8}$$

Similarly to what has been done in the previous part of this chapter, we study the resonant magnetic signal corresponding to an electric dipole transition between the $2p$ level and the d band of the Fe atoms ($L_{2,3}$ edges), adding a resonant component to the scattering amplitude. Consequently, we expect to see diffraction peaks for all the order parameters in the sample coming from resonant magnetic scattering superimposed on a charge scattering response. First, the largest part of the scattered amplitude is coming from the charge scattering term. The response can be calculated with a simple charge density model where the scattered amplitude $f(\overrightarrow{q})$ is given by the Fourier transfom of the charge density $\rho(r)$:

$$f(\overrightarrow{q}) = \int \rho(r) e^{i\overrightarrow{q}.\overrightarrow{r}} d^3r \tag{3.9}$$

The average charge densities in the substrate and in the film remain homogeneous but the broken spatial symmetry induced by the surface steps and the alternate polarization domains should lead to resonant scattering. Therefore, one needs to find the periodicity of the substrate surface steps and the ferroelectric domains of the film.

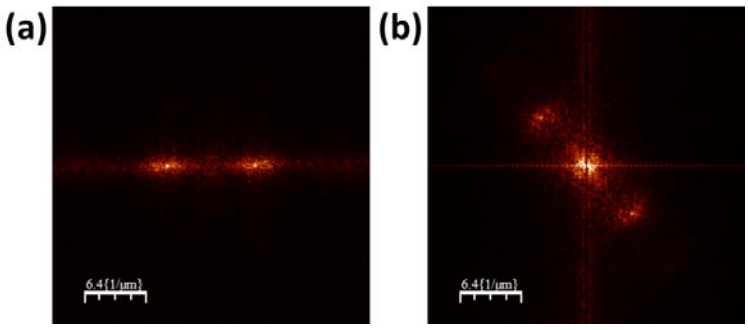

Figure 3.17: Fourrier transform of (a) the AFM image of the sample surface (3.15a), (b) the in-plane PFM of the $BiFeO3$ thin film (figure3.15b)

A simple fourier transforms of the AFM image of the substrate and the in-plane PFM image of the film can give a good approximation of what is expected as a scattering response. Resulting images are shown in figure 3.15 and show two distinct series of aligned peaks which are rotated by 48.6° with respect to each other. Each period can be determined by measuring the distance in the reciprocal space of each peak from the central peak. The extracted period of the surface steps is $\sqrt{2}$ times larger because of the tilt of the pattern.

3.3.2 Results and discussion

Diffraction pattern for different φ angles are shown on figure 3.18 recorded at 707 eV.

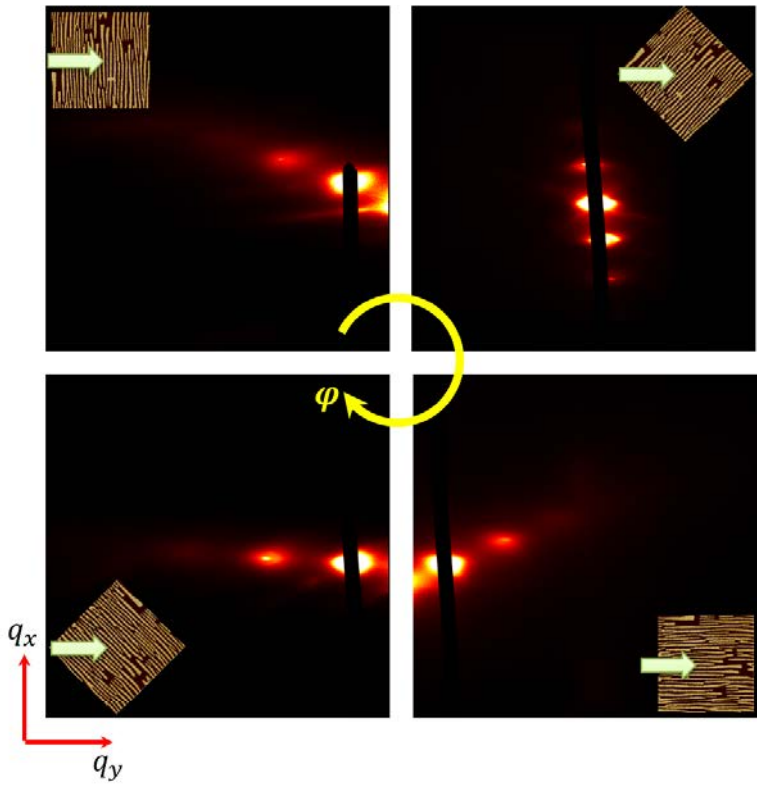

Figure 3.18: Diffraction images of stripe domain $BiFeO_3$ thin film. The diffraction pattern rotates with the azimuthal angle (φ) and its period is found to be similar to that of the surface steps (157nm). The direction of the incident beam with respect to the ferroelectric domains is indicated in corresponding image corner.

Intense equidistant peaks are aligned in a direction that rotates with the relative orientation of the incident beam with respect to the sample. The rotation axis is centered on

the specular peak in the middle of the diffraction pattern. The relative angle between the incident beam (30° from the sample surface) and the periodicity of the diffracted pattern does not match with the ferroelectric domain pattern. In addition, the absence of linear dichroism rules out the diffraction on the ferroelectric domains. Instead, it seems to be coherent with these steps as the peaks follows the azimuthal angle and the periodicity associated to the diffraction of the surface steps. One can see structural peaks up to the third order spanning intensities of 5 orders of magnitude.

In order to, better image the higher orders, the specular peak is put out of the camera and the first order peak is hidden by a beamstop.

The difference of two images record respectively with incoming left and right circular polarization that is display in figure 3.19 will be called 'XMCD' image in the following. We thus observe on these 'XMCD' images, an other series of peaks whereas the predefined structural peaks almost disappear. This series of peaks is not centered on the main specular peak but is shifted and have a different orientation and periodicity. This series of peaks is aligned in the direction of the stripe periodicity and rotate with the sample around the main specular peak. It can also be seen on figure 3.19c that this structure is symmetric with respect to the main specular peak. One can only partially see the symmetric structure but this demonstrates that it is indeed there and that the circular dichroism signal is reversed (black spot). This is typical of the diffraction of chiral magnetic structures. The distance between two peaks follows the Bragg's law variation relative to the azimuthal angle and thus can be associated to the diffraction pattern of a magnetic structure periodic in this direction .

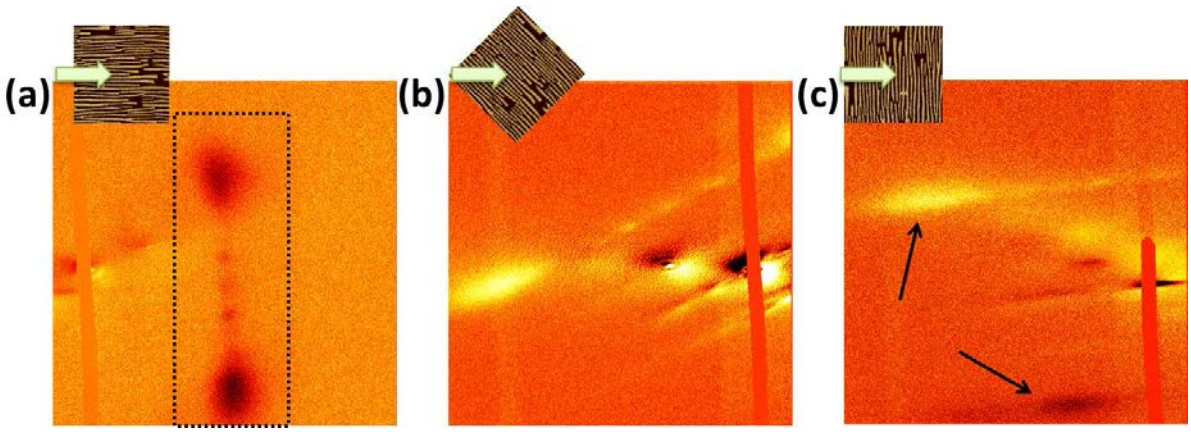

Figure 3.19: XMCD images of the diffraction pattern which reveal an other series of peaks. They rotate with the azymuthal angle. Black arrows indicate the two symmetric series of peaks with respect to the main specular peak (hidden on these images).

In order to characterize the magnetic properties of this pattern, we thus focus on this

second series of peaks. The 'XMCD' images at the iron edge, out of resonance and at the oxygen edge are shown in figure 3.20. At the Fe edge, the series of peaks can originate from magnetism and ferroelectricity as the Fe ions are part of the two ferroic orders. Out of resonance, the absence of these peaks points out that the periodicity is carried by the Fe ions. Finally, the absence of peaks at the O edge rules out ferroelectricity as the oxygen ions are much less influenced by the magnetic order than by the ferroelectric order. We therefore conclude that diffracted pattern comes from a magnetic chiral structure, i.e. a cycloidal arrangement.

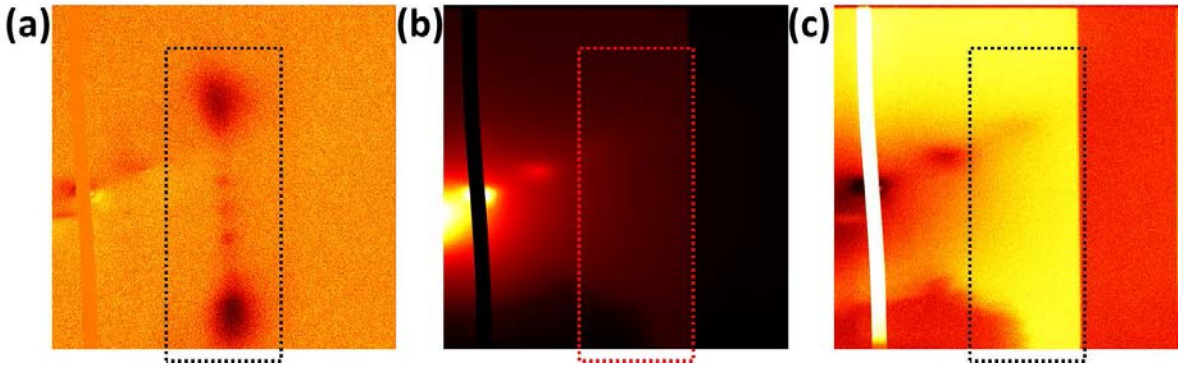

Figure 3.20: Images of the diffraction pattern (dash rectangle) associated to the magnetic structure, (a) at the Fe edge, (b) out of resonance, (c) at the O edge.

The second order structural peak was also shifted in order to obtain a much better resolution of the diffraction pattern. The resulting 'XMCD' image is shown on figure 3.21 and thanks to the previous operation, line profile along the structure gives now three peaks related to magnetic dichroism. We summarized the diffraction pattern on figure 3.21 where three periods can be extracted. The largest peaks give a periodicity around 53nm and the smallest, around 210nm. Between this two peaks, a smaller one gives a period around 110nm.

As discussed in the previous part of this chapter, the presence of a cycloid in a sample can lead to a diffraction pattern which reveals the projection of the cycloidal period on the surface. As the cycloid rotates in the plane formed by the polarization and the direction of propagation, this plane toggles from one ferroelectric domain to the other. Moreover, for each toggle, a domain wall is predicted to have a small magnetic moment.

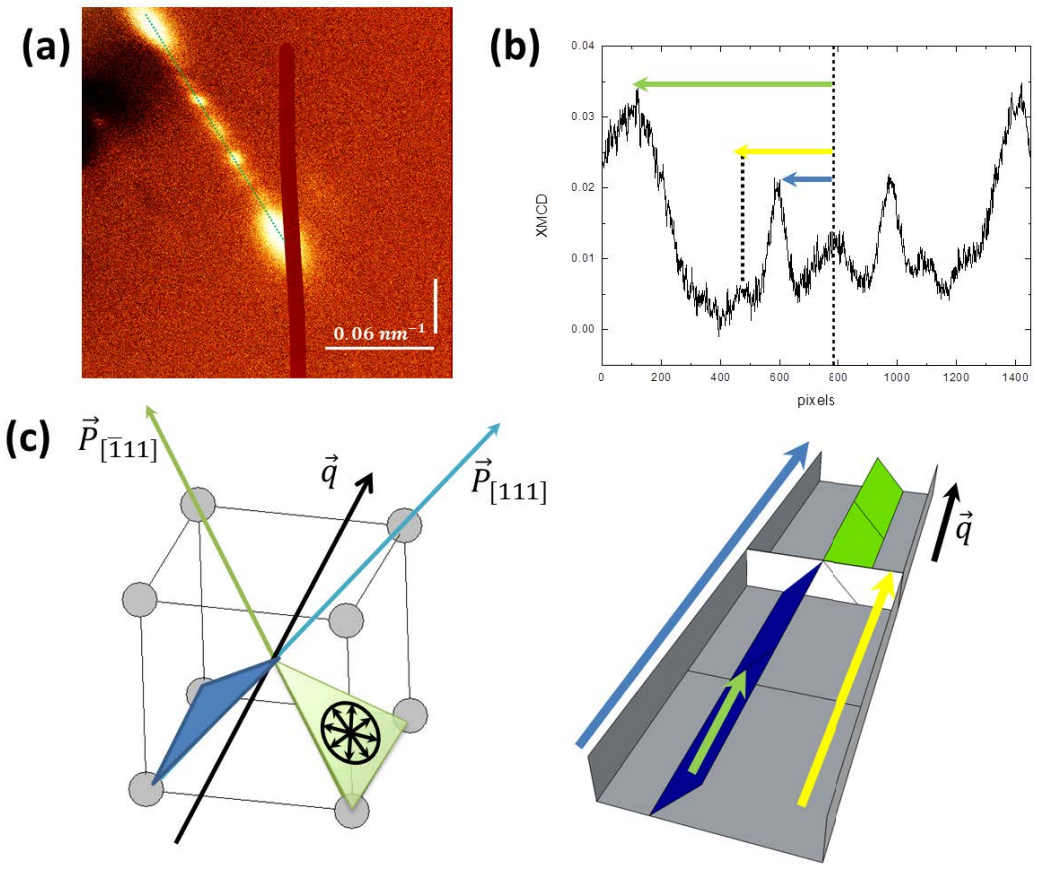

Figure 3.21: (a) 'XMCD' images of the magnetic structure (the black line is the beam stop which was unfortunately positioned there). (b) Line profile of the green dash line. (c) Schematics of the domain structure which leads to the observed diffraction pattern. Cycloids rotate in a plane which toggle with the periodicity of the ferroelectric domains but the propagation vector remains in the same direction. The green arrow gives a period associated to the cycloid. The yellow arrow gives a period associated to domain walls. The blue arrow gives a period associated to the cycloid toggling.

This magnetic structure can then lead to three order parameters :

- The 53nm period is associated to the projected cycloid.

  This value is smaller to that in the bulk (90nm), but compressive strain induced by epitaxial misfits, could influence its period which has never been measured so far. The corresponding structure is found perpendicular to the stripes, along [110], and corresponds to one of the allowed cycloidal directions for both types of domains.

- The 108nm period is associated to the domain walls. The peak is thus related to a possible magnetic contribution in the domain walls.

  This value is half the domain periodicity given by PFM measurements.

- The 210nm period is associated to the toggling of the cycloid plane between each ferroelectric domain as well as the second order of the magnetic contribution of the domain walls, which should be very small.

  This value is close to the domain periodicity (240nm) given by the PFM measurements.

In addition, the observation of a symmetric series of peaks with respect to the main specular peak indicates that the overall observations are also modulated by another periodic structure which is parallel to the stripe with an approximate 50nm period. This structure could also be a cycloidal domain pattern, also allowed in this direction.

3.3.3 Conclusions and outlooks

In conclusion, we imaged the surface diffraction pattern of a cycloidal order modulated by stripe domains with alternate in plane ferroelectric polarization. This observation confirms that the cycloid is "printed" on the surface of the sample and is able to induce a periodic structure which can be seen by circular dichroism. Moreover the alternating ferroelectric polarization in each domain leads to a modulation of the cycloidal order which also gives rise to diffraction peaks. Indeed, the propagation vector remains the same in both populations of domains but the cycloidal plane toggles between the (112) and $(1\bar{1}2)$ variants.

A signal arising from the domain walls was also measured and could be associated to a net magnetic moment as it appears only by circular dichroism. However, the dichroic signal is too small to lead to a reliable quantitative estimate.

Moreover, the diffraction pattern also indicates that there may be a periodic structure in the direction parallel to the stripes. This could be consistent with the establishment of other superimposed modulation running parallel to the stripes which could result in a chessboard pattern. This is also consistent with micromagnetic simulations presented in chapter 5.

Nevertheless, the goal of these measurements was to measure the magnetization profile associated to the antiferromagnetic domain wall. We could not manage to observe the diffraction pattern associated to the ferroelectric domains nor to the domain walls. We emphasize here that we are not measuring the diffraction of the ferroelectric domains. Indeed, in order to minimize the elastic energy in striped samples, the 71° domain walls are parallel to the [101] direction, resulting in planes tilted in the sample thickness.

Consequently, the periodic structure forms a 54° angle with the surface, leading to a real θ angle of 35°. Thus, the sample would have to be tilted in order to locate the 1D structure diffraction spot in the detector. This geometry shall be attempted in the months to come.

It is important to note that the measurements presented here are still ongoing and this chapter can still be considered as preliminary work.

Chapter 4

High magnetic field control of the spin cycloid in multiferroic $BiFeO_3$

Bismuth ferrite $BiFeO_3$ is by far the most studied magnetoelectric multiferroic material, on account of having both the ferroelectric and magnetic ordering temperatures well above room temperature [7]. This, combined with very large polarization [10, 11] and coupling between electric and magnetic orders [8, 9] have made this material the most promising candidate for magnetoelectric spintronic devices [17], leading to a very intense research effort devoted to this material.

The DM interaction has been recently revisited and reformulated in the light of spin currents and electric fields. It has thus been shown that electron hopping between magnetically canted magnetic ions through oxygen atoms induces a small electric field perpendicular to the hopping direction : $\mathbf{P_s} \propto \mathbf{e_{ij}} \times (\mathbf{S_i} \times \mathbf{S_j})$ with e_{ij} the vector linking the cation neighbors along the cycloid direction and S_i and S_j their magnetization vectors [26]. Interestingly the polarization induced by the cycloid can be singled out in high magnetic field measurements as the long range magnetic structure disappears above 20T [39, 82]. This allows one to study in some detail the magnetoelectric coupling.

Because $BiFeO_3$ is essentially an antiferromagnet, the pure compound shows a rather uneventful low field magnetization where magnetization is proportional to the external field with a low susceptibility. This behavior is observed for all temperatures below 300K. For higher fields however, the Zeeman energy can dominate and the cycloid gets unstable around 19T above which it is replaced by a global canting [39, 82]. The linear high field magnetization extrapolates to a value of 0.25emu/g which can be attributed to the canting of magnetoelectric origin. The destruction of the cycloidal structure was also shown to produce a linear magnetoelectric effect as well as the appearance of a toroidal moment evidenced by the asymmetry of the off diagonal components of the linear magnetoelectric effect tensor [83]. A detailed experimental and theoretical

magnetic field evolution of the cycloid and its disappearance was reported in 2006 [39, 82]. However, many things are not yet clear and in particular no specific study as a function of the direction of a high magnetic field relative to the crystal axes has been performed. Our high quality single ferroelectric domain crystals allow us such a study which reveals some very interesting magnetoelectric properties of the cycloidal arrangement.

4.1 Samples and techniques

The samples used for this high field study are again the single crystals in the form of millimeter sized platelets with the [001] pseudocubic axis along the short dimension. The cycloidal arrangements have been previously studied in our crystals and it was concluded that at zero magnetic field, the cycloids are harmonic and often dominated by a single entity along one of the three symmetry allowed axes [8]. Polarization switching was also shown to toggle the plane of rotation of the antiferromagnetic spins, in good agreement with the expected magnetoelectric coupling.

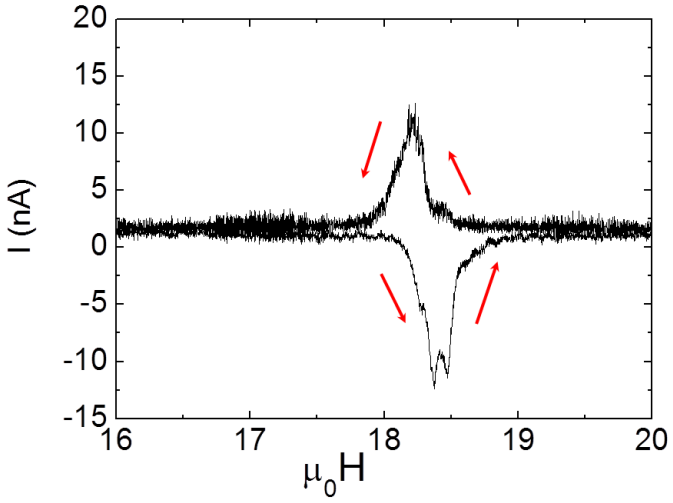

Figure 4.1: Pulsed magnetic field measurement of the current (black) near the field of disappearance of the cycloidal order. Integrating the current leads to a polarization change close to $10nC/cm^2$.

The High-field measurements were carried out at the 'Laboratoire National des Champs Magnétiques Intenses' in Toulouse (France) where pulsed fields of 50T are generated

with a 10 milisecond rise time and 300 milisecond fall time in a cryogenic environment. The field direction relative to the crystals can be varied within a set plane by rotating the samples mounted on a plate around a unique axis. The single crystals were glued with varnish and contacted in a capacitor fashion with silver wires linking the two top and bottom contacts perpendicular to the [001] direction.

A typical measurement of the current generated in the circuit during the field pulse is shown in figure 4.1. Near 20T, a negative current dip can be seen as the field increases followed by a positive peak as the field comes back down. Hence, a flow of charges in one direction as the cycloid disappears corresponds to the equivalent reverse flow when the cycloid reappears. Experimentally, P is measured indirectly by integrating the current generated in the circuit by the balancing of electric charges as P changes.

As a result, the current signal leads to a polarization of $10nC/cm^2$ and, thus $\Delta P/P = 10^{-4}$. This value is consistent with the polarization of improper ferroelectrics and it is therefore attributed to the cycloid. This polarization change as the cycloid disappears results from two magnetoelectric terms, linear and quadratic in magnetization : $P_i \propto \alpha_{ik} M_k + \beta_{ijk} M_j M_k$ with α and β the magnetoelectric tensors. Here, the ΔP value is attributed mainly to the polarization of magnetoelectric origin linked to the antiferromagnetic cycloidal structure.

In order to precisely measure the flop field, it is more convenient to measure the capacitance as it is difficult to precisely monitor a tiny current. ε can indeed be sensitively measured at high frequency (70kHz). The cycloid disappearance corresponds to a clear jump in capacitance directly related to the polarization. In fact, the electric field inside a parallel plate capacitor is given by :

$$E = \frac{D}{\varepsilon} \tag{4.1}$$

where D is the electric displacement and ε the dielectric function of the material. In our measurements, one can consider that $D \approx P_s$ the spontaneous polarization of $BiFeO_3$. This results in :

$$\frac{dE}{dP_s} = \frac{1}{\varepsilon} \tag{4.2}$$

Furthermore, considering the power expansion in polarization of the free energy as follows :

$$F = \frac{1}{2}aP^2 + \frac{1}{4}bP^4 + \ldots - EP \tag{4.3}$$

Minimizing the free energy with respect to P, leads to :

$$\frac{dF}{dP} = aP + bP^3 + \ldots - E = 0 \tag{4.4}$$

thus, $E = aP + bP^3$ and minimizing E with respect to P gives :

$$\frac{dE}{dP} = a + 3bP^2 = \frac{1}{\varepsilon} \tag{4.5}$$

with $P_s = P + \Delta P(H)$ the magnetoelectric part of the spontaneous polarization being small. Therefore, the jump in capacitance is proportional to that in P.

The response of the cycloidal state to a high applied magnetic field has been predicted to be anisotropic [39] and depend on the cosine of the two relevant angles :

- θ the angle within the cycloidal plane
- φ the equatorial angle in the plane perpendicular to P

It is therefore interesting to study the behavior of single crystals with a unique polarization state where large fields are applied along different directions.

4.2 Results and discussion

A typical set of data is presented in figure 4.2 where the capacitance (i.e. dielectric constant), measured along [001] is seen to jump at different magnetic fields depending on the field direction. Moreover, the jump itself has different amplitudes.

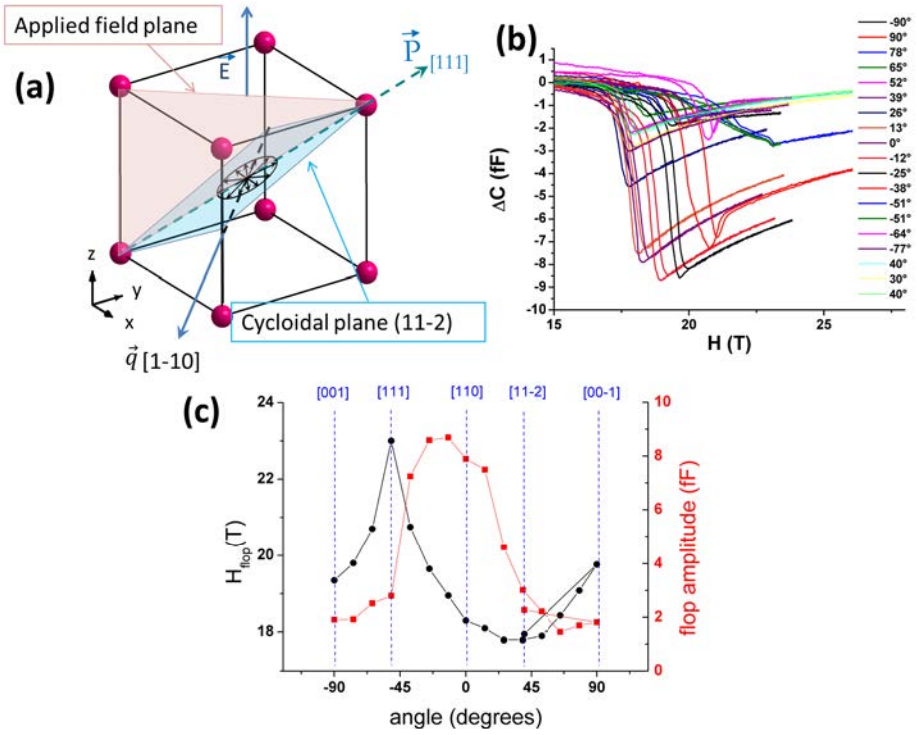

Figure 4.2: a) Geometry of the measurement where the field was rotated in the plane containing P[111] and the [001] direction (=90°) along which the capacitance is measured. b) High field measurements of the capacitance (along [001]) of a single polarization domain crystal as a function of the field direction. c) Summary of the flop fields and the amplitude of the capacitance jump amplitude as a function of angle in the measuring plane.

The field was set to be in the plane defined by the polarization direction [111] and the [001] axis across which the capacitance is measured. The flop fields range from 17.8 to 23T and are found maximum parallel to P and minimum along $[11\bar{2}]$, the direction perpendicular to one cycloidal plane. We note that the corresponding H_{flop} versus angle curve of figure 4.2 is globally close to the prediction of Fishman [84] (figure 4.3). However it is interesting to note that the measured behavior is associated to cycloids supposed not to be the most stable.

Figure 4.3: The critical field for longitude connecting z = (0,0,1) with (0,0,−1) through (1,1,0) with $\theta = cos^{-1}(\mathbf{m} \cdot \mathbf{z})$. The insets show the trajectory for the pseudocubic unit cell. Reproduced from ref [84]

In order to understand the magnetic dependence of the cycloid flop, a micromagnetic

simulation code has been adapted to the $BiFeO_3$ problem with the help of a team in CEA Le Ripault. The code is based on magnetic molecular dynamics which solves the Landau-Lifshitz-Gilbert equation for each atomic position.

For a given applied magnetic field, the magnetic state is given by the minimization of the following Hamiltonian :

$$H = H_{exch} + H_{anis} + H_{Ze} + H_{IME} + H_{DMI} \tag{4.6}$$

where the four terms are respectively the exchange, the anisotropy, the Zeeman, the inhomogeneous magnetoelectric and Dzyaloshinskii-Moryia energies.

These can be individually expressed as (S_i and S_j being neighboring spins on the chain) :

- $H_{exch} = J \sum \mathbf{S_i} \cdot \mathbf{S_j}$ with J the exchange integral. This term promotes antiparallel alignment of spins as $J < 0$.
- $H_{anis} = K \sum (\mathbf{P} \cdot \mathbf{S_i})^2$ with K the anisotropy constant along the polarization vector P. This term tends to align spins with the direction of the polarization.
- $H_{Ze} = \sum \mu_B \mathbf{S_i} \cdot \mathbf{B}$ with B the applied magnetic field. This term promotes parallel alignment of spins along B.
- $H_{IME} = G \sum \mathbf{P} \cdot \mathbf{R_{ij}} \times (\mathbf{S_i} \times \mathbf{S_j})$ with G the inhomogeneous ME constant. This term tends to impose a fixed angle between adjacent spins within a plane containing P.
- $H_{DMI} = \sum D_{ij} \cdot (\mathbf{S_i} \times \mathbf{S_j})$ with D_{ij} the Dzyaloshinskii-Moryia constant. This term gives a small canting to two neighboring spins in the plane perpendicular to D.

First we set up a model consisting of a one-dimensional chain of antiferromagnetic spins under an applied magnetic field parallel to P where the flop field is found to be maximal, around 23T.

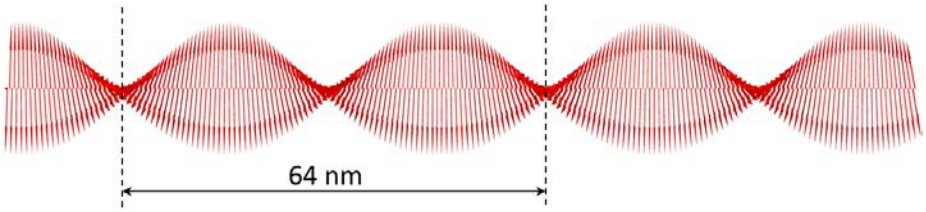

Figure 4.4: One-dimensional chain of antiferromagnetic spins which show a cycloidal ordering.

At low field, the magnetoelectric effect dominates and the equilibrium state is a cycloidal ordering of the spins as shown on figure 4.4. At 15T, the cycloidal ordering is destabilized in the direction of the applied magnetic field B. This results in an anharmonicity of the cycloidal ordering as can be seen on the top view of figure 4.5.

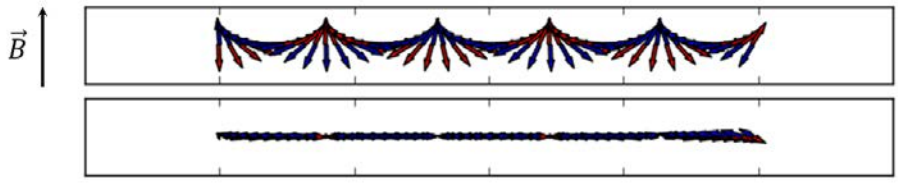

Figure 4.5: Side view (up) and top view (down) of the cycloidal ordering at 15T.

Finally, at 18T, the cycloid flops and rotates in a plane perpendicular to the applied electric field in order to align the weak ferromagnetic moment induced by the spin canting parallel to the applied magnetic field. The resulting magnetic structure is shown on figure 4.6.

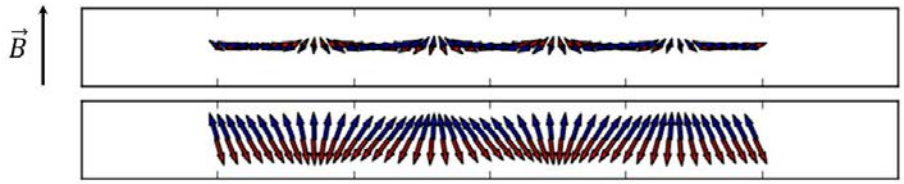

Figure 4.6: Side view (up) and top view (down) of the cycloidal ordering at 18T. The cycloidal order is lost and the spins have flopped.

The flop field is found lower than that measured in our crystals, indicating that the magnetoelectric coupling is a little greater than the presently accepted one. Interestingly, the measurements show a strong irreversibility as can be seen on figure4.7.

For the same crystal it can be seen that below 6T, the capacitance increases with field and comes back reversibly. However,when the maximum pulsed field is increased to 22.5T, the capacitance first increases but then decreases above 7T and shows a marked dip at 18T indicating the cycloid disappearance. It comes back from the maximum 22.5T irreversibly (black curve) and the zero field level is decreased by about 1fF. Subsequent 6T and 25T pulses, both positive and negative show a reversible and reproducible behavior.

When pulsing with a higher field of 50T, the capacitance starts by following the previous curve (it lags slightly behind on the graph but this is an experimental problem due to

the dynamical effect of the fast pulse rise), but coming back from the maximum field the cycloid reappears at a slightly higher field (19.5T) and the zero field capacitance is slightly decreased. Subsequent field pulses reproducibly follow the 50T curve.

As the macroscopic ferroelectric monodomain was subsequently checked to survive the entire field sequence, the changes must originate from the polarization induced by the cycloids. This is surprising as, by construction, the three allowed cycloids should produce a polarization parallel to the global macroscopic one. Indeed, at zero field, the free energy is minimized by the cycloids' geometry where the propagation vector (q) is perpendicular to the polarization and the antiferromagnetic spins rotate in a plane containing P and q [85]. This was corroborated by our previous neutron measurements. Hence, the cycloids are most likely to lie along the three 'allowed' symmetry directions. Two things can therefore change during the experiment: the population of q along these three directions and the cycloidal domain size.

Although it is hard to assess the latter, one can try to understand how the field can influence the domains populations. If at zero field, the free energy is equally minimized by the q vectors along $[1\bar{1}0]$, $[10\bar{1}]$ and $[01\bar{1}]$, the stability of these differs as a field is applied at a given angle. Indeed, the magnetic evolution is rather different when the magnetic field is applied perpendicular to the plane of rotation or in this plane. In the former case, the antiferromagnetic vectors gradually cant towards the field, thus minimizing the Zeeman energy. In the latter, the cycloid distorts and this costs more energy.

Thus, as already found by Fishman [84], the cycloid lying in the plane most perpendicular to H should be the most stable. This is however not consistent with our angular variation of flop fields. Beside this enigma, one can notice that in our geometry, the two other cycloids are degenerate in energy. Hence, it is very likely that after the flop, a cycloidal multidomain is obtained. In that case, a high density of uncompensated domain walls could contribute with a significant amount of linear magnetoelectric polarization.

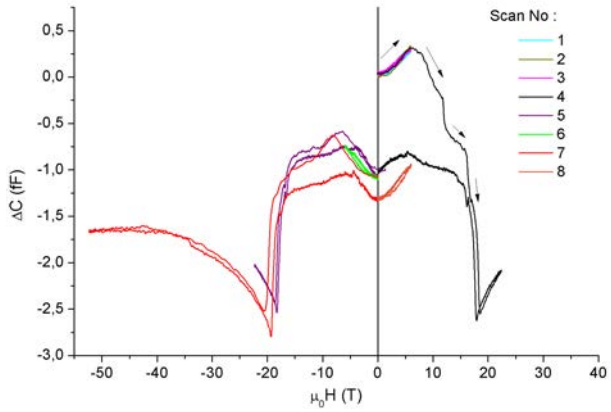

Figure 4.7: Evolution of the capacitance of a single polarization domain during consecutive magnetic field pulses along the [001] direction. The first curve was measured in the virgin state and as soon as the field exceeds about 7T, irreversible changes appear both in the field at which the cycloids appear/disappear and in the zero field capacitance.

Unfortunately, it is very hard to image those domains and only synchrotron PEEM [86] or SHG [87] could achieve such a measurement. On the simulation front, we have started to perform two-dimensional calculations which are still ongoing. Preliminary calculations show that indeed cycloidal domain walls are extremely perturbed regions (figure 4.8).

4.3 Conclusions and outlook

We have shown that we can measure the small polarization associated to the cycloid ordering through the capacitance and thus ε. This quantity allows to precisely measure the magnetic field induced disappearance of the cycloidal ordering. The study of the irreversibility of the capacitance shows that the as-grown 'mono' cycloidal state quickly disappears after the first field sequence, resulting in a multidomain cycloidal state.

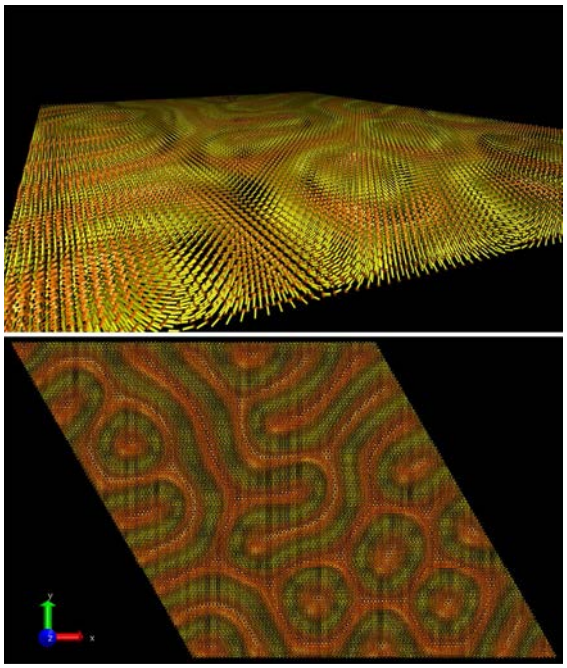

Figure 4.8: Two dimensional simulations of the cycloidal domains.

We believe that the extra polarization is coming from a high density of domain walls. Work is still in progress but two dimensional simulations are interesting as they give indications that close to domain walls, bubles could be generated. Thus it is perhaps also consistent with the surface diffraction results previously discussed.

Conclusion

In the present thesis, photoelectric and magnetic properties of both domains and domain walls in $BiFeO_3$ have been investigated, using original techniques of characterization.

First, a Scanning Photocurrent Microscope (SPCM) was used to study the bulk photovoltaic (BPV) effect in $BiFeO_3$ monodomain ferroelectric samples. By using circular shaped electrodes, we managed to spatially map the BPV current and have shown that it modulates in magnitude but also in direction with respect to the incident light polarization. Our measurements are consistent with prediction of the shift current theory, for which we provided a direct observation, and observed anisotropic current flows in different directions than that of the ferroelectric polarization i.e. the internal electric field. Our attempt to tailor the internal field leads us to demonstrate that a 180° domain wall can be positioned between two electrodes and reversibly distorted by an electric field. This distortion leads to the appearance of charges which in turn influence the local internal electric field in its vicinity. SPCM mapping of this system reveals that depolarizing fields can significantly improve the photovoltaic efficiency. Thus domain walls can be generated and precisely positioned in order to tailor the local photovoltaic efficiency. This opportunity broadens the applicative potential of ferroelectrics for photovoltaics but also for using domain walls as electronically active entities. Our measurements also emphasize the influence of the depolarizing field on the ferroelectric photovoltaics and the necessity to take it into account in first principle calculations.

Secondly, the magnetic properties of $BiFeO_3$ were studied on single crystals by synchrotron radiation and provide direct experimental evidence that long-range antiferromagnetic structures can be imprinted on soft ferromagnets through interface magnetic exchange. This results in a magnetic modulation of a cobalt layer deposited on multiferroic $BiFeO_3$ crystals containing antiferromagnetic cycloids. The magnetic layer could thus also be used to reveal antiferromagnetic long-range structures providing that the ferromagnet can be imaged or probed, which is usually easier than magnetic imaging in antiferromagnets. The imprint surface states were also imaged in thin films by surface diffraction on a pattern of a cycloidal order modulated by stripe domains with alternate in plane ferroelectric polarization. The alternating ferroelectric polarization in each domain leads to a toggling of the cycloidal plane between two variants, which

also gives rise to diffraction peaks. Moreover, the diffraction pattern also indicates that there may be a periodic structure in the direction parallel to the stripes. This could be consistent with the establishment of another superimposed modulation running parallel to the stripes which could result in a chessboard pattern. This preliminary work is promising as it indicates that domain walls generate specific structures with possible uncompensated magnetization. In addition, the chessboard of cycloidal ordering has to be further investigated, and especially imaged as it could originate from the chiral character of the cycloids.

Finally the cycloidal ordering was also characterized through measurements of dielectric susceptibility under high applied magnetic fields. The as-grown 'mono' cycloidal state quickly disappears after the first field sequence, resulting in a multidomain cycloidal state which could lead to an extra polarization, coming from a high density of domain walls. Most of this work is still in progress but two dimensional simulations are interesting as they give indications that close to domain walls, bubles could be generated in agreement with the measured surface diffraction patterns.

Bibliography

[1] H. Schmid, "Multi-ferroic magnetoelectrics," Ferroelectrics **162**, 317–338 (1994).

[2] W. Eerenstein, N. D. Mathur, and J. F. Scott, "Multiferroic and magnetoelectric materials," Nature **442**, 759–765 (2006).

[3] N. A. Hill, "Why are there so few magnetic ferroelectrics?" J. Phys. Chem. B **104**, 6694–6709 (2000).

[4] J. Privratska¡ and V. Janovec, "Pyromagnetic domain walls connecting antiferromagnetic non-ferroelastic magnetoelectric domains," Ferroelectrics **204**, 321–331 (1997).

[5] J. Seidel, L. W. Martin, Q. He, Q. Zhan, Y.-H. Chu, A. Rother, M. E. Hawkridge, P. Maksymovych, P. Yu, M. Gajek, N. Balke, S. V. Kalinin, S. Gemming, F. Wang, G. Catalan, J. F. Scott, N. A. Spaldin, J. Orenstein, and R. Ramesh, "Conduction at domain walls in oxide multiferroics," Nat Mater **8**, 229–234 (2009).

[6] J. Seidel, D. Fu, S.-Y. Yang, E. Alarcón-Lladó, J. Wu, R. Ramesh, and J. W. Ager, "Efficient photovoltaic current generation at ferroelectric domain walls," Phys. Rev. Lett. **107**, 126805 (2011).

[7] J. Wang, J. B. Neaton, H. Zheng, V. Nagarajan, S. B. Ogale, B. Liu, D. Viehland, V. Vaithyanathan, D. G. Schlom, U. V. Waghmare, and others, "Epitaxial BiFeO3 multiferroic thin film heterostructures," Science **299**, 1719–1722 (2003).

[8] D. Lebeugle, D. Colson, A. Forget, M. Viret, A. M. Bataille, and A. Gukasov, "Electric-field-induced spin flop in BiFeO3 single crystals at room temperature," Phys. Rev. Lett. **100**, 227602 (2008).

[9] T. Zhao, A. Scholl, F. Zavaliche, K. Lee, M. Barry, A. Doran, M. P. Cruz, Y. H. Chu, C. Ederer, N. A. Spaldin, R. R. Das, D. M. Kim, S. H. Baek, C. B. Eom, and R. Ramesh, "Electrical control of antiferromagnetic domains in multiferroic BiFeO3 films at room temperature," Nat Mater **5**, 823–829 (2006).

[10] D. Lebeugle, D. Colson, A. Forget, and M. Viret, "Very large spontaneous electric polarization in BiFeO3 single crystals at room temperature and its evolution under cycling fields," Applied Physics Letters **91**, 022907 (2007).

[11] D. Lebeugle, D. Colson, A. Forget, M. Viret, P. Bonville, J. F. Marucco, and S. Fusil, "Room-temperature coexistence of large electric polarization and magnetic order in BiFeO3 single crystals," Phys. Rev. B **76**, 024116 (2007).

[12] J. E. Giencke, C. M. Folkman, S.-H. Baek, and C.-B. Eom, "Tailoring the domain structure of epitaxial BiFeO3 thin films," Current Opinion in Solid State and Materials Science **18**, 39–45 (2014).

[13] D. B. Strasfeld, A. Dorn, D. D. Wanger, and M. G. Bawendi, "Imaging schottky barriers and ohmic contacts in PbS quantum dot devices," Nano Letters **12**, 569–575 (2012).

[14] J. Kreisel, M. Alexe, and P. A. Thomas, "A photoferroelectric material is more than the sum of its parts," Nat Mater **11**, 260–260 (2012).

[15] T. Choi, S. Lee, Y. J. Choi, V. Kiryukhin, and S.-W. Cheong, "Switchable ferroelectric diode and photovoltaic effect in BiFeO3," Science **324**, 63–66 (2009).

[16] S. Y. Yang, J. Seidel, S. J. Byrnes, P. Shafer, C.-H. Yang, M. D. Rossell, P. Yu, Y.-H. Chu, J. F. Scott, J. W. Ager, L. W. Martin, and R. Ramesh, "Above-bandgap voltages from ferroelectric photovoltaic devices," Nature Nanotechnology **5**, 143–147 (2010).

[17] H. Béa, M. Gajek, M. Bibes, and A. Barthélémy, "Spintronics with multiferroics," J. Phys.: Condens. Matter **20**, 434221 (2008).

[18] N. A. Spaldin and M. Fiebig, "The renaissance of magnetoelectric multiferroics," Science **309**, 391–392 (2005).

[19] D. Khomskii, "Classifying multiferroics: Mechanisms and effects," Physics **2** (2009).

[20] J. Valasek, "Piezo-electric and allied phenomena in rochelle salt," Phys. Rev. **17**, 475–481 (1921).

[21] L. Landau, "The theory of phase transitions," Nature **138**, 840–841 (1936).

[22] M. Stengel and N. A. Spaldin, "Origin of the dielectric dead layer in nanoscale capacitors," Nature **443**, 679–682 (2006).

[23] I. Dzyaloshinsky, "A thermodynamic theory of "weak" ferromagnetism of antiferromagnetics," Journal of Physics and Chemistry of Solids **4**, 241–255 (1958).

[24] T. Moriya, "Anisotropic superexchange interaction and weak ferromagnetism," Phys. Rev. **120**, 91–98 (1960).

[25] P. Curie, "Sur la symétrie dans les phénomènes physiques, symétrie d'un champ électrique et d'un champ magnétique," Journal de Physique Théorique et Appliquée **3**, 393–415 (1894).

[26] Y. Tokura, S. Seki, and N. Nagaosa, "Multiferroics of spin origin," Rep. Prog. Phys. **77**, 076501 (2014).

[27] S. Ishiwata, Y. Kaneko, Y. Tokunaga, Y. Taguchi, T.-h. Arima, and Y. Tokura, "Perovskite manganites hosting versatile multiferroic phases with symmetric and antisymmetric exchange strictions," Phys. Rev. B **81**, 100411 (2010).

[28] T. Kimura, T. Goto, H. Shintani, K. Ishizaka, T. Arima, and Y. Tokura, "Magnetic control of ferroelectric polarization," Nature **426**, 55–58 (2003).

[29] D. C. Arnold, K. S. Knight, F. D. Morrison, and P. Lightfoot, "Ferroelectric-paraelectric transition in BiFeO3 : Crystal structure of the orthorhombic β phase," Phys. Rev. Lett. **102**, 027602 (2009).

[30] D. C. Arnold, K. S. Knight, G. Catalan, S. A. T. Redfern, J. F. Scott, P. Lightfoot, and F. D. Morrison, "The β-to-γ transition in BiFeO3: A powder neutron diffraction study," Adv. Funct. Mater. **20**, 2116–2123 (2010).

[31] J. M. Moreau, C. Michel, R. Gerson, and W. J. James, "Ferroelectric BiFeO3 x-ray and neutron diffraction study," Journal of Physics and Chemistry of Solids **32**, 1315–1320 (1971).

[32] F. Kubel and H. Schmid, "Structure of a ferroelectric and ferroelastic monodomain crystal of the perovskite BiFeO3," Acta Crystallographica Section B Structural Science **46**, 698–702 (1990).

[33] L. D. Landau and E. Lifshitz, "On the theory of the dispersion of magnetic permeability in ferromagnetic bodies," Phys. Z. Sowjetunion **8**, 101–114 (1935).

[34] C. Kittel, "Theory of the structure of ferromagnetic domains in films and small particles," Phys. Rev. **70**, 965–971 (1946).

[35] T. Mitsui and J. Furuichi, "Domain structure of rochelle salt and KH2po4," Phys. Rev. **90**, 193–202 (1953).

[36] M. Daraktchiev, G. Catalan, and J. F. Scott, "Landau theory of ferroelectric domain walls in magnetoelectrics," Ferroelectrics **375**, 122–131 (2008).

[37] C. Lichtensteiger, P. Zubko, M. Stengel, P. Aguado-Puente, J.-M. Triscone, P. Ghosez, and J. Junquera, "Ferroelectricity in ultrathin-film capacitors," (Wiley-VCH Verlag GmbH & Co. KGaA, 2011), pp. 265–230.

[38] I. Sosnowska, T. P. Neumaier, and E. Steichele, "Spiral magnetic ordering in bismuth ferrite," Journal of Physics C: Solid State Physics **15**, 4835–4846 (1982).

[39] A. K. Zvezdin, A. M. Kadomtseva, S. S. Krotov, A. P. Pyatakov, Y. F. Popov, and G. P. Vorob'ev, "Magnetoelectric interaction and magnetic field control of electric polarization in multiferroics," Journal of Magnetism and Magnetic Materials **300**, 224–228 (2006).

[40] M. Mostovoy, "Ferroelectricity in spiral magnets," **96**, 067601 (2006).

[41] S. G. Choi, H. T. Yi, S.-W. Cheong, J. N. Hilfiker, R. France, and A. G. Norman, "Optical anisotropy and charge-transfer transition energies in BiFeO3 from 1.0 to 5.5 eV," Phys. Rev. B **83**, 100101 (2011).

[42] A. G. Chynoweth, "Surface space-charge layers in barium titanate," **102**, 705–714 (1956).

[43] A. M. Glass, "High-voltage bulk photovoltaic effect and the photorefractive process in LiNbO3," Appl. Phys. Lett. **25**, 233 (1974).

[44] V. M. Fridkin, "Bulk photovoltaic effect in noncentrosymmetric crystals," Crystallography Reports **46**, 654–658 (2001).

[45] W. Kraut and R. von Baltz, "Anomalous bulk photovoltaic effect in ferroelectrics: A quadratic response theory," Phys. Rev. B **19**, 1548–1554 (1979).

[46] V. M. Fridkin, E. P. Efremova, B. H. Karimov, V. A. Kuznezov, I. P. Kuzmina, A. N. Lobachev, V. G. Lazarev, and A. J. Rodin, "The experimental investigation of the photovoltaic effect in some crystals without a center of symmetry," Appl. Phys. **25**, 77–80 (1981).

[47] R. von Baltz and W. Kraut, "Theory of the bulk photovoltaic effect in pure crystals," Phys. Rev. B **23**, 5590 (1981).

[48] J. E. Sipe and A. I. Shkrebtii, "Second-order optical response in semiconductors," Phys. Rev. B **61**, 5337–5352 (2000).

[49] S. M. Young and A. M. Rappe, "First principles calculation of the shift current photovoltaic effect in ferroelectrics," Phys. Rev. Lett. **109** (2012).

[50] H. T. Yi, T. Choi, S. G. Choi, Y. S. Oh, and S.-W. Cheong, "Mechanism of the switchable photovoltaic effect in ferroelectric BiFeO3," Adv. Mater. **23**, 3403–3407 (2011).

[51] L. Pintilie and M. Alexe, "Metal-ferroelectric-metal heterostructures with schottky contacts. i. influence of the ferroelectric properties," J. Appl. Phys. **98**, 124103 (2005).

[52] M. Stengel, P. Aguado-Puente, N. A. Spaldin, and J. Junquera, "Band alignment at metal/ferroelectric interfaces: Insights and artifacts from first principles," Phys. Rev. B **83** (2011).

[53] R. Moubah, O. Rousseau, D. Colson, A. Artemenko, M. Maglione, and M. Viret, "Photoelectric effects in single domain BiFeO3 crystals," Adv. Funct. Mater. **22**, 4814–4818 (2012).

[54] M. Alexe and D. Hesse, "Tip-enhanced photovoltaic effects in bismuth ferrite," Nat. Comm. **2**, 256 (2011).

[55] W. Ji, K. Yao, and Y. C. Liang, "Evidence of bulk photovoltaic effect and large tensor coefficient in ferroelectric BiFeO 3 thin films," Phys. Rev. B **84** (2011).

[56] S. M. Young, F. Zheng, and A. M. Rappe, "First-principles calculation of the bulk photovoltaic effect in bismuth ferrite," Phys. Rev. Lett. **109** (2012).

[57] A. Bhatnagar, A. Roy Chaudhuri, Y. Heon Kim, D. Hesse, and M. Alexe, "Role of domain walls in the abnormal photovoltaic effect in BiFeO3," Nat. Comm. **4** (2013).

[58] S. J. Clark and J. Robertson, "Band gap and schottky barrier heights of multiferroic BiFeO3," App. Phys. Lett. **90**, 132903 (2007).

[59] R. Guo, L. You, Y. Zhou, Z. Shiuh Lim, X. Zou, L. Chen, R. Ramesh, and J. Wang, "Non-volatile memory based on the ferroelectric photovoltaic effect," Nat. Comm. **4** (2013).

[60] M. Cormier, J. Ferré, A. Mougin, J.-P. Cromières, and V. Klein, "High resolution polar kerr magnetometer for nanomagnetism and nanospintronics," Review of Scientific Instruments **79**, 033706 (2008).

[61] W. Wu, J. R. Guest, Y. Horibe, S. Park, T. Choi, S.-W. Cheong, and M. Bode, "Polarization-modulated rectification at ferroelectric surfaces," Phys. Rev. Lett. **104** (2010).

[62] G.-L. Yuan and J. Wang, "Evidences for the depletion region induced by the polarization of ferroelectric semiconductors," Appl. Phys. Lett. **95**, 252904 (2009).

[63] M. Alexe, "Local mapping of generation and recombination lifetime in bifeo3 single crystals by scanning probe photoinduced transient spectroscopy," Nano Lett. **12**, 2193–2198 (2012).

[64] C. Himcinschi, I. Vrejoiu, M. Friedrich, L. Ding, C. Cobet, N. Esser, M. Alexe, and D. R. T. Zahn, "Optical characterisation of bifeo3 epitaxial thin films grown by pulsed-laser deposition," physica status solidi (c) **7**, 296–299 (2010).

[65] H. Huang, "Solar energy: Ferroelectric photovoltaics," Nat Photon **4**, 134–135 (2010).

[66] A. Zenkevich, Y. Matveyev, K. Maksimova, R. Gaynutdinov, A. Tolstikhina, and V. Fridkin, "Giant bulk photovoltaic effect in thin ferroelectric batio3 films," Phys. Rev. B **90**, 161409 (2014).

[67] S. Hong, T. Choi, J. H. Jeon, Y. Kim, H. Lee, H.-Y. Joo, I. Hwang, J.-S. Kim, S.-O. Kang, S. V. Kalinin, and B. H. Park, "Large resistive switching in ferroelectric bifeo3 nano-island based switchable diodes," Adv. Mater. **25**, 2339–2343 (2013).

[68] V. Gopalan, V. Dierolf, and D. A. Scrymgeour, "Defect-domain wall interactions in trigonal ferroelectrics," Annual Review of Materials Research **37**, 449–489 (2007).

[69] T. J. Yang, V. Gopalan, P. J. Swart, and U. Mohideen, "Direct observation of pinning and bowing of a single ferroelectric domain wall," Phys. rev. lett. **82**, 4106 (1999).

[70] R. K. Vasudevan, A. N. Morozovska, E. A. Eliseev, J. Britson, J.-C. Yang, Y.-H. Chu, P. Maksymovych, L. Q. Chen, V. Nagarajan, and S. V. Kalinin, "Domain wall geometry controls conduction in ferroelectrics," Nano Letters **12**, 5524–5531 (2012).

[71] M. Sacchi, N. Jaouen, H. Popescu, R. Gaudemer, J. M. Tonnerre, S. G. Chiuzbaian, C. F. Hague, A. Delmotte, J. M. Dubuisson, G. Cauchon, B. Lagarde, and F. Polack, "The SEXTANTS beamline at SOLEIL: a new facility for elastic, inelastic and coherent scattering of soft x-rays," J. Phys.: Conf. Ser. **425**, 072018 (2013).

[72] N. Jaouen, J.-M. Tonnerre, G. Kapoujian, P. Taunier, J.-P. Roux, D. Raoux, and F. Sirotti, "An apparatus for temperature-dependent soft x-ray resonant magnetic scattering," Journal of Synchrotron Radiation **11**, 353–357 (2004).

[73] D. Lebeugle, A. Mougin, M. Viret, D. Colson, and L. Ranno, "Electric field switching of the magnetic anisotropy of a ferromagnetic layer exchange coupled to the multiferroic compound bifeo3," Phys. Rev. Lett. **103**, 257601 (2009).

[74] S. S. Dhesi, S. A. Cavill, A. Potenza, H. Marchetto, R. A. Mott, P. Steadman, A. Peach, E. L. Shepherd, X. Ren, U. H. Wagner, and R. Reininger, "The nanoscience beamline (i06) at diamond light source," in "AIP Conference Proceedings," , vol. 1234 (AIP Publishing, 2010), vol. 1234, pp. 311–314.

[75] T. a. W. Beale, T. P. A. Hase, T. Iida, K. Endo, P. Steadman, A. R. Marshall, S. S. Dhesi, G. v. d. Laan, and P. D. Hatton, "RASOR: An advanced instrument for soft x-ray reflectivity and diffraction," Rev. of Sci. Instrum. **81**, 073904 (2010).

[76] H. A. Durr, E. Dudzik, S. S. Dhesi, J. B. Goedkoop, G. v. d. Laan, M. Belakhovsky, C. Mocuta, A. Marty, and Y. Samson, "Chiral magnetic domain structures in ultrathin FePd films," **284**, 2166–2168 (1999).

[77] J. P. Hannon, G. T. Trammell, M. Blume, and D. Gibbs, "X-ray resonance exchange scattering," Phys. Rev. Lett. **61**, 1245–1248 (1988).

[78] R. D. Johnson, P. Barone, A. Bombardi, R. J. Bean, S. Picozzi, P. G. Radaelli, Y. S. Oh, S.-W. Cheong, and L. C. Chapon, "X-ray imaging and multiferroic coupling of cycloidal magnetic domains in ferroelectric monodomain bifeo3," Phys. Rev. Lett. **110**, 217206 (2013).

[79] P. Fischer, M. Polomska, I. Sosnowska, and M. Szymanski, "Temperature dependence of the crystal and magnetic structures of BiFeO 3," J. Phys. C: Solid State Phys. **13**, 1931 (1980).

[80] M. Elzo, R. Moubah, C. Blouzon, M. Sacchi, S. Grenier, R. Belkhou, S. Dhesi, D. Colson, F. Torres, M. Kiwi, M. Viret, and N. Jaouen, "Coupling between an incommensurate antiferromagnetic structure and a soft ferromagnet in the archetype multiferroic bifeo3/cobalt system," Phys. Rev. B **91**, 014402 (2015).

[81] D. Sando, A. Agbelele, D. Rahmedov, J. Liu, P. Rovillain, C. Toulouse, I. C. Infante, A. P. Pyatakov, S. Fusil, E. Jacquet, C. Carrétéro, C. Deranlot, S. Lisenkov, D. Wang, J.-M. Le Breton, M. Cazayous, A. Sacuto, J. Juraszek, A. K. Zvezdin, L. Bellaiche, B. Dkhil, A. Barthélémy, and M. Bibes, "Crafting the magnonic and spintronic response of BiFeO3 films by epitaxial strain," Nat. Mater. **12**, 641–646 (2013).

[82] A. M. Kadomtseva, A. K. Zvezdin, Y. F. Popov, A. P. Pyatakov, and G. P. Vorob'ev, "Space-time parity violation and magnetoelectric interactions in antiferromagnets," Jetp Lett. **79**, 571–581 (2004).

[83] Y. F. Popov, A. M. Kadomtseva, S. S. Krotov, D. V. Belov, G. P. Vorob'ev, P. N. Makhov, and A. K. Zvezdin, "Features of the magnetoelectric properties of BiFeO3 in high magnetic fields," Low Temperature Physics **27**, 478–479 (2001).

[84] R. S. Fishman, "Orientation dependence of the critical magnetic field for multiferroic bifeo3," Phys. Rev. B **88** (2013).

[85] H. Katsura, N. Nagaosa, and A. V. Balatsky, "Spin current and magnetoelectric effect in noncollinear magnets," **95**, 057205 (2005).

[86] R. Moubah, M. Elzo, S. E. Moussaoui, D. Colson, N. Jaouen, R. Belkhou, and M. Viret, "Direct imaging of both ferroelectric and antiferromagnetic domains in multiferroic BiFeO3 single crystal using x-ray photoemission electron microscopy," Applied Physics Letters **100**, 042406 (2012).

[87] D. Meier, M. Maringer, T. Lottermoser, P. Becker, L. Bohaty, and M. Fiebig, "Observation and coupling of domains in a spin-spiral multiferroic," Phys. Rev. Lett. **102**, 107202 (2009).